

Remote arc generated plasma in diatomic gases

Citation for published version (APA):

Brussaard, G. J. H. (1999). *Remote arc generated plasma in diatomic gases*. [Phd Thesis 1 (Research TU/e / Graduation TU/e), Applied Physics and Science Education]. Technische Universiteit Eindhoven.
<https://doi.org/10.6100/IR520463>

DOI:

[10.6100/IR520463](https://doi.org/10.6100/IR520463)

Document status and date:

Published: 01/01/1999

Document Version:

Publisher's PDF, also known as Version of Record (includes final page, issue and volume numbers)

Please check the document version of this publication:

- A submitted manuscript is the version of the article upon submission and before peer-review. There can be important differences between the submitted version and the official published version of record. People interested in the research are advised to contact the author for the final version of the publication, or visit the DOI to the publisher's website.
- The final author version and the galley proof are versions of the publication after peer review.
- The final published version features the final layout of the paper including the volume, issue and page numbers.

[Link to publication](#)

General rights

Copyright and moral rights for the publications made accessible in the public portal are retained by the authors and/or other copyright owners and it is a condition of accessing publications that users recognise and abide by the legal requirements associated with these rights.

- Users may download and print one copy of any publication from the public portal for the purpose of private study or research.
- You may not further distribute the material or use it for any profit-making activity or commercial gain
- You may freely distribute the URL identifying the publication in the public portal.

If the publication is distributed under the terms of Article 25fa of the Dutch Copyright Act, indicated by the "Taverne" license above, please follow below link for the End User Agreement:

www.tue.nl/taverne

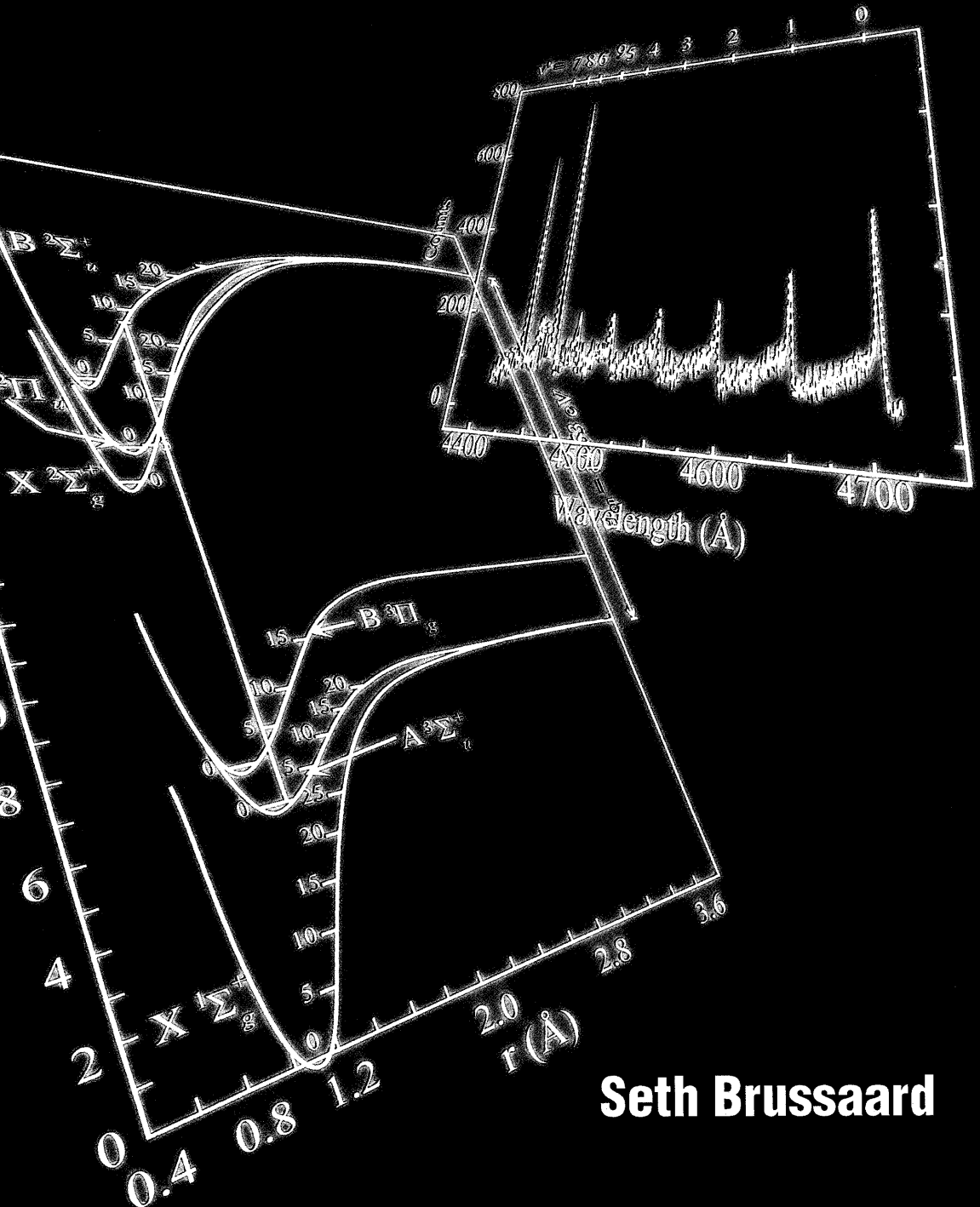
Take down policy

If you believe that this document breaches copyright please contact us at:

openaccess@tue.nl

providing details and we will investigate your claim.

Remote Arc Generated Plasma in Diatomic Gases



Seth Brussaard

Remote Arc Generated Plasma in Diatomic Gases

PROEFSCHRIFT

ter verkrijging van de graad van doctor
aan de Technische Universiteit Eindhoven,
op gezag van de Rector Magnificus, prof.dr. M. Rem,
voor een commissie aangewezen door het College
voor Promoties in het openbaar te verdedigen op
dinsdag 2 maart 1999 om 16.00 uur

door

Gerrit Jacobus Hendrik Brussaard

geboren te Leidschendam

Dit proefschrift is goedgekeurd door de promotoren:

prof.dr.ir. D.C. Schram

en

prof.dr. A.W. Kleyn

en de copromotor:

dr.ir. M.C.M. van de Sanden

The work described in this thesis was supported by the Netherlands Technology Foundation (STW) of the Netherlands Organization for Scientific Research (NWO) in the project titled *A High Intensity Particle Source for Plasma Surface Engineering and Chemical Kinetic Studies*, STW Project ETN33.3049

Drukwerk: Universiteitsdrukkerij Technische Universiteit Eindhoven

CIP-DATA LIBRARY TECHNISCHE UNIVERSITEIT EINDHOVEN

Brussaard, Gerrit Jacobus Hendrik

Remote Arc Generated Plasma in Diatomic Gases / by Gerrit Jacobus Hendrik Brussaard.-
Eindhoven: Eindhoven University of Technology, 1999.-

Thesis.-

With summary in Dutch.-

ISBN 90-386-0807-1

NUGI 812

Trefw.: plasma / plasma diagnostieken / proces plasma's

Subject headings: remote plasma / plasma diagnostics / plasma processing / non-equilibrium plasmas

Contents

1. General Introduction	1
2. Langmuir Probe Measurements in the Downstream Plasma	9
3. Determination of the Dissociation Degree in a Hydrogen Plasma by Electron Beam Induced Fluorescence	39
4. Drift Velocity and Diffusion in the downstream argon plasma	63
5. Ion Densities in a High Intensity, Low Flow Nitrogen-Argon Plasma	79
6. Evidence for charge exchange between N^+ and $N_2(A^3\Sigma_u^+)$ in a low temperature nitrogen plasma.	89
7. The Density of Ions and Metastable Molecules in the Nitrogen Plasma	99
8. Stripping of Photoresist Using a Remote Thermal Ar/O ₂ and Ar/N ₂ /O ₂ Plasma	117
9. General Conclusions	137
Summary	140
Samenvatting	142

1 General Introduction

1.1 Low-temperature plasmas

Low-temperature plasma processing finds many applications in modern manufacturing industry. Plasmas enable materials processing beyond the possibilities of purely chemical treatment. The idea behind plasma processing is to activate particles by an electrical discharge, thus avoiding the necessity of chemical activation or heating of the material. An important factor herein is the possibility of using relatively low substrate temperatures, which greatly widens the variety of materials that can be processed. Furthermore, in a controlled plasma process only those particles necessary for the desired process need to be present and the creation of toxic byproducts is minimized. New materials and manufacturing techniques have thus been developed with the increasing use of processing plasmas [1].

The semiconductor industry in particular has used plasmas to improve their products [2]. Plasma processing has enabled the fabrication of ever smaller and more complicated devices. With plasmas it has become possible to deposit thin layers with the desired composition and etch and deposit small structures. Presently features as small as $0.10\ \mu\text{m}$ with an aspect ratio of at least 3 have been produced on 300 mm wafers. The high demands on the quality of semiconductor devices require good control over the plasma species. The emphasis in these processes lies on reliability and homogeneity rather than on processing time. The resulting high equipment cost and long processing times are justified by the enormous revenue created.

On the other side of plasma processing industry came the further development of established plasma techniques. Plasma spraying and sputtering deposit relatively thick layers ($> 1\ \mu\text{m}$) with less stringent demands on quality. Such products include the nitriding of titanium to create wear-resistant layers on high-speed drills and the deposition of the aluminum layer found in compact discs. The greatest advantages of plasmas in these applications are the speed of the production and the possibility to deposit layers on a wide variety of materials. Even larger and more robust plasmas are used for the disposal of toxic and hazardous wastes [3].

The development of new plasma sources such as the one under investigation in this thesis, opens the possibility to apply plasma processing at high speeds, but still with sufficient control to manufacture rather complex materials. An example of this is the deposition of amorphous silicon layers for the manufacturing of thin-film solar cells [4]. The quality demands on the deposited layers are rather stringent in order to produce solar cells with the required efficiency. On the other hand, the cost of production must remain low to be able to compete with other sources of energy.

In conventional plasmas, the plasma is generated at the same position as where the material being processed is situated (so-called direct plasmas). This means that there is a tradeoff

between process rates and the quality of the product. Increasing the power input into a plasma leads to larger energy fluxes and higher bias potentials. As a result of the substrate bias, ions are accelerated causing bombardment and damage at the surface. Charging of the substrate due to higher electron densities induces electric fields and current through the underlying material, which can destroy previously manufactured structures. The trend in the development of new reactors is towards remotely generated plasmas. In these so-called "downstream" reactors the production region of the plasma is separate from the processing region and active particles are carried by gas flow. Most common of these configurations are remote plasma reactors such as the remote microwave (Distributed) Electron Cyclotron Resonance ((D)ECR) plasma [5], RF Inductively and Transformer Coupled Plasma (ICP and TCP) [6] and the Helicon plasma [7]. The advantages that led to the development of the remote microwave and RF reactors mentioned above have also led to the investigation of the use of the thermal DC arc source for downstream processing. The downstream plasma generated by the arc is the main topic of research of this thesis. In the high-density arc plasma, gases are efficiently dissociated and ionized, producing high fluxes of active particles [8]. The plasma is let to expand supersonically into a low pressure vessel. The supersonic expansion makes this plasma truly remote in the sense that there is no backflow of particles from the downstream region into the source. This allows a great variety of gases to be used downstream without fear of damaging the source. The expansion also lowers the electron temperature [9] and downstream addition of molecules leads to charge exchange and dissociative recombination, further improving the ratio of atoms to ions [10, 11].

In fundamental research of low temperature plasmas, nitrogen and oxygen have received a lot of attention because of the abundance of these gases in the Earth's atmosphere. Through the study of the aurora phenomenon, for example, Kaplan [12, 13] discovered a short-duration afterglow later called the "pink afterglow" [14]. In this afterglow of a nitrogen plasma, electrons and ions are created after the plasma has been switched off. The effect has been explained by reactions between electronically excited metastable molecules [15]. Since then, the increased use of computers has led to more complete modeling of nitrogen plasmas [16] and more detailed measurements have become available [17, 18], solving many of the existing questions. The investigation of processes taking place at the surface during plasma nitriding of materials has led to many new questions [19].

Fundamental research on nitrogen-oxygen plasmas is also of great interest in the investigation of the behavior of spacecraft during re-entry into the Earth's atmosphere [20]. During re-entry of the Apollo capsules and the Space Shuttle plasma chemistry in the bow-shock seriously altered the flight performance of these spacecraft [21]. Another challenge is posed by the

design of the ceramic heat shields. The effects of these surfaces on the plasma, v.v., during re-entry are still not well understood.

From both a fundamental point of view and for the applicability of plasmas, the challenge is the development of plasmas with a high degree of activation and a wide parameter space in the operation of the plasma. With this view a project was set up, funded by the Technology Foundation (STW) of the Netherlands Organization for Scientific Research (NWO), to investigate the remote thermal arc as a high-intensity particle source [22]. The high flux of energetic particles created by the arc source leads to high processing rates [23, 24]. Apart from the higher flux, the difference with other (semi) remote plasmas is the high degree of dissociation. In diatomic gases, the source creates mainly atoms and atomic ions. This difference in composition opens the possibility to investigate new kinetic interactions [25].

It has been the aim of the work presented in this thesis to investigate the behavior of particles in the downstream plasma in the presence of molecules, specifically nitrogen, hydrogen and oxygen. Several diagnostic techniques are investigated that are necessary to obtain useful and reliable information on particle densities, energy and velocity necessary to determine the composition and reactions taking place in these plasmas. From the measurements a global picture of these plasmas is extracted. In a more detailed study the reactions involving nitrogen ions are investigated. Photoresist etching is demonstrated as a promising application of the remote arc generated plasma as a processing tool.

1.2 Outline of the thesis

In the first part (Chapters 2 and 3) two diagnostic techniques are presented for the investigation of the downstream plasma. Langmuir probe theory is critically reviewed in Chapter 2. The appropriate theories for interpretation of Langmuir probe measurements in the downstream plasma are presented. In an extension of the applicability of the Langmuir probe the theory of probe measurements in the presence of a magnetic field is investigated. In Chapter 3 Electron Beam Induced Fluorescence is introduced as a new technique to determine the dissociation degree in a hydrogen plasma.

The second part of the thesis describes the investigation of the drift velocity, diffusion and recombination in the downstream plasma. Resonant Laser Induced Fluorescence (LIF) is used in Chapter 4 to determine the drift velocity and temperature of metastable argon atoms in a pure argon plasma. A theoretical diffusion model is compared to the spatial distribution of ions, measured by Langmuir probe. Nitrogen is introduced into an argon plasma in Chapter 5. The process of charge exchange and dissociative recombination is established.

In the third part the behavior of nitrogen ions is studied in more detail. Optical emission spectroscopy in combination with Langmuir probe measurements provides evidence for a charge exchange mechanism between atomic ions and metastable molecules. The evidence for these reactions is presented in Chapter 6. In Chapter 7, the investigation of nitrogen ions is extended to enable the determination of the densities of electrons, atomic ions, molecular ions and metastable molecules throughout the downstream plasma.

Finally, Chapter 8 shows the application of the remote arc generated plasma for the removal of photoresist from crystalline silicon. Argon-oxygen and argon-nitrogen-oxygen plasmas are used and the dependence of etch rate on various parameters is investigated. The importance of flow and diffusion of the particles as well as the kinetics of charge exchange and dissociative recombination leading to the measured etch rates is discussed.

1.3 Brief description of the experimental setup

1.3.1 The cascaded arc plasma source

The plasma source is a cascaded arc as shown in Fig. 1.1. A current is drawn from the three cathodes to the anode nozzle through a channel with a diameter of typically 4 mm and a length of approximately 5 cm. The total current can be varied between 35 and 75 A; for lower current settings the plasma may become unstable and the upper limit of 75 A is determined by the power supply. Pressure inside the arc source is determined by the gas flow, arc current, type of gas and is typically 0.1-1 bar (near atmospheric). The gas flow through the arc can be varied between 0.1 and 10 standard liters per minute (slm). For gas flow rates below 0.5 slm, the arc design has been adjusted slightly (see Chapter 5 of this thesis) to keep the upstream pressure near the cathodes sufficiently high.

The operation of this source has been studied quite extensively during the past decade. Kroesen [26] and Van de Sanden [27, 28] have presented results of the expanding argon plasma. In later studies, hydrogen has been added as a carrier gas. De Graaf [29] and Meulenbroeks [30] have investigated the influence of different mixtures of argon and hydrogen and finally have worked with pure hydrogen as a carrier gas. This work has been continued by Zhou Qing [31]. A theoretical investigation of the arc with hydrogen as a carrier gas was performed by Jansen [32]. During the period that extensive investigation into the hydrogen plasma was carried out, experiments were also started on the working of the arc source with nitrogen as a carrier gas [11]. It turned out that with some minor adjustments, the cascaded arc could be run on hydrogen and nitrogen without much difficulty. The results of these investigations show that at normal operating conditions the electron temperature is typically 1 eV. The ionization degree is around 10%; electron densities are of the order 10^{21} .

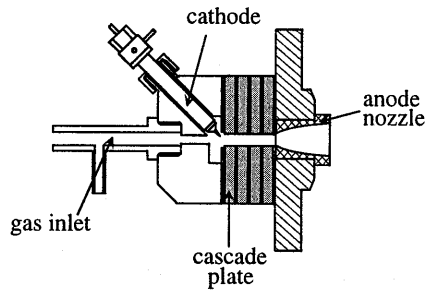


Figure 1.1: The cascaded arc source.

10^{22} m^{-3} . The arc produces electrons and atomic ions (Ar^+ , H^+ , N^+) since molecular ions have very short lifetimes at the aforementioned temperature and electron density. In case hydrogen or nitrogen is added, the dissociation degree in the arc is high, 50-100% [33, 34].

1.3.2 The supersonic expansion and shock

In the anode plate of the cascaded arc source, a nozzle is fitted through which the plasma is let to expand into the low pressure vessel (Fig. 1.2). The nozzle used in the present investigations is parabolically shaped, as proposed by De Graaf [35]. Due to the pressure difference between the arc source and the vessel, the plasma is accelerated and expands supersonically. Inside the vessel at a few centimeters from the nozzle, a stationary shock occurs after which the plasma moves at subsonic velocity. The expansion and barrel shock in the argon plasma have been investigated theoretically and experimentally by Van de Sanden [27]. In the expansion the temperature of the particles drops from 1 eV to 0.1 eV. In the shock region the temperature rises to approximately 0.3 eV and decreases slowly downstream. The electron density drops from 10^{21} m^{-3} to 10^{19} m^{-3} in the supersonic expansion; it increases by approximately a factor 4 in the shock. The exact densities and the position of the shock depend on arc operating conditions and vessel pressure. Experimental results of the supersonic expansion in argon-hydrogen mixtures have been presented by Meulenbroeks [30]. The results are similar to those in argon. Theoretical results on expansion and shock are not available (yet) for mixtures of argon with nitrogen or hydrogen, or for the pure hydrogen and nitrogen plasmas. Based on the investigations mentioned above, it is assumed that the particle composition (relative densities of electrons, ions, atoms and molecules) is preserved through the expansion and in the shock. The temperatures (electron, ion and neutral particle temperatures) are all assumed to be approximately 0.3 eV in and just after the shock.

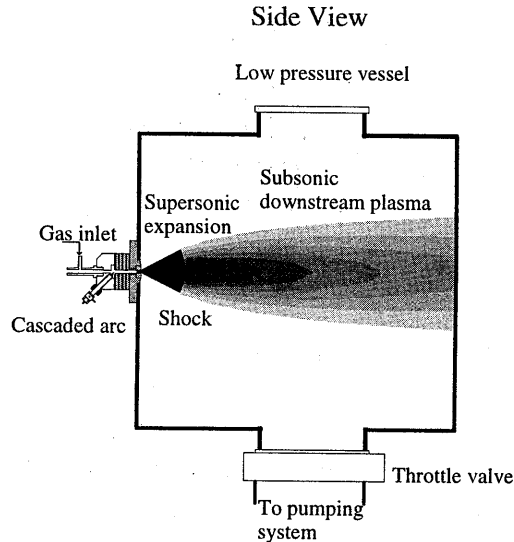


Figure 1.2: The remote thermal arc plasma setup

1.3.3 The downstream plasma

The main interest of the investigations in this thesis is the plasma in the low pressure vessel. The vessel is a stainless steel cylinder of 0.4 m length and 0.4 m diameter (50 liters) pumped by a system of roots blowers with a maximum capacity of 1000 m³/hour. The pressure inside the vessel can be varied by closing or opening the valve between the vessel and the pumping system. During normal operation the pressure is varied between 10 and 250 Pa.

After the supersonic expansion and shock, the plasma particles emanated from the arc flow into the downstream vessel at subsonic speed (< 1000 m/s). The plasma will diffuse towards the vessel walls, while moving further downstream. The particles will interact with each other and with the background gas present in the vessel. Since there is no power input into the plasma in this region, the plasma will be recombining. In a pure argon plasma the recombination is through three particle recombination (ion plus two electrons) [27]. This is a relatively slow process. The main loss mechanism in a pure argon plasma, therefore, is diffusion of electrons and ions to the vessel walls [27, 36]. In several earlier studies [11, 29, 30] it was found that recombination becomes fast when nitrogen is added, and even faster with the addition of hydrogen. The fast recombination is caused by charge exchange between atomic ions and molecules, followed by dissociative recombination of the molecular ion. This behavior is investigated in this thesis for argon-nitrogen mixtures. Charge exchange and dissociative recombination are studied in more detail for a pure nitrogen plasma. As discussed above, the downstream plasma produced by the cascaded arc source has many practical

applications. In the application of this plasma for the deposition of thin films promising results have already been achieved [24, 37, 38]. In this thesis the applicability of the remote thermal arc plasma is investigated for the removal of photoresist by an argon plasma containing oxygen and nitrogen-oxygen mixtures. In this application several advantages of the setup are combined. The high flow of radicals results in high removal rates. The relatively low ion density (due to the dissociative recombination) leads to a low current density through the substrate (preventing damage to underlying structures). Substrate bias is negligible, thus damage by ion impact is avoided.

References

- 1 M.A. Lieberman, and A.J. Lichtenberg, *Principles of Plasma Discharges and Materials Processing*, John Wiley & Sons, Inc., New York (1994).
- 2 P.F. Williams ed., *Plasma Processing of Semiconductors*, NATO ASI Series E: Applied Sciences **336** (1996).
- 3 W. Hoffelner, R. Burkhard, V. Haefeli, and H. Sun, Proc. 13th ISPC IV, Beijing China, 1915 (1997).
- 4 W. Luft, and Y.S. Tsuo, *Hydrogenated Amorphous Silicon Alloy Deposition Processes*, Marcel Dekker, New York (1993).
- 5 M. Moisan, C. Barbeau, R. Claude, C.M. Ferreira, J. Margot, J. Paraszczak, A.B. Sauve, and M.R. Wertheimer, *J. Vac. Sci. Technol. B* **9**, 8 (1991).
- 6 J. Hopwood, C.R. Guarnieri, S.J. Whitehair, and J.J. Cuomo, *J. Vac. Sci. Technol. A* **11**, 147 (1993).
- 7 A.J. Perry, D. Vender, and R.W. Boswell, *J. Vac. Sci. Technol. B* **9**, 310 (1991).
- 8 M.I. Boulos, P. Fauchais, and E. Pfender eds., *Thermal Plasmas - Fundamentals and Applications Volume 1*, Plenum Press, New York (1994).
- 9 M.C.M. van de Sanden, R. van den Bercken, and D.C. Schram, *Plasma Sources Sci. Technol.* **3**, 511 (1994).
- 10 R.F.G. Meulenbroeks, A.J. van Beek, A.J.G. van Helvoort, M.C.M. van de Sanden, and D.C. Schram, *Phys. Rev. E* **49**, 4397 (1994).
- 11 R.P. Dahiya, M.J. de Graaf, R.J. Severens, H. Swelsen, M.C.M. van de Sanden, and D.C. Schram, *Phys. Plasmas* **1** 2086 (1994).
- 12 J. Kaplan, *Phys. Rev.* **42**, 807 (1932).
- 13 J. Kaplan, *Phys. Rev.* **54**, 176 (1938).
- 14 G.E. Beale Jr., and H.P. Broida, *J. Chem. Phys.* **31**, 1030 (1959).
- 15 M.A. Biondi, *Phys. Rev.* **82**, 453 (1951).
- 16 J. Loureiro, C.M. Ferreira, M. Capitelli, C. Gorse, and M. Cacciatore, *J. Phys. D* **23**, 1371 (1990).
- 17 G. Cernogora, C.M. Ferreira, L. Hochard, M. Touzeau, and J. Loureiro, *J. Phys. B* **17**, 4429 (1984).
- 18 P. Supiot, O. Dessaux, and P. Goudmand, *J. Phys. D* **28**, 1826 (1995).
- 19 M. Capitelli, C. Gorse, and A. Ricard, *J. Physique Lett.* **44**, L-251 (1983).
- 20 M. Capitelli ed., *Molecular Physics and Hypersonic Flows*, NATO/ASI Series C: Mathematical and Physical Sciences **482** (1995).

- 21 J.R. Maus, *AIAA J. Spacecrafts and Rockets* **21**, 136 (1984).
- 22 *A High Intensity Particle Source for Plasma Surface Engineering and Chemical Kinetic Studies*, STW Project ETN33.3049
- 23 J.W.A.M. Gielen, M.C.M. van de Sanden, P.R.M. Kleuskens, and D.C. Schram, *Plasma Sources Sci. Technol.* **5**, 492 (1996).
- 24 J.J. Beulens, A.J.M. Buuron, M.J. de Graaf, G.J. Meeusen, M.C.M. van de Sanden, A.T.M. Wilbers, and D.C. Schram, *J. High Temp. Chem. Processes* **1**, 105 (1992).
- 25 G.J.H. Brussaard, E. Aldea, M.C.M. van de Sanden, G. Dinescu, and D.C. Schram, *Chem. Phys. Lett.* **290**, 379 (1998).
- 26 G.M.W. Kroesen, D.C. Schram, A.T.M. Wilbers, and G.J. Meeusen, *Contrib. Plasma Phys.* **31**, 27 (1991).
- 27 M.C.M. van de Sanden, J.M. de Regt, and D.C. Schram, *Phys. Rev. E* **47**, 2792 (1993).
- 28 M.C.M. van de Sanden, J.M. de Regt, and D.C. Schram, *Plasma Sources Sci. Technol.* **3**, 501 (1994).
- 29 M.J. de Graaf, R.J. Severens, R.P. Dahiya, M.C.M. van de Sanden, and D.C. Schram, *Phys. Rev. E* **48**, 2098 (1993)
- 30 R.F.G. Meulenbroeks, R.A.H. Engeln, M.N.A. Beurskens, R.M.J. Paffen, M.C.M. van de Sanden, J.A.M. van der Mullen, and D.C. Schram, *Plasma Sources Sci. Technol.* **4**, 74 (1995).
- 31 Z. Qing, D.K. Otorbaev, G.J.H. Brussaard, M.C.M. van de Sanden, and D.C. Schram, *J. Appl. Phys.* **80**, 1312 (1996).
- 32 G.M. Jansen, Stan Ackermans Inst. - I11, Eindhoven University of Technology (1997).
- 33 R.F.G. Meulenbroeks, D.C. Schram, M.C.M. van de Sanden, and J.A.M. van der Mullen, *Phys. Rev. Lett.* **76**, 1840 (1996).
- 34 D.K. Otorbaev, A.J.M. Buuron, N.T. Guerassimov, M.C.M. van de Sanden, and D.C. Schram, *J. Appl. Phys.* **76**, 4499 (1994).
- 35 M.J. de Graaf, PhD thesis, Eindhoven University of Technology (1994).
- 36 see also Chapter 4 of this thesis.
- 37 J.W.A.M. Gielen, M.C.M. van de Sanden, and D.C. Schram, *Appl. Phys. Lett.* **69**, 152 (1996).
- 38 R.J. Severens, G.J.H. Brussaard, M.C.M. van de Sanden, and D.C. Schram, *Appl. Phys. Lett.* **67**, 491 (1995).

2 Langmuir Probe Measurements in the Downstream Plasma

2.1 Introduction

Charged particles play an important role in any plasma. In plasma sources the energy is coupled into the plasma through the acceleration of electrons. In the downstream plasma under investigation, the ions play an important role in the gas phase kinetics (see Chapters 5-8). For example, argon ions are used to create oxygen atoms via charge exchange and dissociative recombination (see Chapter 8). In plasma surface interactions ions can be accelerated towards the substrate by an applied bias or self-bias. This way directionality can be given to the ions making it possible to etch surfaces anisotropically. In some other plasma processing applications the presence of ions is undesirable, so that study of the behavior of ions is important to avoid damage. In this chapter one of the methods to measure the density and energy of charged particles, the Langmuir probe, is investigated. The accuracy of the measurements and the correct interpretation in the use of probes in the downstream plasma are established. This way, the results of Langmuir probe measurements can be used to investigate the behavior and model the kinetics of charged particles in argon/nitrogen, nitrogen and argon/oxygen plasmas in later chapters.

The Langmuir probe is one of the oldest diagnostic tools used in plasma physics. In essence a Langmuir probe is a conductor placed in the plasma. By measuring voltage of and current to the probe, information about the charged particles in the plasma is obtained. The probe can be placed at different positions in the plasma and local variations in the plasma density and temperature are measured. Since probes can be constructed in many different shapes and sizes they have been applied to plasmas with widely varying properties. The electronics involved are straightforward (a simple power supply may suffice) and six or seven orders of magnitude differences in electron density can be measured without great difficulty. The main drawback of a probe is its physical presence in the plasma, thus disturbing the plasma at the very position the measurement is taken. It is therefore of prime importance in the use of probes that its shape and size is adjusted to the properties of the plasma. Careful analysis of these properties of the plasma is then necessary to apply the appropriate theory for the interpretation of the results. Too often results from Langmuir probe measurements are unreliable because of misinterpretation, rather than error in measurement [1, 2, 3].

In a review of different methods to determine electron density and temperature, Meulenbroeks et al. [4] have compared Thomson scattering [5, 6], Langmuir probe and optical emission spectroscopy. Thomson scattering turns out to be the most accurate method, but its disadvantage is that it is a rather complicated and expensive experiment to perform, especially

at electron densities below 10^{19} m^{-3} . Langmuir probe measurements show good correlation with Thomson scattering results in a downstream plasma, but show a systematic difference. It will be shown here that the difference in the determined electron density between Thomson scattering and Langmuir probe found by Meulenbroeks et al. [4] is a result of an error in the application of the theory for Langmuir probes under the conditions present in the downstream plasma. When this is corrected, the Langmuir probe measurements yield electron densities within 10% of the densities found by Thomson scattering.

Optical emission spectroscopy can be used to determine the continuum radiation from the plasma which is proportional to the electron density squared. The best accuracy obtained using this method is 50% (or a factor of 2). Another possibility to determine electron density and temperature from optical emission spectroscopy is to use the highest excited states visible in the plasma. These states are in local Saha equilibrium (cf. Ref. [7]). This method also leads to results with limited accuracy when compared to Thomson scattering. However, recently De Regt et al. [8] have presented transition probabilities for high excited states of argon, which may improve the accuracy of this method. Both methods to determine the electron density from optical emission spectroscopy require the assumption of some equilibrium, the existence of which is often questionable.

Another method to determine the electron density is microwave interferometry [9, 10] in which the change of phase of microwaves transmitted through the plasma is measured. The advantage of this method over Langmuir probes is that it is a non-intrusive method (as mentioned, the physical presence of a probe in the plasma is considered to be the main disadvantage). The disadvantage of microwave interferometry is the fact that it is a line-of-sight measurement and gives the spatial average over the size of the microwave beam. Furthermore, the phase shift of the microwaves only yields information on the density of the electrons, not on their temperature.

All in all, Langmuir probe measurements turn out to be a simple and still rather accurate method to determine electron density and temperature in plasmas similar to the ones under investigation here. Its greatest advantages are probably its low cost and easy applicability, when compared to Thomson scattering, as well as the wide range of applicability. Its biggest disadvantage is the interpretation of the results and the application of the appropriate theory to account for the disturbance of the plasma by the probe. It is the goal of this chapter to investigate the use of probes in the downstream arc generated plasma.

When a voltage is applied to a probe, a current will flow to or from the conductor. If the probe is not heated (on purpose, nor heated significantly by the current flowing through it) and no deposition or etching of the surface takes place, the current to or from the probe is formed by particles coming from the plasma (positive ions, electrons or negative ions). When an electron reaches the probe it will be absorbed, ions will be neutralized. This causes the boundary layer

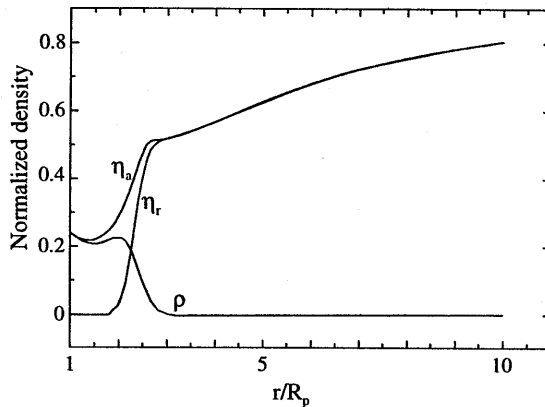


Figure 2.1: Normalized densities of repelled (η_r) and attracted (η_a) particles, and charge density when a cylindrical probe is at a potential of $25kT/e$, with ratio of probe radius to Debye length $R_p/\lambda_D = 10$. The density in the undisturbed plasma equals 1. (Simulation made by Krout [11], after Laframboise [1])

between the undisturbed plasma and the probe to be depleted of charged particles (see Fig. 2.1 [11]). The challenge for correct interpretation of the measurements lies in the choice of the correct theory for the formation of the depletion region.

Ideally, the hydrodynamic transport equations and Poisson's equation are solved under the proper boundary conditions. To solve the complete set of equations is not yet possible for a probe of arbitrary shape or any particle species. However, under specific conditions, the equations may be simplified without much loss of accuracy and solved analytically or numerically. The simplifications and resulting theory that are most appropriate for measurements in the downstream plasma under investigation is the *Theory of cylindrical probes in a collisionless plasma* [1, 12] and will be explained in section 2.2.1. This theory will be applied to measurements in the downstream plasma using cylindrical probes. Under specific conditions the theory may be simplified further and leads to the conventional theory of Langmuir probes as developed originally by Langmuir et al. [13], presented in section 2.2.2. This theory may under the right experimental conditions be applied to probes with shapes other than cylindrical; specifically planar probes will be used and investigated. The determined plasma parameters using different probes will finally be compared in section 2.3.3. The goal of this effort is to determine the accuracy of the theory and the influence of the shape of the probes (cylindrical/planar). It will be shown that under the experimental conditions the shape of the probe has little influence on the accuracy of the determined plasma parameters, as long as the appropriate theory is applied.

In a further investigation of the applicability of probe measurements for the determination of plasma parameters, planar single and double probe measurements are performed in magnetized downstream plasmas. When the plasma is magnetized the electrons will start a precession around and along the magnetic field lines. Thus, the electron mobility perpendicular to the magnetic field lines is reduced. This influences the probe measurements and the determination of the electron density and temperature. The existing theory for probe measurements in a magnetized plasma will be presented in section 2.2.4 and used for the interpretation of experimental results in section 2.3.4. Using the experimental results obtained in magnetized argon plasmas with different size planar probes the theory is adapted for measurements in hydrogen and nitrogen. The goal and final result of this effort is to show how Langmuir probe measurements can be performed in magnetized plasmas to yield the same plasma parameters (electron density, temperature and ion mass) as in non-magnetized plasmas.

2.2 Theory

2.2.1 Theory of Langmuir probes in a collisionless plasma

The behavior of particles in a plasma close to a surface is determined by three parameters (all with dimension length). The mean free path of a particle (λ_{mfp}) gives the average distance the particle can travel without a collision. The Debye length (λ_D) is the screening distance over which charge separation takes place and thus gives the average distance over which an electrical field may exist in the plasma. Thirdly, the size of the surface (usually the probe radius, R_p) gives, relative to the previous two parameters, the measure in which the surface physically disturbs the plasma. In the downstream plasma under investigation in this thesis the electron densities are of the order 10^{16} - 10^{19} m^{-3} and temperatures are in the range 0.1-0.5 eV. Using the range of these values, the Debye length ($\lambda_D = \sqrt{\epsilon_0 k_B T_e / e^2 n_e}$) is of the order 5×10^{-5} - 10^{-6} m. The mean free path for electrons and ions* is of the order 10^{-1} - 10^{-4} m (cf. Ref. [14]) and is always at least one order of magnitude larger than the Debye length. This means that over the distance that the probe induces an electric field (the so-called sheath around the probe) the electrons and ions are collisionless.

* When the ionization degree is high, the mean free path of electrons and ions is the electron-ion and ion-ion mean free path. At very low ionization degree (normally when the electron density is below 10^{17} m^{-3} , depending on the pressure) the mean free path is the ion-atom and electron-atom mean free path.

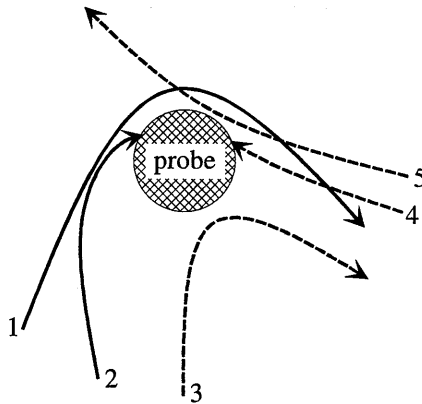


Figure 2.2: Possible trajectories of charged particles around a cylindrical probe. 1.: attracted particle with high angular momentum, 2.: attracted particle with low angular momentum, 3.: repelled particle with insufficient energy to overcome the electric field, 4.: repelled particle with sufficient energy and low angular momentum, 5.: repelled particle with sufficient energy and higher angular momentum

The most complete and self-consistent theory is the *Theory of Spherical and Cylindrical Langmuir Probes in a Collisionless, Maxwellian Plasma at Rest* by J.G. Laframboise [1]. The presumption made by Laframboise is that the mean free path is much larger than the Debye length. This means that in the sheath region, where a potential difference is induced by the probe, no collisions take place. The current to the probe is then determined by the random, Maxwellian flux towards the probe[†] [15]. If a particle that is being repelled has sufficient energy to overcome the potential of the probe it will be absorbed, otherwise it will be reflected. Since angular momentum is also conserved, only particles with sufficiently small angular momentum will be able to reach the probe (this is often referred to as *Orbital Motion Limited* current), see Fig. 2.2. These considerations are translated to a set of differential equations that were solved numerically by Laframboise [1].

In order to make the results of the calculations by Laframboise practically applicable to measurements using cylindrical probes, Peterson and Talbot [12] have fitted a semi-empirical

[†] The collision frequency of electrons is approximately 10^8 s^{-1} , the collision frequency of ions is of the order 10^6 s^{-1} . This means that a large number of collisions will take place in the downstream vessel. This leads to randomization of the energy distributions. There are no processes to significantly heat electrons or ions. The energy distribution will therefore be close to Maxwellian. This was also demonstrated by Thomson scattering [5]. Superelastic collisions with excited particles may heat part of the electrons, leading to an overpopulation of the high-energy part of the electron energy distribution [15]. Since only a small amount of electrons is affected, the Langmuir probe measurements are not influenced significantly

function to the results of the computations of Laframboise for a cylindrical probe. The nondimensional current attracted to a probe is defined as

$$j = \frac{I}{I_0} \quad (2.1)$$

in which I_0 is the random (Maxwellian) current to a probe at the plasma potential and is given by [13]

$$I_0 = \frac{1}{4} n_0 q \left(\frac{8k_B T}{\pi m} \right)^{1/2} A_p \quad (2.2)$$

with n_0 the number density of the charged particle under consideration in the undisturbed plasma, q the charge, T the temperature, m the mass and A_p the surface area of the probe. The semi-empirical function of Peterson and Talbot for the current provided by the attracted particle is given by

$$j = (\beta + |\chi|)^\alpha \quad (2.3)$$

where χ is the nondimensional potential expressed in terms of probe potential V_{probe} (relative to the plasma potential) and the temperature and charge of the attracted particle

$$\chi = \frac{qV_{probe}}{k_B T} \quad (2.4)$$

The parameters α and β depend on the ratio of the temperatures of the attracted and repelled particles and on the ratio of the probe radius to the Debye length. These two parameters (α and β) account for the extent in which the electric field penetrates the plasma and the depletion of particles around the probe. Peterson and Talbot have determined empirical functions to relate α and β to the properties of the plasma and have tabulated the constants needed under different plasma conditions. If $T_e = T_i$, α varies between 0.4 and 0.15 for the range of the ratio R_p/λ_D between 5 and 100. In the same range, β varies between 3 and 16.[‡] The dependence of α and β on R_p/λ_D (when $T_e = T_i$) is given as

$$\alpha = \frac{2.9}{\ln(R_p/\lambda_D) + 2.3} - 0.27 \quad (2.5)$$

$$\beta = 2.35 + 0.135 \cdot [\ln(R_p/\lambda_D)]^3$$

The current of repelled species in a Maxwellian plasma is

$$I = I_0 \cdot e^{-\chi} \quad (2.6)$$

[‡] Note: In the article by Peterson and Talbot figure 1 shows the dependence of α and β on the ratio R_p/λ_D and ratio of the temperature of the attracted to repelled particle θ_d/θ_r . In this figure the value of β with θ_d/θ_r is shown as -1.5. This should be +1.5 according to Table 1 in the same article and according to the data produced by Laframboise.

The total current to a probe is, of course, the sum of the current provided by the repelled and attracted species:

$$I_{probe} = I_{0r} \cdot e^{-\chi} + I_{0a} (\beta + |\chi|)^\alpha \quad (2.7)$$

with I_{0r} and I_{0a} the random current of the repelled and attracted particles, respectively. Note that no distinction has been made between electrons and ions. In the case that $T_e = T_i$ the electrons and ions only differ in mass and charge.[§] The difference in mass influences the random current, I_0 . The ratio of electron to ion current is given by

$$\frac{I_{e0}}{I_{i0}} = \sqrt{\frac{m_i}{m_e}} \quad (2.8)$$

where the subscripts e and i denote electrons and ions, respectively.

2.2.2 Conventional Langmuir probe theory.

For large probes (probe radius is larger than the mean free path) in a plasma with Debye length much smaller than probe dimensions and mean free path, some further simplifications can be made. No longer is the current to the probe limited by the conservation of angular momentum. We can now define a sheath around a probe as the region into which the electrical field of the probe extends. Outside the sheath the plasma is quasi neutral ($n_e = n_i$) and no electric fields are present. Every particle that enters the sheath and is attracted by the probe will (eventually) be absorbed. The repelled particles that have enough energy to overcome the probe potential will also reach the probe surface and be absorbed (neutralized), thus contributing to the current. In this simplified view, the random (Maxwellian) flux into the sheath determines the current absorbed by the probe. The size of the sheath must be calculated in order to find out whether the sheath thickness is indeed much smaller than the probe dimensions so that the orbital motion may be neglected. Furthermore, the total collection area is in this case the sheath area, which must be known to find the density from the measured current. As mentioned above the current to the probe may be written as the random (Maxwellian) current into the sheath analogous to Eq. (2.2)

$$I = \frac{1}{4} n_0 q \left(\frac{8k_B T}{\pi m} \right)^{1/2} A_{sheath} \quad (2.9)$$

with the sheath area A_{sheath} as the collection area (in stead of the probe area, A_p , in Eq. (2.2)). All attracted particles that enter the sheath will then be absorbed. The current of repelled

[§] If $T_e \neq T_i$ the formulas for α and β are different to account for the difference.

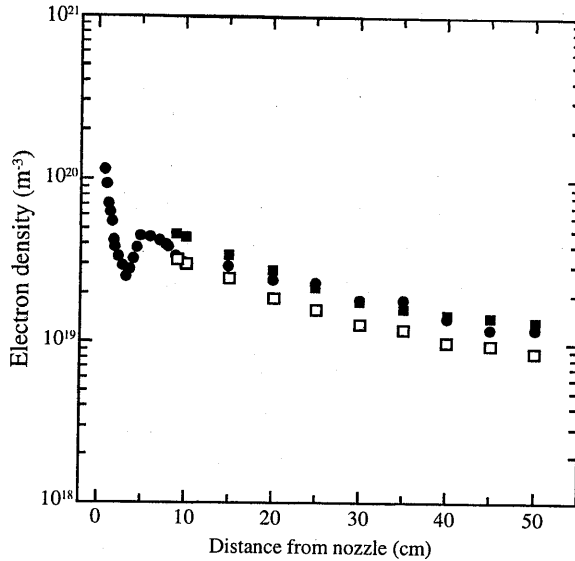


Figure 2.3: Comparison of electron densities obtained by Langmuir probe (■) and Thomson scattering (●). The results from Langmuir probe measurements have been corrected using Eq. (2.9). The original results from [4] are shown as open symbols (□).

particles is still given by Eq. (2.6). This, in fact, is the conventional probe theory developed early this century by Mott-Smith and Langmuir [13].

The simplifications inherent to the conventional Langmuir probe theory lead to some inconsistencies that had to be patched up. One example of this is the applicability of the theory in plasmas with very low ion temperature (compared to the electron temperature). Equation (2.9) is only valid if the velocity (temperature) of the attracted particle is high enough. If the situation exists that the ions are cold ($T_i = 0$), a presheath will be formed (cf. for example [16]) to accelerate the ions to the Bohm velocity [17]. The ion velocity at the sheath edge is then

$$v_{ion} \geq v_{Bohm} = \left(\frac{kT_e}{m_{ion}} \right)^{1/2} \quad (2.10)$$

so that essentially, the electron temperature T_e , rather than the ion temperature determines the ion flux into the sheath. In the downstream (recombining) plasma investigated in this thesis, the electron and ion temperature are equal. The Bohm criterion is then automatically satisfied so that Eq. (2.9) must be used.

In their book on *Electrical Probes for Plasma Diagnostics*, Swift and Schwar [3] derive the dependence of the Bohm criterion on the temperature ratio, T_i/T_e , and find for the current to the probe

$$I_i = \kappa A_{sheath} n_{i0} e \left(\frac{k_B T_e}{m_i} \right)^{1/2} \quad (2.11)$$

where the subscript i denotes the ions and κ is the factor that depends on the ratio of the temperatures. They find that when $T_e = T_i$ the factor κ takes the value 0.565. However, they derive this dependency assuming a mono-energetic ion energy distribution. In the remote plasma there is ample time to redistribute energy among the different species and it is more likely that the ions have a Maxwellian energy distribution. In their comparison of electron densities determined from Thomson scattering and Langmuir probe measurements, Meulenbroeks et al. [4] have used Eq. (2.11) to determine the plasma density. They report a discrepancy between the two methods of 30%. If Eq. (2.9) is used the differences in electron density is less than 10% with no systematic discrepancy. The corrected result is shown in Fig. 2.3.

As mentioned above, the sheath area determines the current of particles to the probe. It is therefore necessary to have an estimate of the sheath size. For cylindrical probes, with ratio of probe radius to Debye length, R_p/λ_D , between 5 and 100, the empirical functions of Peterson and Talbot are best suited for the calculation of the current to the probe. At larger R_p/λ_D , the area of the probe may be used as the total collection area, since the value of α in Eq. (2.3) approaches 0 for large R_p/λ_D . In the investigation of the plasmas in this thesis we have often used planar probes. The probes will be more extensively described in section 2.3. For planar probes, in the case of a collisionless sheath the one-dimensional derivation of the Child law of space-charge-limited current in a plane diode (derived for plasmas in for example [16], adjusted here for Maxwellian energy distribution) yields the current density I_0/A_p

$$\frac{I_0}{A_p} = \frac{4}{9} \epsilon_0 \left(\frac{2q}{m_i} \right)^{1/2} \frac{V^{3/2}}{s^2} \quad (2.12)$$

with V the potential between two electrodes at a distance s . Substituting the current given by Eq. (2.2) gives an expression for the sheath thickness s

$$s = \frac{4}{3} \left(\frac{\pi}{4} \right)^{1/4} \lambda_D \left(\frac{e V_{probe}}{k_B T} \right)^{3/4} \quad (2.13)$$

The sheath thickness in this 1-dimensional derivation scales with the probe potential to the power 3/4. In the results of Talbot and Peterson [12], the dependence of the sheath thickness on the probe potential is smaller (between 0.5 and 0.1). This is due to the fact that the one-dimensional derivation of Eq. (2.12) is not valid for a cylindrical probe. A derivation of

Eq. (2.12) in cylindrical coordinates leads to a differential equation in V that cannot be solved analytically. When analyzing the characteristic of a cylindrical probe, it is therefore more useful to use the results of Talbot and Peterson than an approximation based on the Child law. When using planar probes, the sheath thickness only needs to be taken into account when it becomes of the order of the probe dimensions. So, although a higher order dependency exists of the sheath thickness on probe potential, the I-V characteristic of a planar probe shows much less dependency on the potential than a cylindrical probe with the same area. If the sheath thickness is negligible (i.e. when using a large probe and/or when the probe potential is close to the plasma potential), the sheath area is the surface area of the probe. Equation (2.9) then reduces back to Eq. (2.2).

In summary, conventional Langmuir theory may be applied to probes that are large with respect to the sheath thickness, in which case the increase in sheath size is small compared to the dimensions of the probe.

2.2.3 Double probes

To determine the electron temperature it is sometimes more useful to use a double probe setup, where the voltage is applied between two probes, rather than to one probe with respect to ground. In this setup the two probes together always remain at the floating potential since no net current is flowing to or from the plasma. Assume that both probes have the same surface area, A_p . If no voltage is applied between the two probes, both probes are at the floating potential. Due to the difference in mass (mobility) between ions and electrons, the floating potential always is well below the plasma potential and electrons are repelled [18]. If the voltage on probe 1 is lowered with respect to probe 2, probe 1 will attract more ions. This is compensated by probe 2 (the net current must remain 0) in the way that probe 2 will repel less electrons. If extremely large potentials are not applied, probe 2 will not reach the plasma potential. The electron current to each probe will therefore always be given by Eq. (2.6). Following the derivation by Peterson and Talbot [12] the total current through the probes, I , must be

$$I = I_{e1} + I_{i1} = -I_{e2} - I_{i2} \quad (2.14)$$

with the subscripts 1 and 2 indicating the two probes and the subscripts e and i electron and ion. If we define the applied potential difference, V_a , between the two probes as

$$V_a = V_2 - V_1 \quad (2.15)$$

then

$$\begin{aligned} V_1 &= V_f - V_1' \\ V_2 &= V_f + V_2' \end{aligned} \quad (2.16)$$

with V_1' and V_2' are the potentials with respect to the floating potential V_f . The current through a double cylindrical probe with equal surface area may now be derived from Eqs. (2.3), (2.6) and (2.14) as

$$I = \frac{I_{i1} e^{\frac{eV_a}{k_B T}} - I_{i2}}{1 + e^{\frac{eV_a}{k_B T}}} \quad (2.17)$$

The ion currents are given by Eqs. (2.1) and (2.3) as

$$I_{i1} = I_{i0} \left(\beta - \frac{e(V_f - V_1')}{k_B T} \right)^\alpha$$

$$I_{i2} = I_{i0} \left(\beta - \frac{e(V_f + V_2')}{k_B T} \right)^\alpha \quad (2.18)$$

The difficulty in the interpretation of the double probe characteristic comes from the fact that only the applied potential difference is known, not the potential of each probe with respect to the plasma potential. Expressions for the potentials V' and V_f can be derived in implicit form:

$$\frac{eV_1'}{k_B T} = -\ln \left\{ \left[1 + \frac{eV_1'/k_B T}{\beta - eV_f/k_B T} \right]^\alpha + \left[1 + \frac{eV_1'/k_B T}{\beta - eV_f/k_B T} - \frac{eV_a/k_B T}{\beta - eV_f/k_B T} \right]^\alpha \right\} + \ln [1 + e^{eV_a/k_B T}] \quad (2.19)$$

and

$$eV_f/k_B T = -\frac{1}{2} \ln \left(\frac{m_i}{m_e} \right) + \alpha \ln (\beta - eV_f/k_B T) \quad (2.20)$$

It is clear that these equations are not particularly useful for the evaluation of plasma parameters from a measured I-V characteristic. Peterson and Talbot [12] therefore recommend the following procedure for the evaluation of the double probe characteristic.

The temperature is found from the derivative of the probe characteristic, $\partial I / \partial V_a$, at $V_a = 0$, where both probes are at the floating potential

$$\frac{k_B T}{e} \left(1 + \frac{\alpha}{\beta + |eV_f/k_B T|} \right)^{-1} = \left\{ \frac{I_{i1} I_{i2}}{I_{i1} + I_{i2}} \left(\frac{\partial I}{\partial V_a} \right)^{-1} \right\}_{V_a=0} \quad (2.21)$$

When the areas of the probe are equal, the ion currents at the floating potential become equal and Eq. (2.21) is simplified further. The factor $1 + \alpha / (\beta + |eV_f/k_B T|)$ only slightly depends on temperature and density. It varies between 1.1 and 1 with the ratio R_f / λ_D between 1 and 100. At very large applied potential the current to one of the probes (the one at the most negative

potential) will consist only of the ion current to that probe. To reach a potential V_1' (with respect to the floating potential) of $10 k_B T/e$ the applied potential normalized to T , will be between 10.65 and 10.95 for all values of R_p/λ_D considered. So the ion current can be evaluated at applied potential $10.8 k_B T/e$.

For a double planar probe, under the simplifications discussed in section 2.2.2, the evaluation is more straightforward, since the slope of the saturation current is much smaller. The floating potential may now be approximated as

$$eV_f/k_B T_e = -\frac{1}{2} \ln\left(\frac{m_i}{m_e}\right) \quad (2.22)$$

The ion currents can be linearly extrapolated from the high potential part of the curve to the floating potential and (with the use of Eq. (2.22)) to the plasma potential. The current extrapolated to the plasma potential (where no sheath is present) to each probe is given by Eq. (2.2):

$$I_{is1,2} = \pm \frac{1}{4} \cdot n_{i0} \cdot \sqrt{\frac{8k_B T_i}{\pi m_i}} \cdot q_i \cdot A_{p1,2} \quad (2.23)$$

with $A_{p1,2}$ the surface area of the probe considered and q_i the charge of the ion. For small potentials current is also carried by the electrons and the current through the probes is given by (after Eq. (2.14)):

$$\begin{aligned} I &= I_{e1} - I_{is1} = I_{es1} \cdot e^{\frac{eV_1}{k_B T_e}} - I_{is1} & (V_a < 0) \\ I &= I_{is2} - I_{e2} = I_{es2} \cdot e^{\frac{eV_2}{k_B T_e}} - I_{is2} & (V_a > 0) \end{aligned} \quad (2.24)$$

After rearranging Eq. (2.24) to

$$\frac{I - I_{is1}}{I_{is2} - I} = \frac{A_{p1}}{A_{p2}} \cdot e^{\frac{eV_a}{k_B T_e}} \quad (2.25)$$

an expression for the electron temperature is obtained. Because $T_i \approx T_e$, the ion (or electron) density can be calculated from Eq. (2.23).

2.2.4 Langmuir probes in a magnetized plasma

The situation is considerably more complicated if a magnetic field is applied. When the magnetic field is sufficiently strong the electrons will be confined to the magnetic field lines**.

** In the present investigations, the magnetic field will not be strong enough to magnetize the ions.

The electron current collected by the probe will, due to this confinement, be reduced. Although there have been several theoretical studies [17, 19, 20], there is still no consistent theory to fully explain the reduction. Most widely used is the theory of Bohm [17]

When a magnetic field is applied, the electrons will be forced into a circular motion with a radius, ρ_e , equal to the Larmor radius:

$$\rho_e = \frac{m_e \bar{v}_e}{eB} \quad (2.26)$$

with B the applied magnetic field, and \bar{v}_e the average (Maxwellian) electron velocity. If the Larmor radius becomes smaller than the mean free path of the electron ($\rho_e < \lambda_{mfp}$) the electrons are effectively confined to move along the magnetic field lines. If, under these conditions, the Larmor radius is also smaller than the dimensions perpendicular to the magnetic field of the probe ($\rho_e < R_p$, in the case of a planar probe with the normal of its surface parallel to the magnetic field), the current to the probe is limited by diffusion. The particle flux, $\bar{\Gamma}$, to the probe in this case is given by:

$$\bar{\Gamma} = -\underline{\underline{D}} \cdot \bar{\nabla} n - n \underline{\underline{\mu}} \cdot \bar{\nabla} V \quad (2.27)$$

The diffusivity $\underline{\underline{D}}$ and the mobility $\underline{\underline{\mu}}$ are anisotropic, due to the magnetic field. The diffusion along the magnetic field lines remains unchanged ($D_e = \frac{1}{3} \lambda_{mfp} v_e$), but the components perpendicular to the direction of the magnetic field, D_{\perp} , are reduced:

$$D_{e\perp} = \frac{D_e}{1 + (\lambda_{mfp} / \rho_e)^2} \quad (2.28)$$

It is assumed that Einstein's relation $\mu = eD_e/k_B T_e$ is still valid. For a planar, circular probe with the normal of its surface parallel to the magnetic field the electron saturation current, I_{esll} , becomes [21]:

$$I_{esll} = I_0 \cdot \zeta(B) \quad (2.29)$$

with I_0 the undisturbed, random current given by Eq. (2.2) and a reduction $\zeta(B)$ due to the magnetic field of:

$$\zeta(B) = \left(1 + \frac{\pi}{8} \frac{R_p}{\lambda_{mfp}} \left(1 + (\lambda_{mfp} / \rho_e)^2 \right)^{\frac{1}{2}} \right)^{-1} \quad (2.30)$$

The dependence on the magnetic field in this factor consists of the contribution of the Larmor radius, ρ_e . The ratio of saturation currents becomes:

$$\frac{I_{esll}}{I_{is}} = \sqrt{\frac{m_i}{m_e}} \cdot \zeta(B) \quad (2.31)$$

For the double Langmuir probe, the current to each probe is given by Eq. (2.24). It is easily seen, by inserting the electron current from Eq. (2.29) into Eq. (2.24), that the presence of a magnetic field does not change the characteristics of the double probe if the ions are not magnetized.

2.3 Experiments

2.3.1 Outline of the experiments

It is the goal of the experiments to investigate the applicability of the existing theories to measurements in the downstream plasma. In section 2.3.2 a brief explanation will be given of the experimental setup used. In section 2.3.3. measurements will be performed in the downstream argon plasma in the absence of a magnetic field. Different probe shapes (cylindrical and planar) and setups (single and double) will be compared under similar plasma conditions. It is the goal of this investigation to establish which theory should be used under these conditions. The accuracy of the measurements is investigated to enable reliable measurements in later investigations (Chapters 5-8 of this thesis. Finally, in section 2.3.4. measurements are performed in the magnetized downstream plasma. First, results from measurements in argon will be compared to the existing theory, to determine the applicability of this theory. Measurements in nitrogen and hydrogen will be undertaken in the presence of a magnetic field. From these measurements the ion most abundant in the plasma can be identified. The mass of the ion must be known in order to determine the ion density from the ion saturation current, which is not affected by the presence of a magnetic field.

2.3.2 Experimental setup

For the investigation of the electron temperature and density of the plasma two planar probes and a double cylindrical probe were constructed. The single cylindrical probe is actually one probe of the double probe system. These cylindrical probes are tungsten wires, 3.7 mm long with a diameter of 0.2 mm, and are 2 mm apart. The planar probes (Fig. 2.4) are circular probes made out of tungsten. A probe with a diameter of 4 mm and one with a diameter of 1.8 mm were used. The edges of the probe are shielded off by a ceramic (Al_2O_3) tube. Although it has been argued by Schott [2] that the charge collected on the tube will distort the field in front of the probe in an uncontrollable way, this is thought not to be of great influence in the plasmas under investigation here. The electron density in the plasmas under

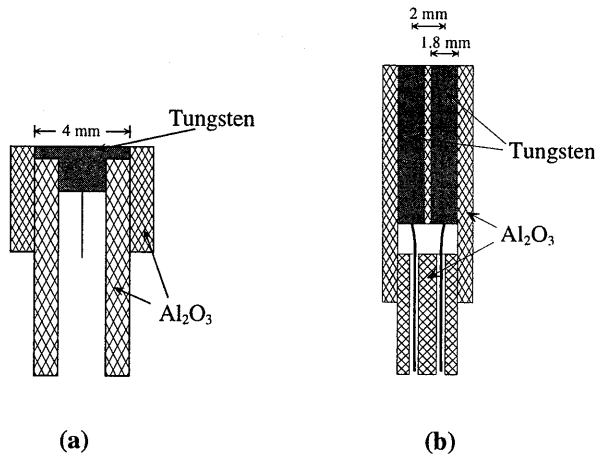


Figure 2.4: Single (a) and double (b) Langmuir probes.

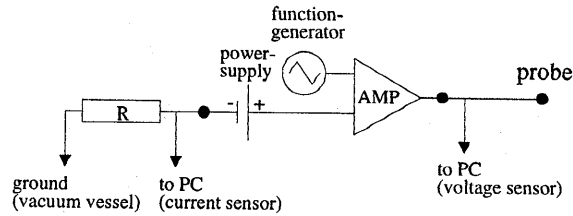
investigation is of the order 10^{17} - 10^{18} m⁻³ and the temperature 0.1-0.5 eV. The Debye length consequently is of the order of 10^{-5} m, i.e. much smaller than the probe diameter. The distortion of the field by the ceramic tube will therefore be limited to an area much smaller than the probe area. An advantage of this design is that no edge effects need to be taken into account. Furthermore, it is possible to use this probe in combination with a laser in photoionization and photodetachment experiments [22] without exposing the probe surface to the laserbeam.

For double planar probe measurements a similar probe design was used (Fig. 2.4(b)) The probe consists of two circular tungsten discs (diameter 1.8 mm) mounted inside a ceramic tube, 2 mm apart. In this setup the current through the probe is measured as a function of applied potential difference. The complete setup is therefore floating with respect to ground.

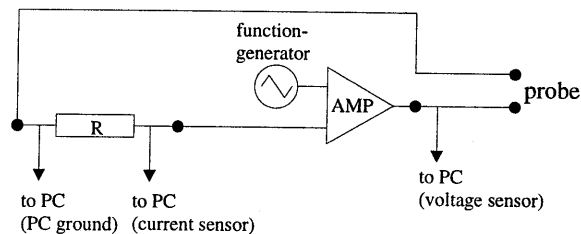
An overview of the electrical circuit for single and double probes is given in Fig. 2.5.

2.3.3 Probe measurements without magnetic field

Four measurements using the probes described above were done in a downstream argon plasma. All measurements were performed at the same position, 30 cm downstream from the nozzle at a radial distance of 5 cm from the axis. The argon flow was set to 3.3 slm (standard liters per minute), the arc current was 45 A and the vessel pressure 14 Pa. The purpose of these experiments is to establish the accuracy of the theories used to interpret the measurement.



(a)



(b)

Figure 2.5: Electrical circuit for measurements with the single probe (a) and double probe (b).

Single cylindrical probe

To determine the relevant plasma parameters from a single probe characteristic, first the plasma potential must be known. So far, all interpretation of current to a probe has been given with respect to the plasma potential. In an experimental setup for single probe measurements the voltage on the probe is measured with respect to a (more or less) arbitrary ground. The plasma potential (with respect to this ground) is determined as the maximum in the first derivative of the characteristic. It is not completely straightforward from the interpretation in the previous section of the current to a probe that the first derivative should have a maximum at the plasma potential, since the approximations are not valid close to the plasma potential. The electron current to the probe below the plasma potential is given by Eq. (2.6). This equation reaches its maximum value at the probe potential because at lower potential the electrons are repelled. At probe potentials above the plasma potential ($V_{probe} > 3kT_e/e$) the current is given by Eq. (2.3) whose derivative also reaches a maximum value at the plasma potential ($\chi = 0$). Close to the plasma potential Eq. (2.3) is no longer valid, but the original results of Laframboise [1] show that the attracted electron current is a monotonously increasing function of the probe potential which also has its maximum at the probe potential. The same (but reversed) situation exists for ions. The derivative of the ion current therefore

		Single cylindrical	Single planar	Double cylindrical	Double planar
Fitted parameters	I_{e0} (mA)	158 ± 10	277 ± 10		
	I_{i0} (mA)	0.60 ± 0.03	1.06 ± 0.04	0.59 ± 0.03	0.55 ± 0.02
	T_e (eV)	0.31 ± 0.02	0.37 ± 0.04	0.38 ± 0.04	0.21 ± 0.04
	R_p/λ_D	45 ± 1			
Calculated parameters	n_e (10^{18} m^{-3})	4.6 ± 0.4	3.3 ± 0.3	4.2 ± 0.4	4.7 ± 0.4
	m_+ (amu)	37 ± 6	37 ± 6		
	R_p/λ_D	52 ± 5			

also reaches a maximum at the plasma potential. In the high voltage parts ($V_{probe} > 3kT_e/e$ and $V_{probe} < -3kT_e/e$) of the probe characteristic the sum of the current of attracted (Eq. (2.3)) and repelled (Eq. (2.6)) species is fitted to the measured characteristic. The free parameters in the fit are the electron saturation current, the ion saturation current, the electron temperature and the ratio of probe radius to Debye length. The result of such a fit is shown in Fig. 2.6(a). The part of the characteristic at negative potential (shown in the inset of Fig. 2.6(a)) has been multiplied by 270 (the square root of the expected mass ratio of ions and electrons) to give it the same weight as the part at positive potential. The fitted parameters are given in Table 2.1. From the electron saturation current at the plasma potential, the electron density is determined using Eq. (2.2). The electron density found is used here to calculate the Debye length, so that the fitted ratio of probe radius to Debye length may be compared to the one calculated from the saturation current. This gives a means of testing the consistency of the method used.

In principle, both electron and ion saturation currents yield the plasma density. The mass of the ions can be determined from the ratio of the two saturation currents, provided the ion saturation current can be determined with sufficient accuracy and no offset is present in the setup. The mass ratio follows from Eq. (2.7). In argon the square root of the ratio of ion to electron mass is 270. In the case that the mass of the ion is known (for example, when using a noble gas such as argon), the square root of the mass ratio forms a second check of the method.

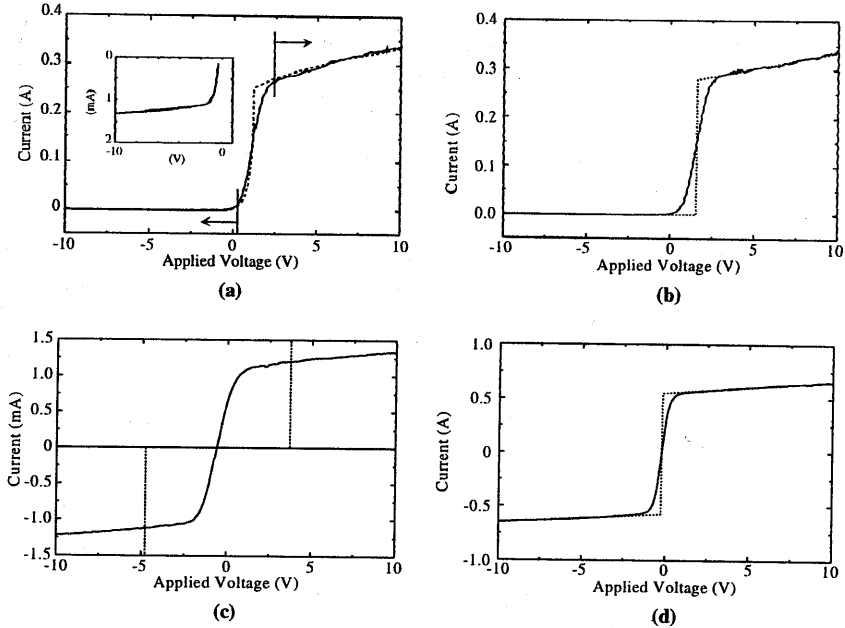


Figure 2.6: Probe characteristics in the downstream argon plasma. The dotted lines indicate fits and/or extrapolations of the characteristics. The different characteristics shown are: (a) Single cylindrical probe, the dotted lines show the fit, the arrows indicate the fitting region. The inset shows the ion current enlarged; the dotted line is not visible due to the quality of the fit. (b) Single planar probe, the dotted lines show the linear extrapolation to the plasma potential. (c) Double cylindrical probe, dotted lines indicate where the saturation current was determined ($V_a = \pm 10.8 k_B T_e/e$). (d) Double planar probe, dotted lines show the linear extrapolation to the floating potential ($V_a = 0$).

The complete analysis of a cylindrical probe is done by the following steps:

1. The plasma potential is determined as the maximum in the derivative of the characteristic
2. The temperature is estimated to determine the part of the characteristic for which the approximate curves of Peterson and Talbot [12] are valid ($V_{probe} > 3k_B T_e/e$ and $V_{probe} < -3k_B T_e/e$).
3. The part of the characteristic below the plasma potential is multiplied by a constant to make it of the same order as the positive part (in the case of argon this constant is 270, the square root of the expected mass ratio of ions to electrons).
4. The equations of Peterson and Talbot are fitted (Eqs. (2.3) and (2.6)).
5. The fitted temperature is compared with the estimated temperature to check whether the fitting range is appropriate (see step 2).
6. The Debye length calculated from the electron density is compared with the fitted ratio of probe radius to Debye length.

Single planar probe

The analysis of a measurement with a planar probe follows a similar scheme. First the plasma potential is found as the value of the maximum of the derivative of the probe characteristic. Since the high voltage parts of the characteristic are almost flat (if the probe is large enough), the saturation currents are found by linearly extrapolating the ion and electron currents to the plasma potential. The slope does not depend uniquely on the electron temperature, so the electron temperature must be determined in a different way than with a cylindrical probe. This is done by subtracting the ion saturation current from the total current, below the plasma potential. Below the plasma potential, the curve now only consists of the repelled electron current given by Eq. (2.6). Plotting this current on a logarithmic scale immediately yields the electron temperature as the slope of the curve. Once the electron temperature and saturation currents are known, the electron density and ion mass can be calculated. A single planar probe measurement and the linear extrapolation of the saturation currents is shown in Fig. 2.6(b). The results of the analysis are given in Table 2.1 where they are compared to the values found by the cylindrical probe measurement.

Double cylindrical probe.

As was shown in section 2.2.3, the interpretation of the double cylindrical probe is somewhat more complex. Following the method suggested by Peterson and Talbot [12], it is done by the following steps:

1. Estimate the ion saturation current at the floating potential by (non-linear) extrapolation.
2. Estimate the temperature using Eq. (2.21) with $\alpha/(\beta + |eV_f/kT|)$ equal to zero.
3. Determine the value of the currents at $V_a = \pm 10.8 k_B T/e$.
4. Calculate V_f using Eq. (2.20). A first estimate of α and β may be obtained from the extrapolated saturation currents at the floating potential.
5. Calculate I_0 from Eq. (2.18), with $V = 10 k_B T/e$.
6. Calculate the electron density and from that determine α and β .
7. Calculate the currents at the floating potential from Eq. (2.18), with $V = 0$.
8. Calculate the temperature from Eq. (2.21).

Steps 3 through 8 may have to be repeated once or twice. The result of a double cylindrical probe measurement is shown in Fig. 2.6(c). The result of the analysis is given in Table 2.1.

Double planar probe

For a double planar probe the analysis is similar to the analysis of the single planar probe. The saturation currents are determined by linear extrapolation of the currents at high voltage.

Equation (2.25) is applied to determine the temperature. After extrapolation of the saturation currents to the plasma potential, thereby using Eq. (2.22) to estimate the value of the plasma potential with respect to the floating potential, Eq. (2.23) is used to determine the ion density. A measurement using the double planar probe is shown in Fig. 2.6(d). The determined parameters are given in Table 2.1.

Comparison and discussion

The results of all four probe measurements are compared in Table 2.1. The single cylindrical probe has the most complete interpretation. It also yields the most complete information about the plasma. The plasma under investigation with its high electron density ($> 10^{19} \text{ m}^{-3}$) and low electron temperature (0.3 eV) is particularly suited for treatment by the theory of Laframboise, since the Debye length is small compared to the mean free path. The fact that the theory is consistent with the experimental results is illustrated by the fair comparison between the ratio of probe radius to Debye length that was fitted and the one calculated from the electron density (45 ± 1 and 52 ± 5 , respectively). As a second check, the mass of the ions found (37 ± 6) is close to the expected value (40 for argon ions). The only difference between the current experiments and the ideal circumstances of the theory of Laframboise is the fact that the expanding thermal plasma is a flowing plasma. In the downstream region, the flow velocity is low ($< 600 \text{ m/s}$) compared to the thermal velocity (1500 m/s for the ions, $4 \times 10^5 \text{ m/s}$ for the electrons) and therefore little influence on the measurements is expected. In conclusion it can be said that the theory of the collisionless plasma at rest is valid for measurements with the single cylindrical probe.

Comparing the results of the different probe methods leads to several interesting observations. The largest discrepancy is found in the determination of the electron temperature. The difference in the temperatures found cannot be explained satisfactorily by experimental error. Since the methods for determining the temperature are very different in nature, it is likely that one or more of these methods will lead to slight under- or overestimation of the temperature. In the case of the single cylindrical probe the temperature is determined from the electron current at fairly high negative potential ($< -3kT$), so that only the most energetic electrons will reach the probe. It seems unlikely that this would lead to an underestimation of the temperature, even though the electron temperature determined with this method is lower than with the single planar and double cylindrical probes. From the present investigation it is not possible to determine the cause of the discrepancy in the determination of the temperature using the different probe methods. Comparison of double cylindrical probe measurements with Thomson scattering by Zhou Qing [23] seem to indicate a systematical overestimation of the electron temperature as determined by the double cylindrical probe. It must be noted,

however, that Zhou Qing uses the theory applied here to double planar probes to interpret his double cylindrical probe results, which makes the comparison difficult.

There also seems to be a systematical difference in the electron density determined by the different probes. If the electron density calculated from the single cylindrical probe characteristic is compared to the density from the double cylindrical probe, the difference can be completely explained by the difference in the determined temperature. This is more clearly illustrated by the ion saturation current (I_{i0}) of each of the probes, which shows they are well within the experimental inaccuracy. The same is true when we compare the single planar and double planar probe. The ion saturation current of the single planar probe is (within the estimated error) twice the current to the double probe. This is a result of the experimental setup used here, where the two parts of the double probe were hooked up in series in the single planar probe measurement, so that the saturation current in the single probe measurement is the current collected by both probe surfaces. If all electron densities found are adjusted, using the same electron temperature, there is a difference in electron density between the cylindrical and the planar probe methods. This is possibly (and most likely) due to the difficulty of positioning the different probes at exactly the same position in the plasma, after removing the other probe.

To summarize, it is found that the theory of the collisionless plasma at rest is applicable to the downstream plasma under investigation (even though it is flowing). The largest uncertainty in the extraction of plasma parameters from the characteristics is the determination of the electron temperature. Differences in temperature are found to be 30%. The electron density can be determined with an accuracy of approximately 20%, most of which is caused by the aforementioned uncertainty in temperature. The saturation current is determined with an uncertainty of only 5%. In some cases, for example when one is interested in the flux of ions to a substrate, separate information on ion density and temperature is not needed. In those cases probe measurements yield very accurate information, comparable to Thomson scattering. Finally, the ratio of saturation currents gives an indication of the ion mass in the plasma.

2.3.4 Probe measurements in magnetized plasmas

The ion density at larger distances from the nozzle can be increased by applying an axial magnetic field [23, 24, 25]. For this purpose a coil around the nozzle provides a diverging magnetic field downstream parallel to the plasma flow with a maximum field strength of 40 mT. Both De Graaf [25] and Zhou Qing [23, 24] noticed deviations from (Saha) equilibrium in the high excited states of hydrogen in the magnetized downstream plasmas. This spurred the investigation of the accuracy of Langmuir probe measurements in magnetized plasmas. Furthermore, Zhou Qing [23] speculated on the influence of negative hydrogen ions,

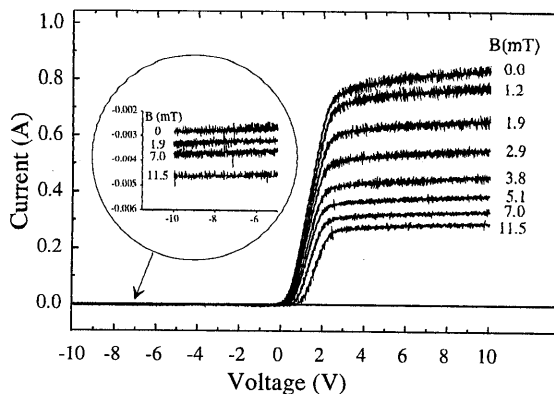


Figure 2.7: Single probe characteristics at different magnetic field strength, measured with a 4 mm probe diameter, in an argon flow of 1 slm. The inset shows the development of ion saturation current with magnetic field.

H^+ in the magnetized hydrogen plasma and the possibility to measure the H^+ density by means of Langmuir probes. To answer these questions and establish the applicability of existing theory for Langmuir probe measurements in the downstream magnetized plasma, measurements were performed in argon, nitrogen and hydrogen plasmas. An overview of all relevant parameters during the experiments is given in Table 2.2.

Argon

To check the validity and applicability of the probe theory in a magnetic field (section 2.2.4), measurements were performed in a pure argon plasma at two different flows (0.3 and 1 slm). The pumping speed was kept constant, resulting in chamber pressures of 11 Pa at 0.3 slm flow and 27 Pa at 1 slm. The two planar probes described in section 2.3.2 were placed with the normal of their surfaces parallel to the magnetic field at a distance of 24 cm from the nozzle.

Ar flow	0.3 and 1 slm
N ₂ flow	1.4 slm
H ₂ flow	2 slm
Arc current	50 A
Chamber pressure	10-30 Pa
Magnetic field	0 - 18 mT

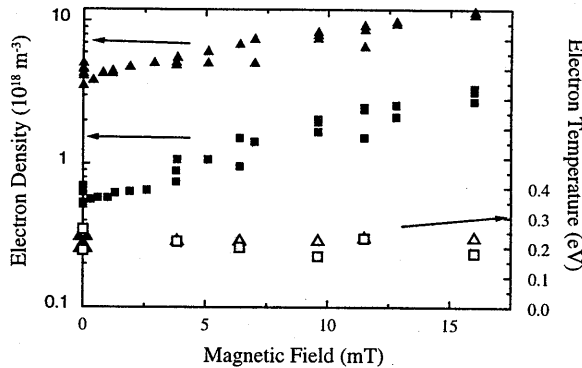


Figure 2.8: Electron density and electron temperature measured by Langmuir double probe. Squares are measurements in a flow of 0.3 slm (\blacksquare for n_e , \square T_e); triangles are results in a flow of 1 slm (\blacktriangle n_e , \triangle T_e).

Measurements were made at magnetic fields between 0 en 16 mT. The probe characteristics at different magnetic fields at an argon flow of 0.3 slm, measured by the larger probe (4 mm diameter) are shown in Fig. 2.7. The electron densities and temperatures measured by the double probe are shown in figure 2.8. The ratio of electron to ion saturation currents as a function of the magnetic field for flows of 0.3 and 1 slm is shown in Figs. 2.9(a) and 2.10(a), respectively. The same ratios are shown as a function of Hall parameter, λ_{mfp}/ρ_e , in Figs. 2.9(b) and 2.10(b).

As can be seen in Fig. 2.9 the current ratios in the absence of a magnetic field range between 290 and 350. The theory of a probe with a collisionless sheath as described in section 2.2 predicts a value of 270 (see Eq. (2.8)). The mean free path for electron-ion collisions is 1.6 mm at 0.3 slm flow (11 Pa) and 0.3 mm at 1 slm flow (27 Pa). The mean free path for collisions with neutrals is much larger (> 2 cm at $p = 27$ Pa, $T_e = 0.25$ eV). The Debye length is of the order of 10^{-6} m in both plasmas. Under these conditions the assumption of a collisionless sheath can be made. The slight discrepancy between the theoretically predicted ratio of electron to ion saturation current of 270 and the experimental result of 320 ± 30 is possibly caused by the probe geometry.

With electron temperature and density measured by the double probe as input parameters, Eq. (2.30) was used to calculate the ratio of electron to ion saturation current at different values of the magnetic field. The results of these calculations are also shown in Figs. 2.9 and 2.10. In the case of the higher (1 slm) argon flow (Fig. 2.10) confinement is reached at a higher magnetic field, due to the smaller mean free path caused by a higher electron (ion)

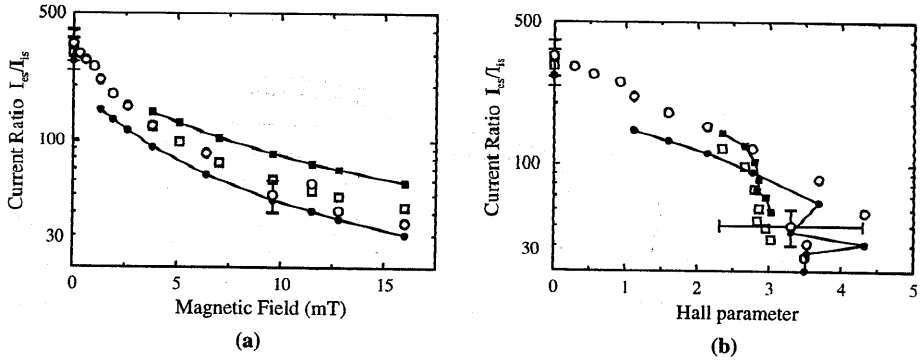


Figure 2.9: Current ratio as a function of magnetic field (a) and as a function of Hall parameter (b) in an argon plasma with a total flow of 0.3 slm. \circ (measurements), and \bullet (calculations) are results for a 1.8 mm probe diameter. \square (measurements), and \blacksquare (calculations) are results for a 4 mm probe diameter.

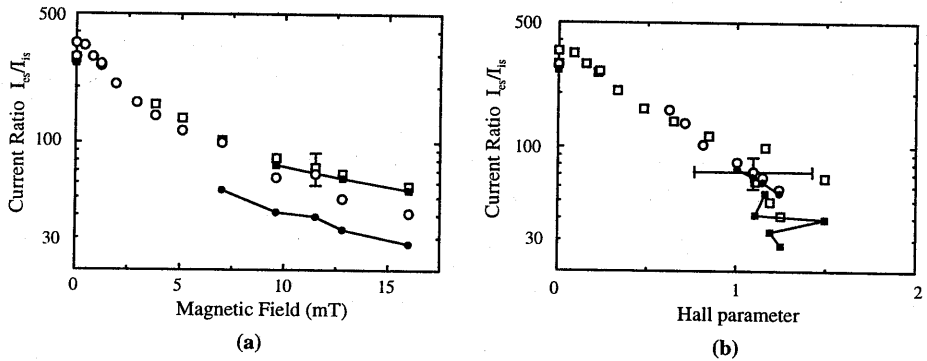


Figure 2.10: Measurements and calculations in an argon plasma with a total flow of 1 slm. The symbols are equivalent to those of Fig. 2.9 (a) and (b).

density. Therefore Eq. (2.31) becomes valid at higher magnetic fields. The theoretical values at $B = 0$ are calculated using Eq. (2.8).

It can be seen in the Figs. 2.9 and 2.10 that there is qualitative agreement between theory and the experiments performed. The dependence on probe radius as predicted in Eq. (2.30) is not observed for either of the two flows. A possible explanation may be found in the fact that the flow of the plasma was neglected in the derivation of the equations. In the theory as explained in section 2.2.4 the electrons in the volume directly in front of the probe diffuse along the magnetic field lines towards the probe. As a result the volume in front of the probe is strongly depleted of electrons due to absorption of these electrons by the probe. The current to the

probe is then determined by diffusion of particles perpendicular to the magnetic field lines into the depleted. So, in effect the electron current to the probe is limited by diffusion perpendicular to the magnetic field lines over an area that scales more or less with the probe radius rather than the probe surface. Hence, the correction $\zeta(B)$ contains a factor proportional to the probe radius, R_p . In the flowing plasma, however, there is a constant supply of electrons flowing in the direction of the probe, and moving along the magnetic field lines. This flow must now be compared to the diffusion of electrons perpendicular to the magnetic field lines (and not to the random Maxwellian flux as was the case in the measurements without magnetic field, section 2.3.3) The flow of particles increases the flux of particles to the probe, which has the normal to its surface parallel to the flow. This contribution is larger for larger probes and could thus cancel out the effect of a larger probe radius in Eq. (2.30).

In order to be able to describe the dependency of the current ratio on the applied magnetic field empirically, the probe radius dependency was removed from Eq. (2.30). A variable, ℓ , is now introduced as a fitting parameter:

$$\zeta^*(B) = \left(1 + \frac{\pi}{8} \frac{\ell}{\lambda_{mfp}} \left(1 + (\lambda_{mfp} / \rho_e)^2 \right)^{1/2} \right)^{-1} \quad (2.32)$$

The best fit is obtained with $\ell = 1.2 \pm 0.2$ mm. Using this value the difference between theory and measurements is less than 20% for both flows and both probe radii.

Nitrogen

If it is assumed that the empirically derived equation (Eq. (2.32)) and value for ℓ are also valid for gases other than argon it is possible to use the probe in the investigation of other, more complicated, magnetized plasmas. One of the plasmas of interest in surface modification and deposition studies is the nitrogen plasma (see also Chapters 5 through 8 of this thesis). A pure nitrogen plasma was created with a total flow of 1.4 slm at a background pressure in the vessel of 23 Pa. The electron densities vary between $0.7 \times 10^{17} \text{ m}^{-3}$ at $B = 0$ and $5 \times 10^{17} \text{ m}^{-3}$ at $B = 4.5$ mT. The measured ratio of saturation currents at different values of the magnetic field is shown in Fig. 2.11. Because under the present conditions nitrogen forms two possible ions (N^+ and N_2^+) the current ratio will be determined by the relative densities of these ions [26]:

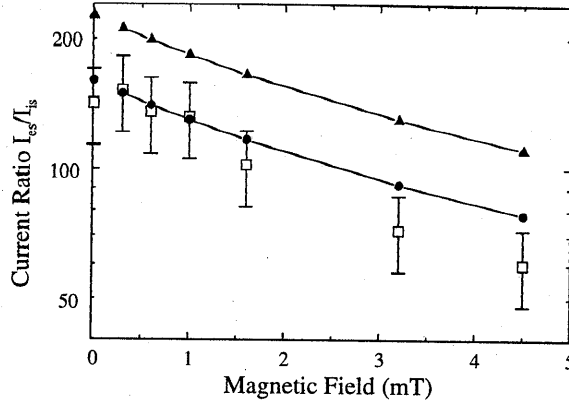


Figure 2.11: Results from the nitrogen plasma with a total flow of 1.4 slm. □ are measured values. The solid symbols are results from calculations assuming that all ions are N^+ (●) and N_2^+ (▲) respectively.

$$\frac{I_{es}}{I_{+s}} = \sqrt{\frac{m_{N^+}}{m_e}} \cdot \left(\frac{n_+}{n_{N^+} + n_{N_2^+} \sqrt{\frac{1}{2}}} \right) \cdot \zeta^+ \quad (2.33)^{\dagger\dagger}$$

with n_{N^+} and $n_{N_2^+}$ the N^+ and N_2^+ densities, and n_+ the total ion density. In Fig. 2.11 the calculated current ratios are given for two distinct cases: $n_{N^+}/n_+ = 1$ and $n_{N^+}/n_+ = 0$. It is clear that a best fit would yield $n_{N^+}/n_+ = 1$. Taking into account the accuracy derived in the previous section it is possible to conclude that in this magnetized plasma the atomic ion N^+ is the dominant ionic species. This result is in good agreement with mass spectrometry measurements performed by Dahiya et al. [27] and Kessels et al. [28], and with the results of the investigation of the kinetics of the downstream nitrogen plasma in Chapter 7 of this thesis.

Hydrogen

An even more complex plasma is the hydrogen plasma. Hydrogen is known to form many different ions H^+ , H_2^+ , H_3^+ and even larger ionic molecules [29]. Besides these positive ions hydrogen can also lead to the stable negative ion H^- . This makes it impossible to make a full quantitative analysis of the distribution of the charged particles in hydrogen using the method

^{††} Equation (2.33) is different from the equation given in the original publication [26]. Since only the limiting cases $n_{N^+}/n_+ = 1$ and $n_{N^+}/n_+ = 0$ are considered, there is no difference in the result.

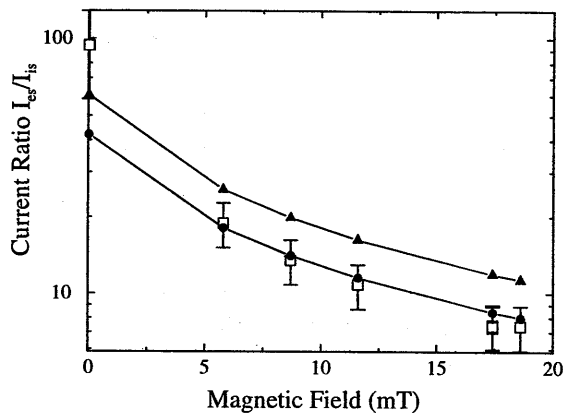


Figure 2.12: Results from the hydrogen plasma with a total flow of 2 slm. □ are measured values. The solid symbols are results from calculations assuming that all ions are H^+ (●) and H_2^+ (▲) respectively.

described. However, some qualitative conclusions can be drawn from an investigation of the saturation currents.

In Fig. 2.12 the saturation current ratio in a pure hydrogen plasma, at a distance of 16 cm from the nozzle, at a flow rate of 2 slm and a chamber pressure of 23 Pa, is shown as a function of magnetic field. The electron densities vary between $0.1 \cdot 10^{17} \text{ m}^{-3}$ and $14 \cdot 10^{17} \text{ m}^{-3}$ for magnetic fields between 0 and 18 mT. Without going fully into the theories that exist about probe analysis in the presence of negative ions [30], it is possible to estimate from the current ratios whether or not H^- is the main negative particle collected by the probe. Because of the difference in mobility between electrons and H^- , the density of H^- needs to be a factor of 10 higher than the electron density for the ion to affect the measured probe characteristic. If H^- would be the dominant negative particle collected by the probe, the ratio of saturation currents at $B = 0$ would be between 1 and 2, depending on the distribution of positive ion densities (H^-/H^+ would yield a current ratio of 1, H^-/H_3^+ would yield 1.7). At increased magnetic field this ratio would remain within this range because neither of the ions (positive or negative) is yet confined. As all of the above predicted observations are not found in the measurements it is concluded that the dominant negative particle in the probe measurements is the electron rather than the negative ion.

The saturation current in this case becomes (see also Eq. (2.33)):

$$\frac{I_{cs}}{I_{+s}} = \sqrt{\frac{m_{H^+}}{m_e}} \cdot \left(\frac{n_+}{\sum_{p=1} n_{H_p^+} \sqrt{\frac{1}{p}}} \right) \cdot \zeta^*(B) \quad (2.34)$$

with p the number of atoms in an ion and $n_{H_p^+}$ the density of the H_p^+ ion. In Fig. 2.12 the calculated current ratios are given for $n_{H^+}/n_+ = 1$ and $n_{H_3^+}/n_+ = 1$. From Fig. 2.12 it is concluded that in the magnetized hydrogen plasma the dominant ion is H^+ . When no magnetic field is applied ($B = 0$ in Fig. 2.12) the ratio of saturation currents is significantly higher. Due to the absence of the magnetic field, the electron density downstream will be lower. It is therefore likely that in this case the dominant ion will be H_3^+ as the ratio of saturation currents at $B = 0$ indicates.

2.4 Conclusions

2.4.1 Probe measurements without magnetic field

The theory of a collisionless plasma at rest is valid for measurements with the single cylindrical probe in the downstream plasma. The probe characteristic predicted by the theory fits well to the experimentally determined curve. The results are self-consistent in the way that the fitted ratio of probe radius to Debye length is close to the ratio calculated using the (fitted) electron density. Furthermore, the (square of the) ratio of electron to ion saturation current yields the correct value for the mass of the ion. When the correct theory is applied for the interpretation of measured probe characteristics, the electron density determined from Langmuir probe measurements compare well with Thomson scattering results.

In the comparison between the different probes, the largest uncertainty in the extraction of plasma parameters from the characteristics is the determination of the electron temperature. Differences in temperature are found to be 30%. The electron density can be determined with an accuracy of approximately 20%, most of which is caused by the uncertainty in temperature. With this investigation of Langmuir probe measurements in the downstream plasma, a firm basis is provided for further measurements. The results of probe measurements in the remote arc generated plasma can be used to determine plasma kinetics (which ions are present?), model the processes in the plasma (what are the densities of electrons and ions, and consequently what are the rates of the reactions that involve these particles?) and investigate plasma-surface interactions in which charged particles are involved (what is the flux of charged particles to a substrate and what is the energy of these particles?).

2.4.2 Probe measurements in the magnetized plasma

The influence of magnetic confinement of electrons on the probe characteristic was investigated in an argon plasma. The dependency on probe radius of the ratio of electron to ion saturation currents as predicted by the theory was not observed. Therefore the theory was used to derive an empirical formula that describes the ratio of electron saturation to ion saturation current. Under the assumption that this empirical formula remains valid in plasmas with a different composition, it was possible to derive which ion is the most abundant ion in magnetized nitrogen and hydrogen plasmas. Information on the ion mass is necessary for correct interpretation of double probe measurements. The composition, density and energy of the ions and electrons as determined from probe measurements can now be used to calculate rates of recombination and the possible formation of radicals in the magnetized downstream plasma.

References

- 1 J.G. Laframboise, University of Toronto, Institute for Aerospace Studies. Report No.100, (1966).
- 2 L. Schott in *Plasma Diagnostics* (ch.11), ed. W. Lochte-Holtgraven, North-Holland, Amsterdam (1968).
- 3 J.D. Swift, and M.J.R. Schwar, *Electrical Probes for Plasma Diagnostics*, Iliffe Books Ltd., London (1970).
- 4 R.F.G. Meulenbroeks, M.F.M. Steenbakkers, Z. Qing, M.C.M. van de Sanden, and D.C. Schram, *Phys. Rev. E* **49**, 2272 (1994).
- 5 M.C.M. van de Sanden, G.M. Janssen, J.M. de Regt, D.C. Schram, J.A.M. van der Mullen, and B. van der Sijde, *Rev. Sci. Instrum.* **63**, 3369 (1992).
- 6 M.C.M. van de Sanden, PhD Thesis, Eindhoven University of Technology (1991).
- 7 J.A.M. van der Mullen, *Phys. Rep.* **191**, 109 (1990).
- 8 J.M. de Regt, R.D. Tas, J.A.M. van der Mullen, B. van der Sijde, and D.C. Schram, *J. Quant. Spectrosc. Radiat. Transfer* **56**, 67 (1996).
- 9 K.A. Graf, and J.H. de Leeuw, *J. Appl. Phys.* **38**, 4466 (1967)
- 10 S.G. Ohler, B.E. Gilchris, and A.D. Gallimore, *IEEE Trans. Plasma Sci.* **23**, 428 (1995).
- 11 R. Krout, internal report VDF/NT 96-34, Eindhoven University of Technology (1996).
- 12 E.W. Peterson, and L. Talbot, *AIAA Journal* **8**, 2215 (1970).
- 13 H. Mott-Smith and I. Langmuir, *Phys. Rev.* **28**, 727 (1926).
- 14 V.M. Lelevkin, D.K. Otorbaev, D.C. Schram, *Physics of non-equilibrium plasmas*, North-Holland, Amsterdam (1992).
- 15 M. Capitelli, G. Colonna, A. Gicquel, C. Gorse, K. Hassouni, and S. Longo, *Phys. Rev. E* **54**, 1843 (1996).
- 16 M.A. Lieberman, and A.J. Lichtenberg, *Principles of plasma discharges and materials processing* (ch. 6), John Wiley & Sons Inc., New York (1994).
- 17 D. Bohm, E.H.S. Burhop, and H.S.W. Massey, *The Characteristics of Electrical Discharges in Magnetic Fields* (ch. 2), ed. by A. Guthrie and R.K. Wakering, McGraw-Hill Book Company Inc., New York (1949).

- 18 E.O. Johnson and L. Malter, *Phys. Rev.* **80**, 58 (1950).
- 19 R.J. Bickerton and A. von Engel, *Proc. Phys. Soc. London* **B69**, 468 (1956).
- 20 J.R. Sanmartin, *Phys. Fluids* **13**, 103 (1970).
- 21 T. Dote, H. Amemiya and T. Ichimiya, *Jpn. J. App. Phys.* **3**, 789 (1964).
- 22 M. Bacal, G.W. Hamilton, A.M. Bruneteau and H.J. Doucet, *Rev. Sci. Instrum.* **50**, 719 (1979).
- 23 Zhou Qing, PhD thesis, Eindhoven University of Technology (1995).
- 24 Zhou Qing, D.K. Otorbaev, G.J.H. Brussaard, M.C.M. van de Sanden, and D.C. Schram, *J. Appl. Phys.* **80**, 1312 (1996).
- 25 M.J. de Graaf, PhD thesis, Eindhoven University of Technology (1994).
- 26 G.J.H. Brussaard, M. van der Steen, M. Carrère, M.C.M. van de Sanden, and D.C. Schram, *Phys. Rev. E* **54**, 1906 (1996).
- 27 R.P. Dahiya, M.J. de Graaf, R.J. Severens, H. Swelsen, M.C.M. van de Sanden and D.C. Schram, *Phys. Plasmas* **1**, 2086 (1994).
- 28 W.M.M. Kessels, C.M. Leewis, T.L. Lauinger, M.C.M. van de Sanden, and D.C. Schram, to be published (1999).
- 29 E. Graham, D.R. James, W.C. Keever, I.R. Gatland, D.L. Albritton and E.W. McDaniel, *J. Chem. Phys.* **59**, 4648 (1973).
- 30 H. Amemiya, *J. Phys. D: Appl. Phys.* **23**, 999 (1990).

3 Determination of the Dissociation Degree in a Hydrogen Plasma by Electron Beam Induced Fluorescence

3.1 Introduction

In many applications of the remote plasma the hydrogen atom plays an important role in the plasma kinetics, in particular in plasmas for deposition of thin layers containing silane, methane, etc. [1]. By itself hydrogen atoms play an important role in surface modification processes [2, 3]. Knowledge of the hydrogen atomic density is therefore necessary to be able to understand these processes. Since the vast majority of hydrogen atoms are in the electronic ground state, they will not emit any light. Normal actinometry to determine the hydrogen atom density is difficult in the recombining plasma under investigation, due to significant deviations from equilibrium [4]. Active, RF probe induced actinometry excites the atoms to higher states. Optical emission spectroscopy is used to detect the emitted light from the subsequent radiative decay [5]. This method has been successfully applied by De Graaf [5] to determine the dissociation degree in arc generated hydrogen plasmas. Its biggest disadvantage is that it is an intrusive method in the sense that the probes disturb the plasma. Active spectroscopic methods are therefore preferred. Determination of the density of hydrogen atoms in the ground state is possible by direct VUV absorption [6], where the absorption of light from an UV light source is measured when it is passed through the plasma. Some disadvantages of this method are the relatively poor sensitivity (changes in light intensity are measured with respect to zero absorption); it is a line-of-sight measurement so that inversion of several measurements is necessary to determine local densities; the optics involved with VUV measurements are rather complex. Two-photon atomic laser induced fluorescence (TALIF) [7, 8] is considered to be the most accurate and least intrusive method to determine atomic hydrogen densities. In a TALIF measurement a pulsed laser with a wavelength of 205 nm is used to excite the atoms from the ground state into the $p = 3$ state ($1s \rightarrow 3s$ or $3p$). An important advantage of the method is its spectral selectivity. Only the resonant transition to the $p = 3$ state is significantly populated. Apart from the density of the ground state atoms TALIF also yields information on the temperature and velocity of the atoms. The energy gap between $p = 1$ and $p = 3$ is 12.09 eV. Two photons of 205 nm are therefore necessary to enable this transition, which means that the probability of the transition is low. To obtain enough signal a high power laser is needed, which carries with it considerable cost. Another disadvantage of this method is the difficulty of translating the signal into absolute densities. For absolute calibration a flow tube reactor is used with NO titration [9]. Systematic errors are hard to exclude from such a calibration. VUV absorption may be used as an alternative

calibration method, but it also has the disadvantages mentioned earlier. In this chapter a newly developed diagnostic tool to detect hydrogen atoms will be presented based on Electron Beam Induced Fluorescence (EBIF).

EBIF was developed in the 1960s by Muntz [10, 11] to study the rotational and vibrational distribution of nitrogen and oxygen gas in flowing nitrogen. It has also been used to study the recombination of nitrogen desorbing from surfaces [12, 13]. In these experiments high-energy electrons ionize neutral nitrogen molecules. Part of the ionized species will be in the electronically excited $N_2^+(B^2\Sigma_u^+)$ which will radiatively decay to the electronic ground state of the molecular ion. Since the ionization reaction and subsequent radiative decay are very fast, the rovibrational distribution of the original molecule will be preserved and can be determined from the emission spectrum.

In the hydrogen plasma we will use an electron beam with electrons in the keV range to excite the atoms from the ground state into different excited states. The fluorescent light from these excited states is a measure for the atom density. The largest difficulty is formed by the presence of neutral hydrogen molecules that will also be dissociatively excited by the high-energy electrons. To distinguish between the emission coming from dissociatively excited molecules and the directly excited atoms a collisional radiative model (CRM) has been formulated. Comparison between measurements in the plasma and in the neutral gas without plasma yields the dissociation degree of the plasma at the intersection of the electron beam with the line of sight of the emission spectroscopy setup. This method does not have the spectral selectivity of TALIF, but this can be corrected by using a correct CRM. It is a crossed beam experiment (as is TALIF) so that local densities are measured. Since the width of the electron beam is larger than the detection volume of the optical emission spectroscopy, absolute densities can be measured after (the relatively straight forward) calibration of the emission spectroscopy setup. Another advantage of EBIF is that it can, in principle, be extended easily to measure dissociation degree in other plasmas in diatomic gases, such as nitrogen and oxygen and even silane, methane etc. A disadvantage of hydrogen atom density measurements by EBIF in the current setup is that it is limited to low pressure (< 200 Pa) and high dissociation degree (> 1%). These restrictions are mainly due to the technical specifications of the electron gun used and can be improved in future setups, as will be discussed at the end of this chapter. In the current setup, EBIF should be considered as a method complimentary to TALIF, as it is most sensitive where TALIF poses most experimental problems (high atom density).

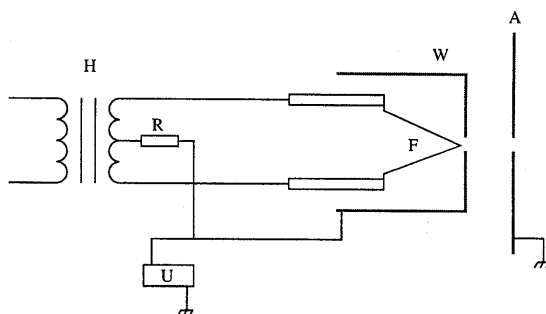


Figure 3.1: Triode gun assembly. *H*: heating current supply; *R*: Wehnelt resistance; *U*: high voltage supply; *F*: tungsten filament; *W*: Wehnelt cylinder; *A*: Anode.

3.2 Experimental Setup

The electron beam setup is shown in Fig. 3.1. The electron beam source is a triode gun configuration, a conventional source for electron microscopy (on loan from the faculty of physics of Delft University). A heating current of approximately 3 A passes through the tungsten filament (*F*). In front of the filament is the Wehnelt cylinder (*W*). This cylinder is connected directly to the high voltage supply. The voltage can be varied between -500 V and -40 keV, but due to the relatively high pressure in the current setup the voltage was normally kept above -6 keV. The filament is kept at a slightly higher voltage (approximately 100 V above the voltage of the Wehnelt cylinder) to restrict the emission of electrons to the tip of the filament. After passing through the hole in the Wehnelt cylinder the electrons are accelerated to the anode (*A*), which is grounded. In the anode is a second pinhole through which the electrons pass to enter the vessel. At a given setting of the Wehnelt resistance, the distance between the cylinder and the anode determines the emission current. In the investigation described in this chapter, the high voltage is typically set at 5 keV, the Wehnelt resistance (*R*) is set at 100 k Ω and the distance between Wehnelt cylinder and anode is set to give an emission current between 0.5 and 1 mA.

Figure 3.2 shows schematically the plasma setup. The cascaded arc and downstream vessel are as explained in Chapter 1 of this thesis. The electron gun is mounted on top of the vessel. The volume in which the tungsten wire tip is situated (up to the pinhole in the anode) is pumped separately from the plasma vessel by a dry turbo molecular pump with forepump (Edwards 120SXC). The pressure inside the electron gun depends on the pressure inside the vessel but is always kept below 10^{-2} Pa to prevent a premature breakdown of the tungsten wire, which is especially sensitive to contamination by hydrogen. After passing through the pinhole in the

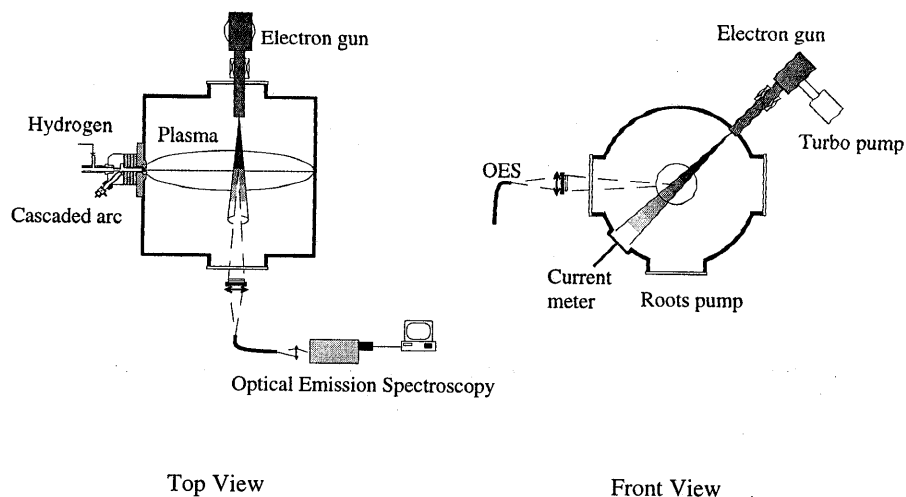


Figure 3.2: Setup for the investigation of the downstream hydrogen plasma with electron beam and optical emission spectroscopy.

anode, the electron beam is focussed by a magnetic Winkler lens before entering the plasma vessel. The beam is aligned to pass through the center of the vessel (and the expansion axis of the plasma) by positioning some small permanent magnets around the point where the beam enters the vessel. On the opposite side the electron beam falls on a circular copper plate where the beam current is measured. The exit of the electron beam is located 24 cm downstream from the exit of the nozzle. The centerline of the beam is at an angle of 45° with the axis of detection of the optical emission spectroscopy and passes through the expansion axis of the plasma. The optical emission spectroscopy setup can be moved horizontally along the expansion axis of the plasma and vertically, perpendicular to this axis (see Fig. 3.2). The spectroscopy setup is focussed on the expansion axis, so that at 24 cm downstream it is focussed exactly on the intersection of the expansion axis of the plasma and the centerline of the electron beam.

3.3 Theory

3.3.1 Excited states in the hydrogen plasma (plasma on, electron beam off)

In the downstream hydrogen plasma a certain distribution of excited states exist. The excited states are produced by recombination of ions with electrons and possibly chemical interactions

between the particles. Due to low electron temperature (0.1-0.5 eV) direct excitation from the ground state or dissociative excitation of molecules can be neglected in the downstream plasma in comparison with excitation by means of recombination processes [14]. The initial distribution is redistributed by collisions (with electrons) and radiative decay. In general the distribution can be described by a complete set of rate equations for each state, taking into account all processes leading to this state and transport by flow and diffusion in the plasma. If the redistribution among the states is much faster than typical transport times these states are in Quasi Steady State (QSS) [15, 16]. In that case transport terms may be neglected and the rate of change of each state equals zero. The rate equation for a particle in excited state p then becomes

$$\frac{\partial n_p}{\partial t} = \sum_{q>p} n_q A_{qp} - n_p \sum_{q<p} A_{pq} + n_e \sum_{q \neq p} n_q K_{qp} - n_e n_p \sum_{q \neq p} K_{pq} - n_e n_p K_{p,ion} + n_e n_{H^+} R_{2,p} + n_e^2 n_{H^+} R_{3,p} + C_p = 0 \quad (3.1)$$

with n_p the density of the excited state p , A_{qp} the transition probability of the transition from state q to state p [17], n_e the electron density, K_{qp} rate coefficient of the collisional (de-)excitation [18], $K_{p,ion}$ the rate coefficient for collisional ionization [18], n_{H^+} the density of the atomic ions, $R_{2,p}$ and $R_{3,p}$ the two and three particle recombination rates and C_p all other recombination or chemical reactions leading to state p . In the hydrogen plasma under investigation, the main recombination mechanism is dissociative recombination (see also Chapters 5-7), leading to population of state $p = 2$. However, we will see later that the terms C_p cancel out in the eventual determination of the dissociation degree.

A more convenient way to present (and solve) Eq. (3.1) is to first write them in matrix form

$$\left(\underline{A} + n_e \underline{K}^{exc} + n_e \underline{K}^{ion} \right) \cdot \underline{n} = n_e n_{H^+} \underline{R}_2 + n_e^2 n_{H^+} \underline{R}_3 + \underline{C} \quad (3.2)$$

with \underline{A} the matrix for radiative decay, \underline{K}^{exc} and \underline{K}^{ion} the matrices for (de-)excitation and ionization by electron impact (cf. appendix for a description of these matrices), \underline{R}_2 and \underline{R}_3 the vectors containing the rate coefficients for two- and three-particle recombination, and \underline{C} the vector containing all other production terms. As mentioned above, this equation is only valid for particles in QSS. For atoms in the ground state this condition usually is not met. As mentioned earlier, in the recombining plasma with electron temperatures of a few tenths of an eV, there is no significant excitation by electron impact from the ground state to higher excited states. This means that there is no depopulation of the ground state. In other words, the ground state density is determined by radiative decay and collisional de-excitation from higher levels, convection from the production region upstream and transport towards the walls of the vessel. At a fixed position in the plasma, the ground state density n_1 must therefore be taken as input in the set of rate equations given by Eqs. (3.1) and (3.2). This will lead to a modified version of Eq. (3.2) for the states $p \geq 2$:

$$\left(\underline{A} + n_e \underline{K}^{exc} + n_e \underline{K}^{ion} \right) \cdot \underline{n} = n_e n_{H^+} \underline{R}_2 + n_e^2 n_{H^+} \underline{R}_3 + \underline{C} + n_e n_1 \underline{k}^{exc} \quad (3.3)$$

with n_1 the density of the ground state atoms, and \underline{k}^{exc} the vector containing the rate coefficients for collisional excitation from the ground state to the states $p \geq 2$ [18]. In some cases (when the density of ground state atoms, n_1 , is high) also the first excited state, $p = 2$, is not in quasi steady state. In that case the left hand side of Eq. (3.3) contains only the terms for $p \geq 3$ and an extra term with the density of the first excited state, n_2 , is added on the right hand side of Eq. (3.3). For the lower excited states ($p < 6$), the collisional terms on the left hand side of Eq. (3.3) are negligible compared to the radiative decay (see also the appendix to this chapter). Equation (3.3) can therefore be simplified to

$$\underline{A} \cdot \underline{n} = n_e n_{H^+} \underline{R}_2 + n_e^2 n_{H^+} \underline{R}_3 + \underline{C} + n_e n_1 \underline{k}^{exc} \quad (3.4)$$

If the density of the terms on the right hand side of Eq. (3.4) (i.e., electron density and atomic ground state density) as well as all rate coefficients and reactions are known, Eq. (3.4) would yield the density (in QSS) of all states $p \geq 2$. The opposite, of course, is also true, that when the density of excited states is known (measured), the rates of the corresponding terms is known as

$$\underline{n} = \underline{A}^{-1} \cdot \left(n_e n_{H^+} \underline{R}_2 + n_e^2 n_{H^+} \underline{R}_3 + \underline{C} + n_e n_1 \underline{k}^{exc} \right) \quad (3.5)$$

The sum between parentheses on the right hand side of Eq. (3.5) is in fact the light produced by the plasma in steady state.

The aim of the present investigation is to determine the density of atoms in the ground state by perturbing the balance of Eq. (3.3) (or Eq. (3.4)) using the electron beam. It will be shown that the influence of the electron beam can be written as a superposition on the balance of Eq. (3.3). It is therefore not necessary to know all the details of the reactions taking place in the plasma without electron beam, since they can be accounted for collectively, using Eq. (3.5) and a measurement of the excited state densities. To determine the influence of the electron beam on the balance of Eq. (3.3) and thus on the excited state density it is only necessary to know the direct interaction of the electron beam with the particles present in the plasma.

3.3.2 Electron Beam in neutral hydrogen gas (plasma off, electron beam on)

When a beam of electrons with energy E_{beam} is incident on a neutral hydrogen gas with density $n_{H_2}^{gas}$, the electrons will excite and ionize the molecules. Part of the molecules will be excited into a dissociative state and will produce two neutral atoms:



These atoms can be in an excited state after ionization and can thus be detected by emission spectroscopy. Vroom and De Heer [19] have determined the cross sections for dissociative

excitation of H_2 by high-energy electrons for the states $p = 3$ through 6. These values are given in the appendix, for electron energies of 5 keV. For the excitation created by the beam of electrons a set of equations can be constructed similar to Eqs. (3.1) and (3.2)

$$\left(\underline{\underline{A}} + n_e^{beam} \underline{\underline{K}}^{exc,beam} + n_e^{beam} \underline{\underline{K}}^{ion,beam} \right) \cdot \underline{\underline{n}} = n_e^{beam} n_{H_2}^{gas} \underline{\underline{k}}_{diss}^{beam} \quad (3.7)$$

with n_e^{beam} the density of the electrons produced by the electron beam, and $\underline{\underline{k}}_{diss}^{beam}$ the vector containing the rates for dissociative excitation [19]. The rates for excitation and ionization by electrons depend on the energy of the incident electrons [18]. The matrices $\underline{\underline{K}}^{exc,beam}$ and $\underline{\underline{K}}^{ion,beam}$ are therefore different from the corresponding matrices in Eq. (3.2). In the set of equations given in Eq. (3.7) several terms have been neglected, compared to Eq. (3.2). The density of electrons produced by the electron beam is small compared to electrons in a plasma as will be shown in section 3.4, and their energy is high. Consequently, recombination reactions can be neglected entirely when compared to the dissociative excitation given on the right hand side of Eq. (3.3).

Once again, the ground state of the atoms, $p = 1$, is not in quasi steady state. The production of this state is by dissociation of molecules and by radiative decay of atoms in a higher excited state. The only destruction of ground state atoms is by excitation to higher states, or by ionization. The rate for these reactions is very low ($\approx 10^{-8} s^{-1}$ for $p = 1$, $n_e^{beam} = 10^{12} m^{-3}$), much lower than typical loss frequency by transport. The electron beam has a typical diameter of several centimeters, and the flow velocity of the gas is of the order of 400 m/s (see Chapter 4 of this thesis). This means that during the transit time of the gas through the electron beam, $10^{-4} s$, quasi steady state is not reached for ground state atoms. The ground state atoms that are produced by Eq. (3.6) can be excited into higher states and should therefore be (time dependent) included on the right hand side of Eq. (3.7). Although the rate coefficient for excitation of ground state atoms is somewhat higher than the dissociative excitation of the molecules, the contribution to the excited states is negligible, because the density of ground-state atoms will reach a density of the order $10^{14} m^{-3}$ ($n_e^{beam} = 10^{12} m^{-3}$, $n_{H_2}^{gas} = 10^{20} m^{-3}$, $k_{diss,1}^{beam} = 4 \times 10^{-15} m^3 s^{-1}$ [18]), much lower than the H_2 density. For excited states ($2 \leq p < 12$) the destruction is by radiative decay, with a rate of $10^7 - 10^4 s^{-1}$. Thus, quasi steady state is reached for these states. For the excited states $p < 12$, the collisional effects are negligible compared to the radiative decay. Furthermore, the production of these states by radiative decay or collisional de-excitation from higher states is negligible compared to the direct production by dissociative excitation of the molecules. In those cases, the production of the excited states by dissociative excitation is balanced by radiative decay, and Eq. (3.7) may be simplified to:

$$\underline{\underline{n}} = \underline{\underline{A}}^{-1} \cdot n_e^{beam} n_{H_2}^{gas} \underline{\underline{k}}_{diss}^{beam} \quad (3.8)$$

3.3.3 Electron Beam in a hydrogen plasma (plasma on, electron beam on)

If the beam of electrons is incident on the plasma, the resulting rate equation is a superposition of the effects of the plasma and the electron beam:

$$\begin{aligned} & \left(\underline{A} + n_e \underline{K}^{exc} + n_e \underline{K}^{ion} + n_e^{beam} \underline{K}^{exc,beam} + n_e^{beam} \underline{K}^{ion,beam} \right) \cdot \underline{n} \\ & = \left(n_e n_{H^+} \underline{R}_2 + n_e^2 n_{H^+} \underline{R}_3 + \underline{C} + n_e n_1 \underline{k}^{exc} + n_e^{beam} n_{H_2}^{plasma} \underline{k}_{diss}^{beam} + n_e^{beam} n_1 \underline{k}_{exc}^{beam} \right) \end{aligned} \quad (3.9)$$

with n_e the electron density of the plasma, n_e^{beam} the electron density of the electron beam (the high-energy electrons), and $n_{H_2}^{plasma}$ the density of the molecules when the plasma is turned on.

Mainly because the temperature of the gas during plasma operation is higher than when the plasma is turned off, $n_{H_2}^{plasma}$ will be significantly lower than $n_{H_2}^{gas}$ at the same pressure. The

last term of Eq. (3.9) represents the excitation of atomic hydrogen by the electron beam. Using the rate coefficients in the appendix and realistic estimates for the electron density ($n_e = 10^{17} \text{ m}^{-3}$, $n_e^{beam} = 10^{12} \text{ m}^{-3}$) it follows that the collisional terms on the left hand side of Eq. (3.8) may still be neglected, at least for the lower excited states ($p < 6$). The density of excited states in the plasma when the electron beam is on is thus a superposition of the density without the electron beam (Eq. (3.4)) and the density added by the electron beam (Eq. (3.8)) with the addition of the excitation of the ground state atoms by the electron beam. The excited state density in the plasma when the electron beam is on is thus given by

$$\underline{n} = \underline{A}^{-1} \cdot \left(n_e n_{H^+} \underline{R}_2 + n_e^2 n_{H^+} \underline{R}_3 + \underline{C} + n_e n_1 \underline{k}^{exc} + n_e^{beam} n_{H_2} \underline{k}_{diss}^{beam} + n_e^{beam} n_1 \underline{k}_{exc}^{beam} \right) \quad (3.10)$$

3.3.4 Determination of the dissociation degree by EBIF

To determine the degree of dissociation or the atom density in the plasma we will have to find n_1 explicitly from the set of equations given by Eqs. (3.5), (3.8) and (3.10). The excited state density found through each of these three equations represents a different situation (plasma on or off, electron beam on or off). In order to distinguish these cases we define the following excited state density distributions:

1. \underline{n}^{plasma} , given by Eq. (3.5), when only the plasma is on.
2. \underline{n}^{beam} , given by Eq. (3.8), when only the electron beam is on.
3. $\underline{n}^{plasma, beam}$, given by Eq. (3.10), when both plasma and electron beam are on.

If the density of an excited state is known in all three of the cases above, it can be shown that by combining Eqs. (3.5), (3.8) and (3.10), the density of the ground state n_1 in the plasma is given by

$$n_1 = n_{H_2}^{plasma} \left[\left(\frac{n_{H_2}^{gas}}{n_{H_2}^{plasma}} \right) \tau - 1 \right] \alpha_p \quad (3.11)$$

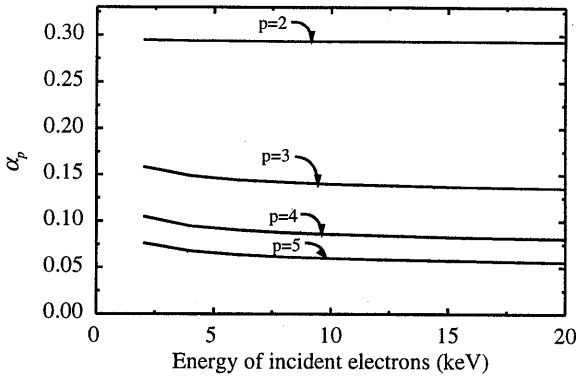


Figure 3.3: α_p (from Eq. (3.13)) as a function of electron energy for different excited states, p .

with

$$\tau = \frac{n_p^{plasma, beam} - n_p^{plasma}}{n_p^{beam}} \tag{3.12}$$

and

$$\alpha_p = \frac{[A^{-1} k_{diss}^{beam}]_p}{[A^{-1} k_{exc}^{beam}]_p} \tag{3.13}$$

The values for τ , $n_{H_2}^{gas}$ and $n_{H_2}^{plasma}$ must (and can) be determined from the experiments by absolute line intensity measurements. The values for α_p have been calculated (cf. appendix). α_p is a measure of how much more sensitive a certain state p is for excitation by the electrons from the atomic ground state compared to dissociative excitation of H_2 molecules. α_p is shown as a function of the energy of the beam electrons in Fig. 3.3. The values for states $p = 2$

Excited state p	α_p
2	0.2935
3	0.1443
4	0.0902
5	0.0636

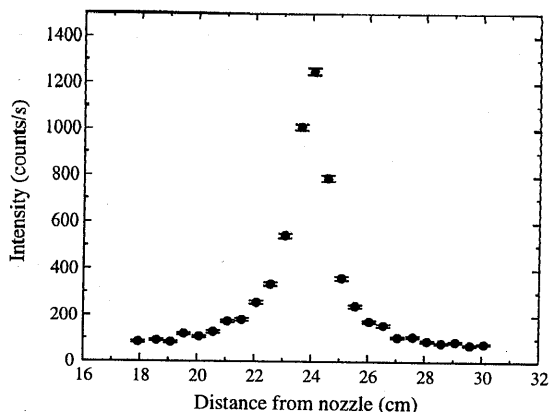


Figure 3.4: Intensity of the H- α signal from the electron beam as a function of horizontal position

to 5 are given in Table 3.1 for an electron energy of 5 keV. The value of α_p is always below 1. This means that all the excited states are more easily populated by excitation from the atomic ground state than by dissociative excitation of the molecules. A lower value of α_p means that the particular excited state is more sensitive to population by excitation from the atomic ground state.

3.4 Results

3.4.1 The electron beam

In the analysis of the electron beam and the eventual determination of the dissociation degree of the plasma the emission of the Balmer- α line at 656.3 nm is detected. This line represents the transition from $p = 3$ to $p = 2$. This transition is chosen because it has the highest intensity when the plasma or the hydrogen gas is illuminated by the electron beam. As will be discussed later, the intensity mostly determines the accuracy of the measurements in the current setup, so that a higher intensity improves the accuracy. Furthermore, the influence of the collisional excitation and de-excitation terms of Eqs. (3.3), (3.7) and (3.9) is smallest for the lowest excited levels and may be neglected with the least loss of accuracy. Since determination of the density of $p = 2$ by emission is not possible (the transition $2 \rightarrow 1$ is in the far UV range and the transition will be optically thick in the plasma under investigation), $p = 3$ is the lowest level that can be measured with the current setup.

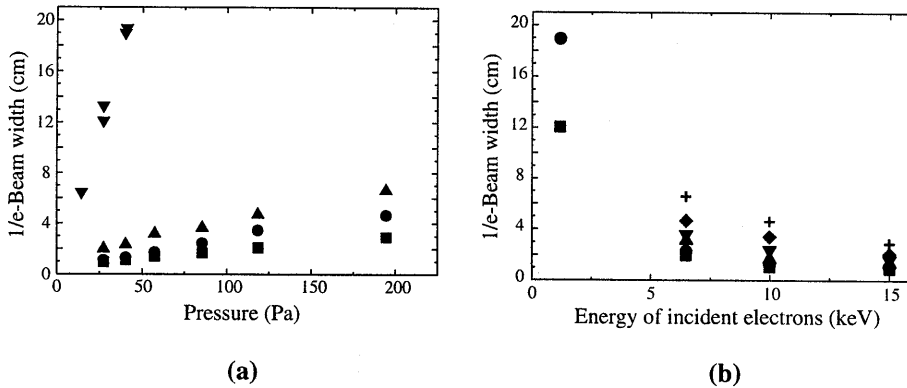


Figure 3.5: (a) Electron beam width as a function of background pressure for different electron energies, ∇ 1.3 keV, \blacktriangle 6.5 keV, \bullet 10 keV, and \blacksquare 16 keV. (b) Beam width as a function of electron energy at different settings of the background pressure, \blacksquare 27 Pa, \bullet 40 Pa, \blacktriangle 57 Pa, ∇ 85 Pa, \blacklozenge 118 Pa, and $+$ 194 Pa.

A horizontal scan of the H- α line across the electron beam is shown in Fig. 3.4 with the plasma turned off. The hydrogen flow was set to 3 standard liters per minute (slm), the background pressure was 20.7 Pa, and the electron beam energy 5 keV. The integration time of the measurement is 5 s. Since the plasma is turned off, the intensity (which is proportional to the density of the excited state) is proportional to the gas density and the electron density, according to Eq. (3.8). Because the electron beam is much larger than the focal width of the optical emission spectroscopy, the intensity of the H- α as measured in Fig. 3.4 is integrated over the width of the beam. Figure 3.4 thus shows the projection of the electron density of the electron beam.

When the pressure is increased, the electrons from the electron beam will be scattered by the gas particles. The width of the beam will increase and the electron density will decrease. The beam width has been defined here as the 1/e width of a Gaussian fitted to the horizontal scans. The result is shown in Fig. 3.5(a) where the width of beam is shown as a function of pressure. When the energy of the beam electrons is increased, the cross section for scattering of the electrons decreases. This is shown in Fig. 3.5(b) where the beam width is shown as a function of electron energy.*

The electron density in the electron beam can be determined in two different ways:

* The intensity of the measured signal is the product of electron density and excitation cross section. Decreasing the electron energy increases the cross section, but also increases the beam width thereby lowering the electron density. The optimum choice of electron energy depends on the background pressure. As a rule of thumb, the highest intensity is obtained when the electron energy is chosen so that the mean free path of the electrons is of the order of the dimensions of the vessel. In that case there is no significant scattering of the beam, but most electrons will still cause 1-10 excitations.

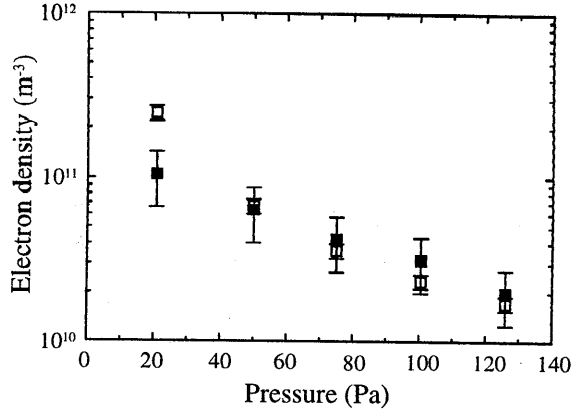


Figure 3.6: Electron density at the center of the electron beam with electron energy of 6 keV. ■ using current measurement (method 1), and □ using absolute calibration (method 2)

1. by measuring the current on the detector on the opposite side of the vessel from the electron gun and the beam width
2. by measuring the absolute density of the state $p = 3$ and using Eq. (3.7).

Method 1: current measurement.

The spatial electron density distribution may be approximated by a Gaussian

$$n_e^{beam}(r) = n_{e0}^{beam} e^{-\frac{r^2}{\left(\frac{1}{2}bw\right)^2}} \quad (3.14)$$

with n_e^{beam} the electron density, n_{e0}^{beam} the electron density at the center of the beam, r the distance to the center of the beam, and bw the $1/e$ beam width. The current on the detector, I_{det} , is then given by

$$I_{det} = n_{e0}^{beam} \frac{1}{4} \sqrt{\frac{E_{beam}}{2m_e}} \pi (bw)^2 \quad (3.15)$$

with E_{beam} the energy of the beam electrons, and m_e the electron mass. The energy of the electrons, E_{beam} , is set and the current on the detector, I_{det} , and the beam width, bw , are measured. The electron density found using this method is shown as solid squares in Fig. 3.6.

Method 2: absolute density measurement

The optical emission spectroscopy setup has been calibrated using a tungsten ribbon lamp to obtain absolute emissivities [20, 21]. The number of photons counted by the spectroscopy setup, F_{det} , corresponding to a transition $p \rightarrow q$ is given by

$$F_{det} = \frac{1}{4\pi} A_{pq} \Delta\Omega \cdot d \cdot h_s \cdot \eta \cdot \int n_p(s) ds \quad (3.16)$$

with A_{pq} the transition probability, $\Delta\Omega$ the solid angle covered by the detector, d the slit width of the monochromator, h_s the slit height of the monochromator, η the efficiency of the setup, and s the coordinate along the line of sight. The product $\Delta\Omega \cdot d \cdot h_s \cdot \eta$ has been determined from the calibration with the tungsten ribbon lamp. In the case the plasma is switched off the density of the excited states is given by Eq. (3.7). The density of the hydrogen molecules, $n_{H_2}^{gas}$, is constant and given by the ideal gas law

$$n_{H_2}^{gas} = \frac{p_{vessel}}{k_B T_{gas}} \quad (3.17)$$

with p_{vessel} the background pressure in the vessel, k_B Boltzmann's constant, and T_{gas} the gas temperature. The latter is approximately 300 K when the plasma is not turned on. If the spatial electron density distribution is assumed to be approximately Gaussian, following Eq. (3.14), the electron density at the center of the electron beam, n_{e0}^{beam} , is found from Eqs. (3.7), (3.14), (3.16), and (3.17)

$$n_{e0}^{beam} = \frac{1}{k_{diss p}} \frac{k_B T_{gas}}{p_{vessel}} \frac{F_{det} 4\pi}{\Delta\Omega \cdot d \cdot h_s \cdot \eta} \frac{1}{\sqrt{\pi} \frac{1}{2} bw \sqrt{2}} \quad (3.18)$$

with $k_{diss p}$ the rate coefficient for dissociative excitation of the hydrogen molecule into excited state p . The factor $\sqrt{2}$ is a result of the fact that the electron beam is at an angle of 45° with the line of sight of the spectroscopy setup. The electron density determined using Eq. (3.18) and the density of the $p = 3$ state is shown as open squares in Fig. 3.6.

In both methods 1 and 2 it is assumed that the energy of the beam electrons does not change significantly due to scattering or excitation of the molecules. Because of the large difference in mass between the electrons and the molecules, the momentum loss for the electrons will be minimal, so that this is a reasonable assumption. It is not necessary to know the electron density exactly in order to determine the dissociation degree (Eq. (3.11)). The electron density of the beam is only needed to establish whether the density of the molecules and the ground state atoms (that were assumed to be constant in the derivation of Eq. (3.11)) is changed significantly. For that purpose, the agreement between both methods is satisfactory.

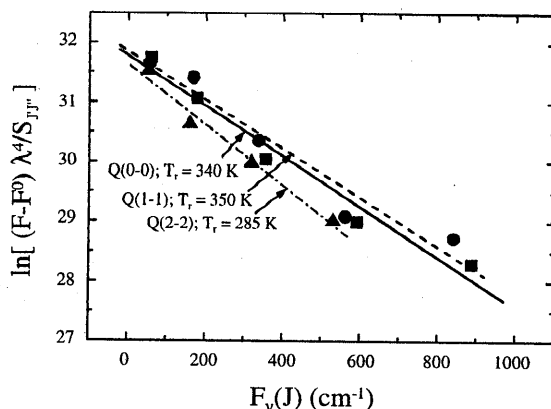


Figure 3.7: Boltzmann plot of the Q -branches in the (0-0), (1-1), and (2-2) band. Measurements are taken at 6 cm from the nozzle, $p_{\text{vessel}} = 20$ Pa, $I_{\text{arc}} = 50$ A, and hydrogen flow of 2 slm. From these measurements the gas temperature is determined to be 500 ± 70 K.

The electron density in the electron beam does not exceed 10^{12} m^{-3} . Thus the electron beam does not significantly influence the densities of the molecules and ground state atoms. It also means that the superposition of Eqs. (3.5) and (3.8) leading to Eq. (3.10) is justified.

3.4.2 The density of the molecules

To determine the dissociation degree from Eq. (3.11) it is necessary to know the ratio $\frac{n_{\text{H}_2}^{\text{gas}}}{n_{\text{H}_2}^{\text{plasma}}}$.

This ratio can be determined in two different ways:

1. by determination of the gas temperature, using the rotational spectrum of excited H_2 .
2. by addition of a small amount of helium as a tracer gas and measurements of $\text{He}(3p)$ excited by the electron beam

Method 1: determination of the rotational temperature

Close to the nozzle ($z = 6$ cm) and at relatively low pressure ($p_{\text{vessel}} < 35$ Pa), the Fulcher- α spectrum of hydrogen is visible. This spectrum is caused by the electronic transition $\text{H}_2(d^3\Pi_u) \rightarrow \text{H}_2(a^3\Sigma_g^+)$. The structure of the rovibrational spectrum can be analyzed to obtain the rotational temperature. This rotational temperature can be translated to a gas temperature by taking into account the Frank-Condon factors of the ground state $\text{H}_2(X^1\Sigma_g^+)$ and the excited $\text{H}_2(d^3\Pi_u)$ (see for example [5]). An example of the determination of the gas temperature from a Boltzmann plot of the rotational spectrum is shown in Fig. 3.7.

The dissociation degree in the plasma, β (with $\beta = n_1 / (n_{H_2}^{plasma} + n_1)$) is found after rearranging Eq. (3.11) (the background pressure is kept constant, whether plasma is on or off):

$$\beta = \left(\frac{T_{plasma}}{T_{gas}} \tau - 1 \right) \frac{\alpha_p}{1 - \alpha_p} \quad (3.19)$$

with T_{plasma} the temperature when the plasma is switched on. The temperature of the gas when the plasma is off, T_{gas} , is room temperature, approximately 300 K.

An uncertainty in this determination of the gas temperature is the origin of excited molecules. The translation of the rotational temperature of $H_2(d^3\Pi_u)$ to gas temperature is only allowed if $H_2(d^3\Pi_u)$ is excited directly from the ground state by electron impact. In the downstream plasma, part of the excited molecules may be formed by recombination of molecular ions, H_3^+ . This could introduce an error in the determination of the gas temperature [22]. In the present investigation, the Fulcher- α spectrum is only visible in the supersonic part, close to the nozzle. The electron density here is still sufficiently high to excite the molecules directly from the ground state. Also, the dissociative recombination of H_2^+ (the precursor to H_3^+) is fast due to the high electron density. Therefore, close to the nozzle, the determination of the temperature of the plasma from the Fulcher- α spectrum is a valid method.

Method 2:

Another method to monitor the total gas density is the addition of a small amount of helium in the vessel. Helium is excited by the electron beam in the same way hydrogen is. The excited states of He are populated by electron impact excitation of ground state He and depopulated by radiative decay (a true corona balance [15]). The density of excited He, \underline{n}_{He} , is therefore proportional to the He density, n_{He} , similar to Eq. (3.8):

$$\underline{n}_{He} = \underline{A}_{He}^{-1} \cdot n_e^{beam} n_{He} \underline{k}_{He,exc}^{beam} \quad (3.20)$$

with \underline{A}_{He}^{-1} the matrix of transition probabilities, and $\underline{k}_{He,exc}^{beam}$ the vector containing the rate coefficients for excitation of ground state helium to an excited state by the electron beam.

To monitor the gas density a small flow of helium is injected from the top of the vessel. The density of excited He(3p) is determined by measuring the $3p \rightarrow 2s$ transition at 501.568 nm (this is the line with the highest intensity in the visible He spectrum). The density of this state is measured with the plasma switched off and with the plasma switched on. The partial flow of helium is kept constant so that the partial pressure in the vessel is also constant. The measured intensity of the transition is then proportional to the total gas density. The dissociation degree of hydrogen is now found as

$$\beta = \left(\frac{I_{He(3p)}^{gas}}{I_{He(3p)}^{plasma}} \tau - 1 \right) \frac{\alpha_p}{1 - \alpha_p} \quad (3.21)$$

with $I_{He(3p)}^{gas}/I_{He(3p)}^{plasma}$ the ratio of the intensity of the He(3p) signal with the plasma switched off to the intensity with the plasma switched on.

The two methods to account for the difference in temperature (and density) can be used in different regions of the plasma. Method 1 (the rotational temperature from the Fulcher- α) is most accurate close to the nozzle, in the supersonic part. Further downstream, the intensity of the Fulcher- α spectrum is too low to determine the temperature accurately. The second method (using helium as a tracer gas) is least accurate in the supersonic part, because mixing between the background helium and the plasma will not be complete. In the subsonic part, on the other hand, the second method is most accurate.

3.4.3 The dissociation degree

To determine the dissociation degree in the downstream hydrogen plasma (only) the intensity of the Balmer α transition ($p = 3 \rightarrow 2$) was measured. The depopulation of the $p = 3$ state occurs only through radiative decay and is not significantly affected by collisional (de-)excitation. For this transition Eqs. (3.5), (3.8) and (3.10) may be used. The variable τ (Eq. (3.12)) is determined from the three measurements shown in Fig. 3.8(a). The ratio $I_{He(3p)}^{gas}/I_{He(3p)}^{plasma}$ is determined from the measurements of Fig. 3.8(b). The intensity of the helium signal in the case the electron beam is turned off is equal to the dark current of the spectroscopy setup. This shows that (as expected) there is no excitation of He by the plasma. The settings of the plasma and the electron beam for the measurements of Fig. 3.8 are given in Table 3.2.

The dissociation degree determined for these settings is shown in Fig. 3.9. The most accurate measurements are the ones around 24.5 cm, at the center of the electron beam, where the density of the beam electrons is highest. For the plasma settings of Table 3.2, the dissociation degree at 24.5 cm downstream from the nozzle is $5 \pm 1\%$. The hydrogen atom density, n_1 , is $(4.6 \pm 1.3) \times 10^{20} \text{ m}^{-3}$. This result is in agreement with the active actinometry measurements of De Graaf [5]. It is consistent with substantial dissociation inside the arc source (up to 100%).

Hydrogen flow	3	slm
Arc current	40	A
Background pressure	49.2	Pa
Helium flow	0.1	slm
Beam energy	5	keV

The hydrogen atoms coming from the source diffuse towards the vessel walls in the downstream plasma where they associate with high probability (between 0.1 and 1) to form hydrogen molecules. The downstream plasma is diluted by these molecules, effectively reducing the dissociation degree to the 5% found.

In this investigation only one example is given of how to determine the dissociation degree in the downstream hydrogen plasma. To investigate the kinetics of hydrogen atoms in more detail more measurements are necessary.

The largest uncertainty in the present measurements is caused by the inaccuracies of the optical emission spectroscopy setup. To determine the dissociation degree, the signal from the plasma without the electron beam has to be subtracted from the signal of the plasma with the electron beam. This substantially increases the uncertainties. Improvements in the accuracy can be achieved if a pulsed electron beam is used in combination with a lock in amplifier to select only the signal induced by the electron beam. In addition a higher electron current from the electron beam will increase the intensity of the detected signals and improve accuracy. With a higher electron current it is also possible to determine the excited state densities of higher excited states ($p \geq 4$) with sufficient accuracy. These states are disturbed less by the dissociative excitation of hydrogen molecules so that the dissociation degree can be determined with greater accuracy.

The method of EBIF for the detection of atoms and other radicals can in principle be extended to include plasmas other than hydrogen. However, most plasmas contain elements which have much larger cross sections for scattering of electrons. For measurements in such plasmas it is necessary to increase the energy of the beam electrons in order to reduce the scattering. An improved electron gun is necessary to achieve this.

All of the limitations of the accuracy and applicability of the current setup are technical. This means that significant improvements can be achieved by some relatively straightforward adjustments to the electron gun assembly.

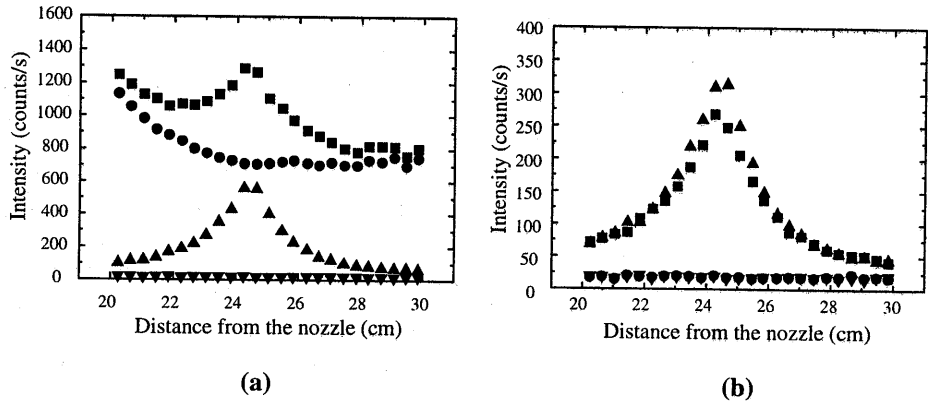


Figure 3.8: (a) intensity of the H- α line at 656.27 nm, with \blacksquare plasma on and e-beam on, \bullet plasma on and e-beam off, \blacktriangle plasma off and electron beam on, and \blacktriangledown plasma off and electron beam off. (b) intensity of the He- α line at 501.568 nm, symbols indicate the same settings as in (a)

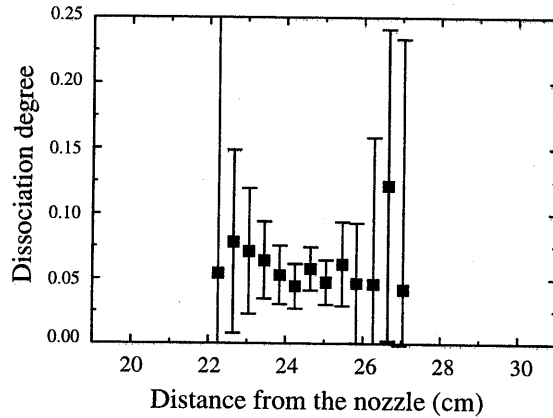


Figure 3.9: The dissociation degree as determined from the measurements of Fig. 3.8.

3.5 Conclusions

A new method to determine the dissociation degree in a downstream hydrogen plasma was investigated. It was demonstrated how electron beam induced fluorescence can be applied to measure the dissociation degree. The lower excited states of hydrogen ($p = 3-6$) are populated by dissociative excitation of hydrogen molecules and excitation of ground state atoms, and depopulated by radiative decay. This leads to a first order relation between the fluorescent excited state density and the dissociation degree of the plasma. The total gas density can be determined from either the rotational Fulcher- α spectrum or by measuring the fluorescence signal of a small amount of added helium. As an example the dissociation degree in a hydrogen plasma with a hydrogen flow of 3 slm, 40 A arc current and 49.2 Pa background pressure was determined. The dissociation degree was found to be $5 \pm 1\%$. The hydrogen atom density was $(4.6 \pm 1.3) \times 10^{20} \text{ m}^{-3}$. This density is consistent with earlier results using active actinometry [5].

An advantage of EBIF is that it is used in a crossed beam experiment, enabling local measurements. In contrast with TALIF, there is no need for absolute calibration of the measurements when using EBIF. A disadvantage of the current setup is that it can only be used in a hydrogen plasma with sufficiently high dissociation degree ($> 1\%$). The accuracy of the setup used is limited by the current and energy of electrons from the electron gun. Some technical alterations can significantly improve the accuracy and applicability of the EBIF.

The theory used in the determination of hydrogen atoms from EBIF can be extended in a straightforward manner for use in plasmas containing other radicals, such as nitrogen and oxygen atoms. With some changes to the electron gun assembly it will also be possible to determine radical densities in more complex plasmas containing silane, methane, etc.

References

- 1 M.C.M. van de Sanden, R.J. Severens, R.F.G. Meulenbroeks, M.J. de Graaf, Z. Qing, D.K. Otorbaev, R. Engeln, J.W.A.M. Gielen, J.A.M. van der Mullen, and D.C. Schram, *Surf. Coatings Technol.* **74-75**, 1 (1995)
- 2 E.S. Cielaszyk, K.H.R. Kirmse, R.A. Stewart, and A.E. Wendt, *Appl. Phys. Lett.* **67**, 3099 (1995).
- 3 J.S. Montgomery, T.P. Schneider, R.J. Carter, J.P. Barnak, Y.L. Chen, J.R. Hauser, and R.J. Nemanich, *Appl. Phys. Lett.*, **67** 2194 (1995).
- 4 D.K. Otorbaev, A.J.M. Buuron, N.T. Guerassimov, M.C.M. van de Sanden, and D.C. Schram, *J. Appl. Phys.* **76**, 1 (1994).
- 5 M.J. de Graaf, PhD thesis, Eindhoven University of Technology (1994).
- 6 D. Wagner, B. Dikmen, and H.F. Döbele, *Plasma Sources Sci. Technol.* **7**, 462 (1998).

- 7 U. Czarnetski, K. Miyazaki, T. Kajiwara, K. Muraoka, M. Marda, H.F. Döbele, *J. Opt. Soc. Am. B* **11**, 2155 (1994).
- 8 J. Amorim, G. Baravian, M. Touzeau, and J. Jolly, *J. Appl. Phys.* **76**, 1487 (1994).
- 9 D.W. Setser, *Reactive Intermediates in the Gas Phase*, Academic Press, New York (1979).
- 10 E.P. Muntz, *Phys. Fluids*, **5**, 80 (1962).
- 11 E.P. Muntz, *The Electron Beam Fluorescence Technique*, AGARDograph 132 (1968).
- 12 R.P. Thorman, and S.L. Bernasek, *J.Chem. Phys.* **74**, 6498 (1981).
- 13 R.P. Thorman, D. Anderson, and S.L. Bernasek, *Phys. Rev. Lett.* **44**, 743 (1980).
- 14 M.C.M. van de Sanden, J.M. de Regt, and D.C. Schram, *Plasma Sources Sci. Technol.* **3**, 501 (1994).
- 15 D.R. Bates, A.E. Kingston, R.W.P. McWhirter, *Proc. Roy. Soc.* **267**, 297 (1962).
- 16 J.A.M. van der Mullen, *Phys. Rep.* **191**, 109 (1990).
- 17 W.L. Wiese, M.W. Smith, and B.M. Glennon, *Atomic Transition Probabilities - Volume I: Hydrogen through Neon*, U.S. Government Printing office (1966).
- 18 R.K. Janev, W.D. Langer, K. Evans Jr., and D.E. Post Jr., *Elementary Processes in Hydrogen-Helium Plasmas*, Springer-Verlag, Berlin (1987).
- 19 D.A. Vroom, and F.J. de Heer, *J. Chem. Phys.* **50**, 580 (1966).
- 20 J. Voogd, *Philips Techn. Tijdschr.* **5**, 87 (1940).
- 21 J.C. de Vos, *Physica* **20**, 690 (1954).
- 22 Zhou Qing, PhD thesis, Eindhoven University of Technology (1995).

Appendix to Chapter 3

Definitions

The vectors and matrices used in the collisional radiative modelling of chapter 3 are defined as follows:

The density of excited states

$$\underline{n} = \begin{pmatrix} n_2 \\ n_3 \\ n_4 \\ \vdots \end{pmatrix} \quad (\text{A } 1)$$

The transition probability matrix for radiative decay:

$$\underline{A} = \begin{pmatrix} -A_{21} & A_{32} & A_{42} & \cdots \\ 0 & -\sum_{i=1}^2 A_{3i} & A_{43} & \cdots \\ 0 & 0 & -\sum_{i=1}^3 A_{4i} & \cdots \\ \vdots & \vdots & \vdots & \ddots \end{pmatrix} \quad (\text{A } 2)$$

The matrix for collisional excitation and de-excitation

$$\underline{K}^{exc} = \begin{pmatrix} -\sum_{j=3}^{\infty} k_{2j} - k_{21} & k_{32} & k_{42} & \cdots \\ k_{23} & -\sum_{j=4}^{\infty} k_{3j} - \sum_{l=2}^1 k_{3l} & k_{43} & \cdots \\ k_{24} & k_{34} & -\sum_{j=5}^{\infty} k_{4j} - \sum_{l=3}^1 k_{4l} & \cdots \\ \vdots & \vdots & \vdots & \ddots \end{pmatrix} \quad (\text{A } 3)$$

and the vector for excitation from the ground state

$$\underline{k}^{exc} = \begin{pmatrix} k_{12} \\ k_{13} \\ k_{14} \\ \vdots \end{pmatrix} \quad (\text{A } 4)$$

Collisional ionization:

$$\underline{\underline{K}}^{ion} = \begin{pmatrix} k_{2+} & 0 & 0 & \dots \\ 0 & k_{3+} & 0 & \dots \\ 0 & 0 & k_{4+} & \dots \\ \vdots & \vdots & \vdots & \ddots \end{pmatrix} \quad (\text{A } 5)$$

Numerical values for 0.2 eV electron temperature and 5 keV beam energy.

The numerical values for the matrices that are used:

$$\underline{\underline{A}} = \begin{bmatrix} -4.6990 & 0.4410 & 0.0842 & 0.0253 & 0.0097 & 0.0044 & 0.0022 & 0.0012 & 0.0007 & \dots \\ 0 & -0.9986 & 0.0899 & 0.0220 & 0.0078 & 0.0034 & 0.0017 & 0.0009 & 0.0005 & \dots \\ 0 & 0 & -0.3019 & 0.0270 & 0.0077 & 0.0030 & 0.0014 & 0.0007 & 0.0004 & \dots \\ 0 & 0 & 0 & -0.1155 & 0.0102 & 0.0033 & 0.0014 & 0.0007 & 0.0004 & \dots \\ 0 & 0 & 0 & 0 & -0.0519 & 0.0046 & 0.0016 & 0.0007 & 0.0004 & \dots \\ 0 & 0 & 0 & 0 & 0 & -0.0262 & 0.0023 & 0.0008 & 0.0004 & \dots \\ 0 & 0 & 0 & 0 & 0 & 0 & -0.0144 & 0.0012 & 0.0005 & \dots \\ 0 & 0 & 0 & 0 & 0 & 0 & 0 & -0.0085 & 0.0007 & \dots \\ 0 & 0 & 0 & 0 & 0 & 0 & 0 & 0 & -0.0052 & \dots \\ \vdots & \vdots & \vdots & \vdots & \vdots & \vdots & \vdots & \vdots & \vdots & \ddots \end{bmatrix} \times 10^8 \text{ s}^{-1}$$

Collisional (de)excitation and ionization in the plasma:

$$\underline{\underline{K}}^{exc} = \begin{bmatrix} -0.0006 & 0.0029 & 0.0090 & 0.0220 & 0.0456 & 0.0845 & 0.1441 & 0.2309 & 0.3519 & \dots \\ 0 & -0.0058 & 0.0090 & 0.0220 & 0.0456 & 0.0845 & 0.1441 & 0.2309 & 0.3519 & \dots \\ 0 & 0 & -0.2700 & 0.0220 & 0.0456 & 0.0845 & 0.1441 & 0.2309 & 0.3519 & \dots \\ 0 & 0 & 0 & -0.1195 & 0.0456 & 0.0845 & 0.1441 & 0.2309 & 0.3519 & \dots \\ 0 & 0 & 0 & 0.0315 & -0.3139 & 0.0845 & 0.1441 & 0.2309 & 0.3519 & \dots \\ 0 & 0 & 0 & 0 & 0.0715 & -0.6800 & 0.1441 & 0.2309 & 0.3519 & \dots \\ 0 & 0 & 0 & 0 & 0.0144 & 0.1430 & -1.3256 & 0.2309 & 0.3519 & \dots \\ 0 & 0 & 0 & 0 & 0 & 0.0300 & 0.2604 & -2.2829 & 0.3519 & \dots \\ 0 & 0 & 0 & 0 & 0 & 0.0121 & 0.0564 & 0.4389 & -3.1671 & \dots \\ \vdots & \vdots & \vdots & \vdots & \vdots & \vdots & \vdots & \vdots & \vdots & \ddots \end{bmatrix} \times 3 \cdot 10^{-10} \text{ m}^3 \text{ s}^{-1}$$

$$\underline{\underline{K}}^{ion} = \begin{bmatrix} 0 & 0 & 0 & 0 & 0 & 0 & 0 & 0 & \dots \\ 0 & 0 & 0 & 0 & 0 & 0 & 0 & 0 & \dots \\ 0 & 0 & 0 & 0 & 0 & 0 & 0 & 0 & \dots \\ 0 & 0 & 0 & 0 & 0 & 0 & 0 & 0 & \dots \\ 0 & 0 & 0 & 0 & 0 & 0 & 0 & 0 & \dots \\ 0 & 0 & 0 & 0 & 0 & 0 & 0 & 0 & \dots \\ 0 & 0 & 0 & 0 & 0 & 0 & 0 & 0 & \dots \\ 0 & 0 & 0 & 0 & 0 & 0 & 0 & 0 & \dots \\ 0 & 0 & 0 & 0 & 0 & 0.1858 & 0 & 0 & \dots \\ 0 & 0 & 0 & 0 & 0 & 0 & 0.5058 & 0 & \dots \\ \vdots & \vdots & \vdots & \vdots & \vdots & \vdots & \vdots & \vdots & \ddots \end{bmatrix} \times 0.3 \cdot 10^{-10} \text{ m}^3 \text{ s}^{-1}$$

Collisional (de)excitation and ionization by the electron beam:

$$\underline{\underline{K}}^{exc,beam} = \begin{bmatrix} -0.0047 & 0.0000 & 0.0000 & 0.0000 & 0.0000 & 0.0000 & 0.0000 & 0.0000 & 0.0000 & \dots \\ 0.0037 & -0.0192 & 0.0000 & 0.0000 & 0.0000 & 0.0000 & 0.0000 & 0.0000 & 0.0000 & \dots \\ 0.0006 & 0.0155 & -0.0535 & 0.0000 & 0.0000 & 0.0000 & 0.0000 & 0.0000 & 0.0000 & \dots \\ 0.0002 & 0.0022 & 0.0441 & -0.1204 & 0.0000 & 0.0000 & 0.0000 & 0.0000 & 0.0000 & \dots \\ 0.0001 & 0.0007 & 0.0058 & 0.1010 & -0.2355 & 0.0000 & 0.0000 & 0.0000 & 0.0000 & \dots \\ 0.0001 & 0.0004 & 0.0019 & 0.0125 & 0.2009 & -0.4155 & 0.0000 & 0.0000 & 0.0000 & \dots \\ 0.0000 & 0.0002 & 0.0009 & 0.0040 & 0.0237 & 0.3616 & -0.6711 & 0.0000 & 0.0000 & \dots \\ 0.0000 & 0.0001 & 0.0005 & 0.0019 & 0.0075 & 0.0411 & 0.6044 & -0.9538 & 0.0000 & \dots \\ 0.0000 & 0.0001 & 0.0003 & 0.0011 & 0.0034 & 0.0127 & 0.0666 & 0.9538 & -1.438 & \dots \\ \vdots & \vdots & \vdots & \vdots & \vdots & \vdots & \vdots & \vdots & \vdots & \ddots \end{bmatrix} \times 0.4 \cdot 10^{-10} \text{ m}^3 \text{ s}^{-1}$$

$$\underline{\underline{K}}^{ion,beam} = \begin{bmatrix} 0.0018 & 0 & 0 & 0 & 0 & 0 & 0 & 0 & 0 & \dots \\ 0 & 0.0143 & 0 & 0 & 0 & 0 & 0 & 0 & 0 & \dots \\ 0 & 0 & 0.0255 & 0 & 0 & 0 & 0 & 0 & 0 & \dots \\ 0 & 0 & 0 & 0.0399 & 0 & 0 & 0 & 0 & 0 & \dots \\ 0 & 0 & 0 & 0 & 0.0574 & 0 & 0 & 0 & 0 & \dots \\ 0 & 0 & 0 & 0 & 0 & 0.0782 & 0 & 0 & 0 & \dots \\ 0 & 0 & 0 & 0 & 0 & 0 & 0.1021 & 0 & 0 & \dots \\ 0 & 0 & 0 & 0 & 0 & 0 & 0 & 0.1292 & 0 & \dots \\ 0 & 0 & 0 & 0 & 0 & 0 & 0 & 0 & 0.1595 & \dots \\ \vdots & \vdots & \vdots & \vdots & \vdots & \vdots & \vdots & \vdots & \vdots & \ddots \end{bmatrix} \times 0.04 \cdot 10^{-10} \text{ m}^3 \text{ s}^{-1}$$

Excitation from the ground state:

$$\underline{\underline{k}}_{exc}^{beam} = \begin{pmatrix} 0.3395 \\ 0.0590 \\ 0.0208 \\ 0.0098 \\ 0.0054 \\ 0.0033 \\ 0.0022 \\ 0.0015 \\ 0.0011 \\ \vdots \end{pmatrix} \times 4 \cdot 10^{-14} \text{ m}^3 \text{ s}^{-1}$$

Dissociative excitation of molecules:

$$\underline{\underline{k}}_{exc}^{beam} = \begin{pmatrix} 0.1071 \\ 0.0095 \\ 0.0021 \\ 0.0007 \\ 0.0003 \\ 0.0001 \\ 0.0001 \\ 0.0000 \\ 0.0000 \\ \vdots \end{pmatrix} \times 4 \cdot 10^{-14} \text{ m}^3 \text{ s}^{-1}$$

4 Drift Velocity and Diffusion in the downstream argon plasma

4.1 Introduction

The expanding or remote arc generated plasma is used for surface engineering such as deposition of thin layers [1, 2], etching [3, 4] or treatment of bulk material [5]. The composition of the plasma and the resulting fluxes of particles from the plasma to the surface are important for the processes taking place. This composition can be influenced by different settings of parameters of the arc and the low pressure vessel. Inside the arc the plasma can be changed by the choice of gas mixtures or the current through the arc. After the expansion into the low pressure vessel the different species in the plasma continue to react in the gas phase or after reaching the vessel wall with species ad- or absorbed there. The time the species in the plasma have to react with each other and with background gases recirculating in the vessel [6] is determined by the flow velocity and diffusion processes. To understand and describe the kinetic processes in the plasma it is therefore of great importance to know the transport of the particles, i.e. drift velocity and diffusion in the vessel.

One way to measure the velocity is to use Laser Induced Fluorescence [7, 8]. In the experiments described here we use resonant LIF on the 4s-4p transition in argon. The experimental setup is shown in Fig. 4.1. In this setup the tunable diode laser is shining in the direction exactly opposite to the flow direction of the expanding plasma. Due to the Doppler effect, the particles travelling towards the laser will absorb the laser light at a slightly lower frequency than particles at rest. The absorbed light is re-emitted and detected at an angle of 90° to the flow. From the difference in frequency between the absorbed and fluorescent light the drift velocity is determined. The spread in the measured frequency is a measure for the temperature of the absorbing particles. From the temperature the diffusion coefficient can be determined.

In section 4.2, describing the theory of diffusion and drift, the analytical solution for freely diffusing particles in a gas flow at constant velocity will be presented. The axial and radial profiles of the ions emanated from the arc will be compared to these solutions in the section on experimental results. From the experimental results the conditions leading to the theoretical solution will be reviewed and adjusted to properly fit the data.

4.2 Theory

In this section we consider the behavior of ions emanated from the arc into the low pressure vessel. First the particles will be accelerated and the drift velocity becomes supersonic. At a certain point in the vessel, depending on vessel pressure and arc conditions a stationary shock front of the barrel shock will occur, after which the particles will drift in the positive z -direction at subsonic speed. The expansion and shock in argon plasmas have been treated extensively by Van de Sanden [9, 10]. In this section we will consider the behavior of the particles after the shock where they drift at subsonic speed.

The density of the ions, n_i , in steady state is determined by the continuity equation

$$\frac{dn_i}{dt} = -\bar{\nabla} \cdot (n_i \bar{v}_d) + \bar{\nabla} \cdot (D_a \bar{\nabla} n_i) + P - n_i R = 0 \quad (4.1)$$

with \bar{v}_d the drift velocity (vector), D_a the ambipolar diffusion coefficient, P volume production, and R recombination of the ions. In the case of the downstream argon plasma under investigation volume production and recombination can be neglected (this assumption will be discussed in section 4.4 on the basis of the experimental results obtained).

In order to be able to find an analytical solution of Eq. (4.1) that will give some insight in the behavior of the particles Eq. (4.1) is simplified further:

- Cylindrical symmetry is assumed (the position of the pumping unit may disturb the symmetry somewhat).
- The drift velocity is taken to be constant and the radial component of the drift velocity is assumed to be negligible compared to radial diffusion.
- Diffusion in the axial (z) direction is negligible compared to the contribution of drift, so that diffusion only takes place in the radial direction.
- The temperature is assumed to be constant, so that the diffusion coefficient D_+ is constant.

With these simplifications, the continuity equation can be written in cylindrical coordinates as

$$-v_d \frac{\partial n_i(z,r)}{\partial z} + D_a \frac{1}{r} \left(\frac{\partial}{\partial r} \left(r \frac{\partial n_i(z,r)}{\partial r} \right) \right) = 0 \quad (4.2)$$

which has a solution of the form

$$n_i(z,r) = n_i(z,0) \cdot e^{-\frac{r^2}{(\rho(z))^2}} \quad (4.3)$$

with $\rho(z)$ the radius of the distribution at position z . Substituting Eq. (4.3) into the differential equation Eq. (4.2) leads to

$$-v_d \cdot e^{-\frac{r^2}{(\rho(z))^2}} \left(\frac{\partial n_i(z,0)}{\partial z} + n_i(z,0) \frac{2r^2}{(\rho(z))^3} \frac{\partial \rho(z)}{\partial z} \right) + \frac{4D_a}{(\rho(z))^2} n_i(z,r) \cdot e^{-\frac{r^2}{(\rho(z))^2}} \left(\frac{r^2}{(\rho(z))^2} - 1 \right) = 0 \quad (4.4)$$

This relation must hold for all r , which means that

$$-v_d \frac{2r^2}{(\rho(z))^3} \frac{\partial \rho(z)}{\partial z} + \frac{4D_a}{(\rho(z))^2} \frac{r^2}{(\rho(z))^2} = 0$$

$$\wedge$$

$$-v_d \frac{\partial n_i(z,0)}{\partial z} - \frac{4D_a}{(\rho(z))^2} n_i(z,0) = 0 \quad (4.5)$$

The first part of Eq. (4.5) is a differential equation for $\rho(z)$ with the solution

$$\rho(z) = \left(\frac{4D_a}{v_d} z + (\rho(0))^2 \right)^{\frac{1}{2}} \quad (4.6)$$

with $\rho(0)$ the radius at the position $z = 0$. Substituting Eq. (4.6) into the second part of Eq. (4.5) leads to

$$\frac{1}{n_i(z,0)} \frac{\partial n_i(z,0)}{\partial z} + \frac{1}{\left\{ z + \frac{(\rho(0))^2 v_d}{4D_a} \right\}} = 0 \quad (4.7)$$

This is solved for $n_i(z,0)$

$$n_i(z,0) = n_i(0,0) \frac{1}{\left(\frac{4D_a}{v_d (\rho(0))^2} \right) z + 1} \quad (4.8)$$

with $n_i(0,0)$ the density on the axis at the position $z = 0$. Since there are no loss processes the total flux, Γ_i , coming from the arc is conserved. The flux is related to the density and the radius:

$$\Gamma_i = v_d \int_0^{\infty} n_i(z,r) \cdot 2\pi r dr = v_d \pi (\rho(0))^2 n_i(0,0) \quad (4.9)$$

The profile of the plasma is described by Eqs. (4.3), (4.6) and (4.8). The radial profile is a Gaussian at all positions z , with a $1/e$ width that increases with the square root of the axial position z . The density on the axis decreases as $1/z$.

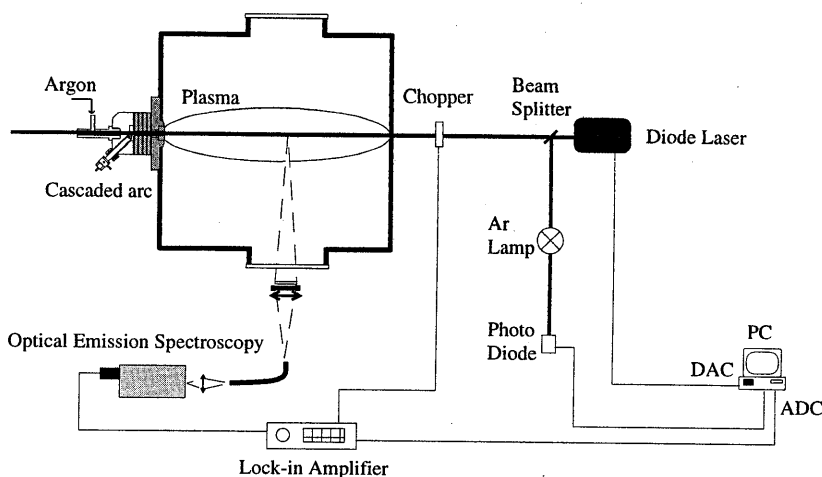


Figure 4.1: Setup for Laser Induced Fluorescence

4.3 Experimental Setup

To determine the velocity of the particles in the vessel resonant Laser Induced Fluorescence (LIF) was performed [7] on the $4s-4p$ transition of Ar at 811.531 nm. The laser is an EOSI LCU 2010 M external cavity diode laser. The laser can be roughly tuned by hand in the range of 790-840 nm. By changing the voltage on the piezo element of the grating the wavelength can be scanned over a range of 0.13 nm. The change in wavelength with changing piezo voltage was calibrated using a Michelson interferometer. The change in wavelength with applied voltage is 0.0131 nm/V.

The LIF setup is shown schematically (seen from above) in Fig. 4.1. The laser is setup at the end of the vessel, opposite to the arc. The laser is aligned with the arc and is shining through the arc when the setup is at $r = 0$. Before entering the vessel, the laser light is split by a beam splitter. Part of the light is passed through an argon spectral lamp. Behind the lamp a photodiode detects the intensity of the laser. This signal is measured and stored by the PC. When the laser is tuned to the resonant wavelength of the transition, part of the light will be absorbed by the argon inside the lamp. Since the gas inside the lamp is at rest, maximum absorption will occur at the resonant wavelength. The signal from the photodiode is used as an absolute calibration of the wavelength of the laser.

The laser light not deflected by the beam splitter is passed through a chopper, which is running at approximately 900 Hz. The light coming from the plasma is detected by the optical

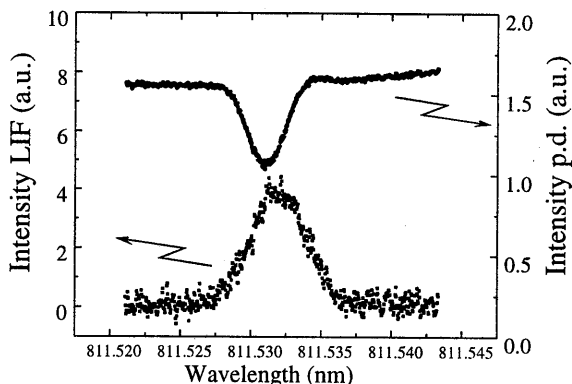


Figure 4.2: LIF measurement. The upper curve shows the absorption signal of the argon spectral lamp. The lower curve is the fluorescence signal from the plasma.

emission spectroscopy setup. The monochromator is tuned to the wavelength of the transition (811.531 nm). It has slit widths of 500 μm giving it a resolution of 0.8 nm, which is much larger than the linewidth of the emitted light. The monochromator in this setup acts as a narrow-band filter. The photomultiplier behind the exit slit of the monochromator gives a current proportional to the light coming from the 4s-4p transition in the plasma. To discriminate between the light coming from the plasma and the induced fluorescence, the signal is fed to a lock in amplifier that is frequency locked to the chopper behind the beam splitter. The output signal of the lock in is measured and stored by the PC. When performing a measurement, the PC scans the voltage on the piezo of the diode laser and measures the signal coming from the photodiode and the lock in amplifier. A typical measurement is shown in Fig. 4.2.

Since the plasma is moving towards the laser, it will absorb the light at a slightly lower wavelength, due to the Doppler shift. Maximum fluorescence will therefore take place at a lower wavelength than maximum absorption by the spectral lamp. The difference in wavelength, $\Delta\lambda$, is a measure of the drift velocity of the plasma, v_d

$$\frac{\Delta\lambda}{\lambda_0} = \frac{v_d}{c} \quad (4.10)$$

with λ_0 the wavelength of the transition (i.e. 811.531 nm), and c the velocity of light.

For particles with a Maxwellian velocity distribution, the fluorescence signal will be broadened by Doppler broadening resulting in a Gaussian profile with full width at $1/e$ maximum [11]

$$\Delta\lambda_D = \lambda_0 \left(\frac{8k_B T}{mc^2} \right)^{\frac{1}{2}} \quad (4.11)$$

with T the temperature and m the mass of the particles. From the width of the measured fluorescence signals, the gas temperature is determined.

In the present investigation measurements were performed at 50 A and 75 A of current through the arc and at vessel pressures of 225 Pa and 10 Pa. These settings encompass the typical window in which most experiments involving the expanding cascaded arc plasma are performed. The flow through the arc is 1 slm (standard liter per minute) argon. When LIF was attempted in pure argon it was found that the metastable (4s) density in the downstream plasma was too high for the laser to penetrate to the region of interest. To quench the density, 5% nitrogen was added downstream in the vessel during the LIF experiments. Since the mass of nitrogen is not too different from that of argon, it is assumed that the velocity and gas temperature is not affected by the presence of nitrogen.

In addition to the LIF measurements single cylindrical Langmuir probe measurements were performed (see Chapter 2). The electron temperature determined from these measurements is compared to the temperature of the metastable atoms. The Langmuir probe measurements also yield the spatial density distribution of ions and electrons. Since argon ions are only formed inside the arc source and not in the vessel (where the temperatures are in the range 0.2-0.3 eV), the spatial distribution of ions can be taken as an indication of the spatial distribution of all (active) particles coming from the arc. These particles are flowing downstream and diffusing to the walls (strictly speaking, neutral particles coming from the arc will have a different diffusion coefficient than ions and will consequently have a (slightly) different spatial density distribution but this effect is neglected here). The distribution of ions in the vessel was determined by measuring radial profiles at different axial positions.

Combining the LIF and probe measurements it is possible to map the behavior of the particles coming from the arc. The LIF measurements yield the forward velocity. The Langmuir probe measurements give the spatial distribution. From these two measurements, the diffusion coefficient needed to obtain such a distribution can be calculated. After that, the temperature leading to this diffusion coefficient is compared to the electron and metastable temperatures determined from the probe and LIF measurements.

4.4 Results

Drift velocity

The results of the LIF velocity measurements are shown in Fig. 4.3. Figure 4.3(a) shows the drift velocity as a function of axial position. In Fig. 4.3(b) the drift velocities are shown at different radial positions at a pressure of 10 Pa and arc current of 50 A. Only the component of the velocity in the z direction was measured. In Fig. 4.4 the gas temperatures are shown corresponding to the measurements of Fig. 4.3. The drift velocity is 300-600 m/s at a gas temperature of 2500-4000 K. These results are in good agreement with measurements by Fabry-Pérot interferometry [12] and calculations using the density before and behind the shock front [10]. The sonic velocity at that temperature is $\sqrt{5k_B T/3m} \approx 900-1100$ m/s, making the velocity subsonic. The assumption that the velocity is subsonic is one of the prerequisites for the validity of the diffusion solution, Eq. (4.1). In the solution of Eq. (4.2) the velocity and temperature were assumed to be constant over all z and r considered. The drift velocity in the z -direction (Fig. 4.3) shows significant dependency on position in the plasma. The velocity on the axis decreases by approximately 25-50% over a distance of 10 cm. The drift velocity also depends on the radial position in the plasma. At $z = 17$ cm there is a difference in velocity of approximately 25% between the measurement on the axis and at $r = 4$ cm. The decrease is less pronounced at greater distances from the nozzle. Only the component of the velocity in the axial direction was measured. It is possible that a small radial component of the velocity exists. This would also lead to a decrease in the axial component as a function of radius, while the total velocity remains constant. The effect of the decrease in velocity on the distribution of particles in the vessel will be discussed later, when the diffusion of ions is treated.

Temperature

The temperature determined from the LIF measurements is shown in Fig. 4.4. The temperatures found are in close agreement with emission spectroscopy measurements using Fabry-Pérot interferometry measurements [12, 9]. The measurements for the radial profile of the temperature (Fig. 4.4(b)) were taken at a different time than the measurements for the axial profile of the temperature (Fig. 4.4(a)). The measurements at $r = 0$ of Fig. 4.4(b) are within the experimental uncertainty of those taken on the axis for Fig. 4.4(a), showing good reproducibility for these measurements.

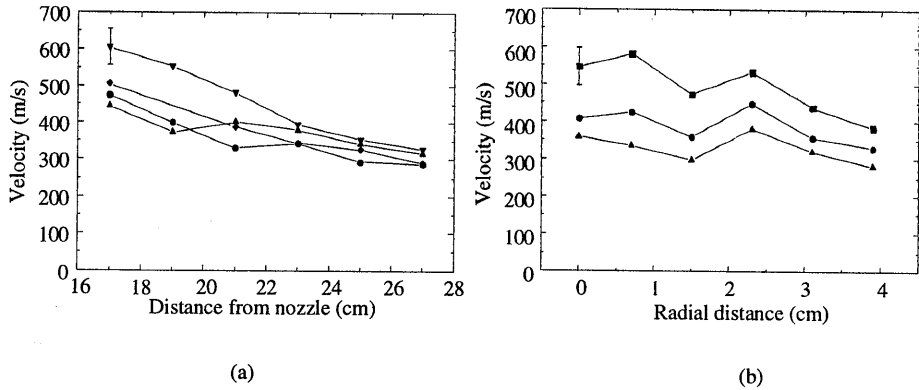


Figure 4.3: (a) Velocity as a function of distance from the nozzle at different plasma conditions: ∇ $p_{vessel} = 10 \text{ Pa}, I_{arc} = 50 \text{ A}$; \blacklozenge $p_{vessel} = 10 \text{ Pa}, I_{arc} = 75 \text{ A}$; \bullet $p_{vessel} = 225 \text{ Pa}, I_{arc} = 50 \text{ A}$; \blacktriangle $p_{vessel} = 225 \text{ Pa}, I_{arc} = 75 \text{ A}$. (b) Velocity as a function of radial distance at different axial positions, $p_{vessel} = 10 \text{ Pa}, I_{arc} = 50 \text{ A}$: \blacksquare 17 cm; \bullet 22 cm; \blacktriangle 26 cm.

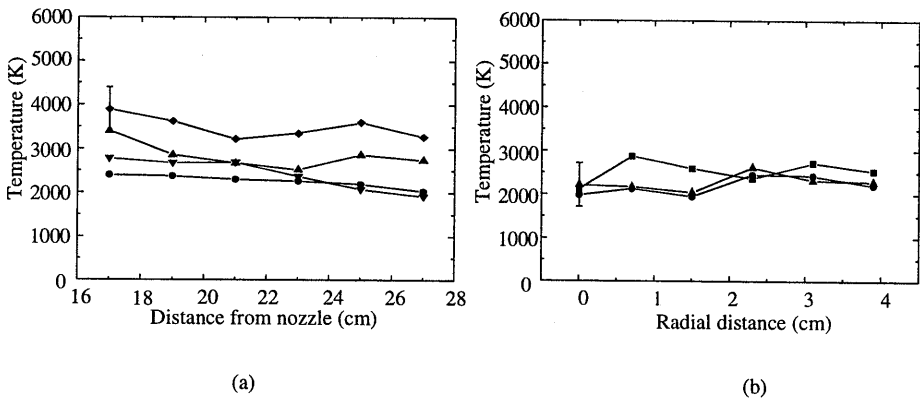


Figure 4.4: (a) Temperature as a function of distance from the nozzle at different plasma conditions: ∇ $p_{vessel} = 10 \text{ Pa}, I_{arc} = 50 \text{ A}$; \blacklozenge $p_{vessel} = 10 \text{ Pa}, I_{arc} = 75 \text{ A}$; \bullet $p_{vessel} = 225 \text{ Pa}, I_{arc} = 50 \text{ A}$; \blacktriangle $p_{vessel} = 225 \text{ Pa}, I_{arc} = 75 \text{ A}$. (b) Temperature as a function of radial distance at different axial positions, $p_{vessel} = 10 \text{ Pa}, I_{arc} = 50 \text{ A}$: \blacksquare 17 cm; \bullet 22 cm; \blacktriangle 26 cm.

The temperatures show no strong dependency on any of the parameters varied in these experiments. The temperature is slightly higher at higher arc current, most likely due to the higher power input from the arc.* The temperatures show no significant dependency on the position in the plasma. The gas temperature (and with that the ambipolar diffusion coefficient) may thus be taken as a constant over the part of the plasma under investigation here.

It can be observed that the background gas slows down the flow (Fig. 4.3), but it has no significant effect on the temperature (Fig. 4.4). The temperature of the background gas is comparable to that of the particles coming from the arc. The particles that desorb from the wall will most likely have a temperature comparable to the temperature of the wall (i.e. 300 K instead of 3000K). They are heated by collisions with particles from the plasma. The collision time between ions and neutral atoms at a pressure of 10 Pa is approximately 10^{-5} s (10^{-7} s at 225 Pa). With a flow velocity of 500 m/s the temperatures of ions and neutral particles are expected to be equal after only 5 mm. In the region where the measurements of Figs. 4.4 and 4.5 were taken (> 17 cm from the nozzle) the temperatures and velocity of particles coming from the plasma and those in the background gas will be completely equilibrated. The drift velocity of the plasma decreases with increasing distance from the nozzle because the momentum is distributed among the particles coming from the background and diffusing into the plasma stream. The temperature is kept high through the heat conductivity of the plasma.

The temperature determined by LIF can be compared to the electron temperature given by the probe measurements, shown in Fig. 4.5. The temperature determined from LIF is the temperature of the metastable 4s state and it can be seen from the comparison of Figs. 4.4 and 4.5 that the temperature of the 4s state is equal to the electron temperature. Although the Ar(4s) is a neutral particle it is formed by three-particle recombination followed by (fast) radiative decay or is coming directly from the arc. It is therefore to be expected that the temperature of these particles is equal to the ion temperature. Ions and metastable atoms undergo resonant charge or excitation transfer upon collisions with the background gas. With a typical collision time of 10^{-5} s the temperature of the background gas is expected to be equal to that of the particles coming from the arc. The collision time between electrons and ions is approximately 10^{-9} s when the electron density is 10^{19} m⁻³ (see Fig. 4.6). Because of the mass difference between the ions and electrons, the time for energy exchange is larger by a factor $m_i/2m_e$, i.e. 10^{-4} s. Still this time is short compared to typical transport times. The electron and ion temperatures are therefore also expected to be equal in the region of the current investigation.

* The behavior of Fig. 4.4 is to be expected as the temperature is determined by a balance of the thermal energy carried by the flow from the arc and the heat conduction to the walls of the vessel. Since the temperature in the arc increases slightly with arc current, the temperature in the downstream plasma should increase somewhat with arc current as can be observed in Fig. 4.4(a).

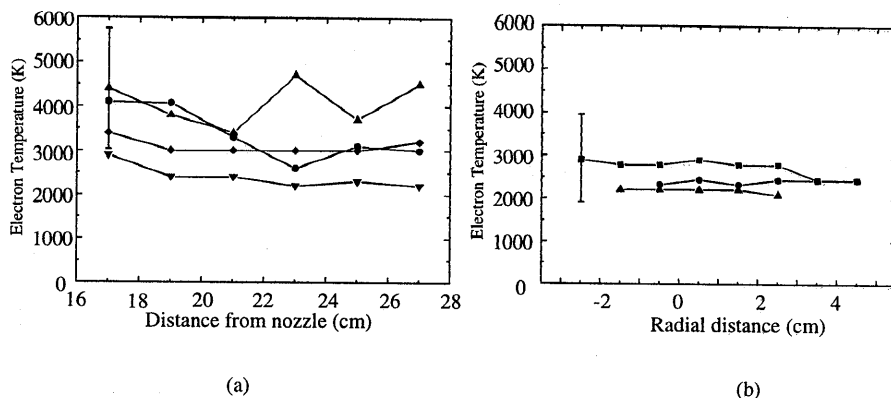


Figure 4.5: Temperatures determined by Langmuir probe (a) as a function of distance from the nozzle at different plasma conditions: ∇ $p_{\text{vessel}} = 10$ Pa, $I_{\text{arc}} = 50$ A; \blacklozenge $p_{\text{vessel}} = 10$ Pa, $I_{\text{arc}} = 75$ A; \bullet $p_{\text{vessel}} = 225$ Pa, $I_{\text{arc}} = 50$ A; \blacktriangle $p_{\text{vessel}} = 225$ Pa, $I_{\text{arc}} = 75$ A, (b) as a function of radial distance at different axial positions, $p_{\text{vessel}} = 10$ Pa, $I_{\text{arc}} = 50$ A: \blacksquare 17 cm; \bullet 21 cm; \blacktriangle 27 cm.

The total picture that emerges from the measurements of drift velocity and temperature, is that of a hot (3000 K) plasma flowing into the background vessel. There it is slowed down as it flows through the vessel, but is not significantly cooled. All temperatures (electron, ion and neutral gas) are equilibrated.

Diffusion

In Fig. 4.6(a) the ion density on the axis of the expansion is shown as a function of distance from the nozzle at a background pressure of 10 Pa. The density as a function of radial position is shown in Fig. 4.6(b) (only the measurements at 10 Pa background pressure and 50 A arc current are shown, corresponding to the LIF measurements of Fig. 4.3(b)). From (all) radial profiles, the radius of the plasma is found as a function of distance from the nozzle. This is shown in Fig. 4.6 for a background pressure of 10 Pa.[†]

[†] A similar analysis was attempted at the high background pressure of 225 Pa. However, at this high pressure it turned out that the flux of ions decreases with distance from the nozzle. This means that recombination of electrons and ions is taking place. The recombination is most likely caused by contamination of the background gas by a small flow of air leaking into the vessel. The leak of the vessel used is approximately 5×10^{-3} slm. Although this flow is small compared to the flow of the plasma (1 slm), the high pressure leads to a significant amount of (primarily) nitrogen in the vessel. At 225 Pa, the contamination of 0.5% leads to a nitrogen density of $8 \times 10^{19} \text{ m}^{-3}$. With a rate for charge exchange of $10^{-17} \text{ m}^3 \text{ s}^{-1}$, the rate of recombination is approximately 10^3 s^{-1} (see Chapter 5 through 7 for a more complete description of charge exchange and recombination in nitrogen plasmas). This will lead to a $1/e$ decrease length of the ion density of 70 cm, comparable to the decrease caused by diffusion. This makes the determination of the diffusive behavior and the diffusion coefficient at this pressure difficult.

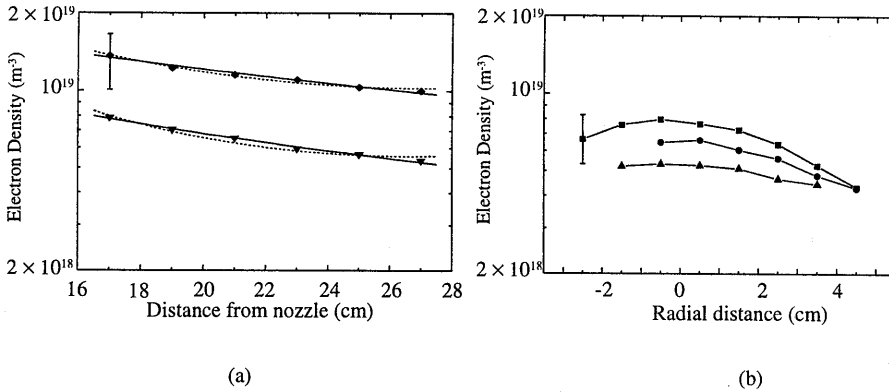


Figure 4.6: (a) Electron density as a function of distance from the nozzle at 10 Pa vessel pressure: ▼ $I_{arc} = 50$ A; ◆ $I_{arc} = 75$ A. Solid lines show a fit with constant drift velocity (Eq. (4.8)), dashed lines are fits with linearly decreasing drift velocity (Eq. (4.15)). (b) Electron density as a function of radial distance at different axial positions, $p_{vessel} = 10$ Pa, $I_{arc} = 50$ A: ■ 17 cm; ● 21 cm; ▲ 27 cm.

Equation (4.8) describes the electron density on the axis of the flowing plasma and Eq. (4.6) describes the development of the radius of the plasma. The starting point ($z = 0$) can be chosen arbitrarily. For easy comparison this is chosen at 17 cm from the nozzle. The determined density, $n_i(0,0)$, and radius, $\rho(0)$, are consequently the density and radius at 17 cm from the nozzle. For the drift velocity, v_d , the average velocity from Fig. 4.3(a) is taken over the range from 17 to 27 cm from the nozzle. These velocities are given in the second row of Table 4.1. The three parameters that can be determined from the measurements of Figs. 4.6(a) and 4.7 are the initial density, $n_i(0,0)$, initial radius, $\rho(0)$, and the (ambipolar) diffusion coefficient, D_a . Since the diffusion coefficient and initial radius are dependent in Eq. (4.8), first the values of $D_a/(\rho(0))^2$ and $n_i(0,0)$ are determined from a fit of Eq. (4.8) to the data of Fig. 4.6. The value of $\rho(0)$ is found after fitting Eq. (4.6) to the results of Fig. 4.7, while keeping the value of $D_a/(\rho(0))^2$ constant. Although in principle independent determination of D_a and $\rho(0)$ is possible directly by fitting Eq. (4.7) to Fig. 4.7, the uncertainties in the measurements of the radius leads to large uncertainties in both parameters. In fact, the values for D_a and $\rho(0)$ found in the procedure used here always lie within the uncertainties of the parameters when determined independently using only Eq. (4.7). The values of the parameters found for the measurements at 10 Pa are given in the top half of Table 4.1. The fitted curves are shown as solid lines in Figs. 4.6 and 4.7.

The diffusion constant, D_a , is related to the neutral (background) gas density, and by that to its temperature. The ambipolar diffusion of Ar^+ in Ar is [13]:

$$D_a = \left(1 + \frac{T_e}{T_i}\right) \frac{3.6 \times 10^{30} (k_B T_i)^{\frac{1}{2}}}{n_a} \quad (4.12)$$

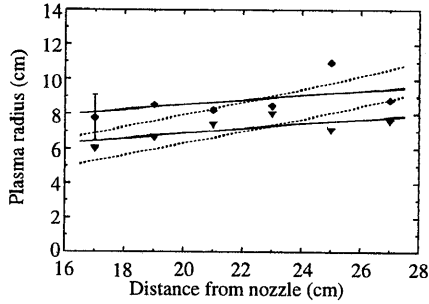


Figure 4.7: $1/e$ width of the plasma as a function of distance from the nozzle at 10 Pa vessel pressure: \blacktriangledown $I_{arc} = 50$ A; \blacklozenge $I_{arc} = 75$ A. Solid lines show a fit with constant drift velocity (Eq. (4.6)), dashed lines are fits with linearly decreasing drift velocity (Eq. (4.14)).

with n_a the neutral atom density, which can be related to its temperature using the ideal gas law. When Eq. (4.12) is used with the average electron temperature of 3000 K, to analyze the results of Table 4.1, the neutral gas temperature is found to be 1100 ± 500 K. The neutral gas temperature found this way is considerably lower than the temperatures (electron and metastable temperature) measured. A plausible explanation for this difference is the observed decrease in velocity (see Fig. 4.3), which apparently has to be included in the analysis.

Influence of decrease in drift velocity

The decrease in velocity observed earlier can be incorporated in the diffusion equation (Eq. (4.2)) by substituting a linearly decreasing drift velocity

$$v_d = v_0(1 - az) \quad (4.13)$$

with v_0 the velocity at $z = 0$, and a the deceleration (in m^{-1}). This leads to solutions for the radius, $\rho(z)$, and the density at $r = 0$, $n_i(z, 0)$, analogous to Eqs. (4.6) and (4.8) of

$$\rho(z) = \left(-\frac{4D_a}{v_0 a} \ln(1 - az) + (\rho(0))^2 \right)^{\frac{1}{2}} \quad (4.14)$$

and

$$n_i(z, 0) = n_i(0, 0) \cdot (1 - az)^{-1} \left[-\frac{4D_a}{v_0 a (\rho(0))^2} \ln(1 - az) + 1 \right]^{-1} \quad (4.15)$$

The values of v_0 and a are found by fitting Eq. (4.13) to the velocity measurements of Fig. 4.3(a). The results are given in the first row of the second half of Table 4.1. These values are used in Eqs. (4.14) and (4.15) that are fitted to the data in the same procedure as described above to find $n_i(0,0)$, $\rho(0)$, and D_a . The results are shown in the second half of Table 4.1 and are shown as dashed lines in Figs. 4.6(a) and 4.7. It must be noticed first, that the fits produced with Eqs. (4.14) and (4.15) (i.e. taking into account the deceleration of the plasma) are not better than the ones produced with Eqs. (4.6) and (4.8). It means that the effect of the deceleration on the density distribution of the particles is minimal, since it can be equally well described using the simpler equations. The fitted ambipolar diffusion coefficient does increase by a factor 2-3. The reason is that because the plasma is decelerating, the diffusion has to compensate for the pile up of particles caused by a decreasing flow rate in order to fit the measured data. The higher diffusion coefficient found in this more realistic analysis indicates a higher background gas temperature. Using Eq. (4.12) and the value of the diffusion coefficient of $6 \text{ m}^2/\text{s}$, the temperature of the background gas is found to be close to 3000 K. In this case all temperatures found are equal, as expected from the earlier calculations. This also shows that the determination of the diffusion coefficient and with that the neutral gas temperature depends rather strongly on the flow behavior of the plasma. Apparently, a constant drift velocity is not such a good approximation in this analysis.

		50 A	75 A
Constant drift velocity	v_d (m/s)	450 ± 110	380 ± 80
	$n_i(0,0)$ (10^{19} m^{-3})	0.778 ± 0.006	1.34 ± 0.02
	$\rho(0)$ (cm)	6.4 ± 0.2	8.1 ± 0.3
	D_a (m^2/s)	2.2 ± 0.7	2.2 ± 0.9
Linearly decreasing drift velocity	v_0 (m/s)	600 ± 15	490 ± 16
	a (m^{-1})	4.9 ± 0.3	4.3 ± 0.4
	$n_i(0,0)$ (10^{19} m^{-3})	0.799 ± 0.003	1.37 ± 0.02
	$\rho(0)$ (cm)	5.3 ± 0.3	6.9 ± 0.4
	D_a (m^2/s)	5.5 ± 1.1	6.0 ± 1.4

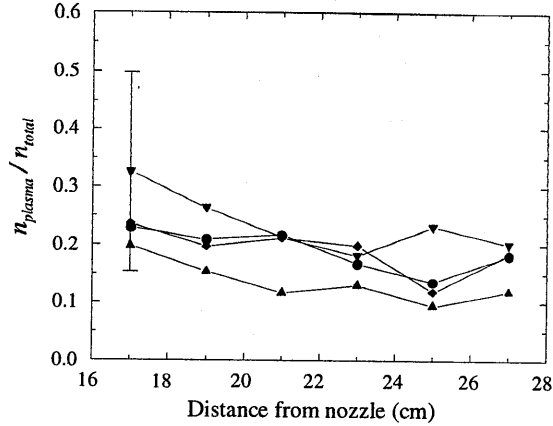


Figure 4.8: Ratio of density of particles coming from the plasma source to total particle density, calculated using the average (constant) velocity at each plasma setting. ∇ $p_{vessel} = 10$ Pa, $I_{arc} = 50$ A; \blacklozenge $p_{vessel} = 10$ Pa, $I_{arc} = 75$ A; \bullet $p_{vessel} = 225$ Pa, $I_{arc} = 50$ A; \blacktriangle $p_{vessel} = 225$ Pa, $I_{arc} = 75$ A

Flux

Using the total flow through the arc and measurements of the radial profiles it is possible to determine the density of the particles coming directly from the arc. If it is assumed that the radius of the profile of all particles coming directly from the arc is approximately equal to the radius of the ion profile determined by the Langmuir probe (see Fig. 4.7), the density of particles coming from the arc, at the center of the plasma, $n_{plasma}(z,0)$ is given by

$$n_{plasma}(z,0) = \frac{4.0 \times 10^{20}}{v_d \pi r(z)} \varphi \quad (4.16)$$

with φ the flow through the arc in slm. The factor 4.0×10^{20} comes from the calculation from standard liters per minute to number of particles per second. The total density of the particles is the sum of particles coming from the arc and the background gas particles. The total particle density, n_{total} , is given by the ideal gas law

$$n_{total} = \frac{p_{vessel}}{k_B T_{gas}} \quad (4.17)$$

with T_{gas} the gas temperature, and p_{vessel} the background pressure in the vessel. Using Eqs. (4.16) and (4.17) the ratio of the density of particles coming directly from the arc to the total particle density in the vessel may be determined. This ratio is shown in Fig. 4.8. In the

calculations leading to Fig. 4.8 it was assumed that the radial profile of all particles coming directly from the source is equal to the radius of the ion density profile, $\rho(z)$. In reality, the diffusion of neutral particles coming from the plasma will be slightly faster than for ions, so that the ratio shown in Fig. 4.8 is in fact the upper limit. Figure 4.8 shows that on the axis of the plasma, the total density of particles is made up of 10-30% particles coming from the plasma and 70-90% of particles recirculating in the vessel. Away from the axis the contribution of plasma particles will be lower. When this plasma source is used for, for example etching or deposition experiments, this result means that if active particles such as radicals or ions are only formed inside the arc source, the density of active particles at a substrate will be 30% or less of the total gas density (even if 100% of the gas in the arc is dissociated or ionized).

4.5 Conclusions

The drift velocity of particles coming from the plasma source was studied by resonant Laser Induced Fluorescence on metastable Ar(4s). The drift velocity in the vessel was found to be between 600 and 300 m/s and decreases with distance from the nozzle. The temperature of the metastable particles lies between 2500 and 4000 K. The electron temperature determined by single cylindrical Langmuir probe measurements lies in the same range. This is in agreement with calculations that show that all temperatures (electron, ion and neutral gas) are expected to be equal. The temperature remains constant over the region of the plasma investigated.

The density distribution of ions was described by the diffusion equation. When using a constant velocity and measurements of the ion density to calculate the ambipolar diffusion coefficient and background gas temperature both were found to be lower than expected from the temperature measurements. When the decrease in the drift velocity observed in the LIF measurements is taken into account, the ambipolar diffusion coefficient is found to be $5.7 \pm 1.1 \text{ m}^2/\text{s}$ and the neutral gas temperature $2900 \pm 900 \text{ K}$, i.e. close to the electron and metastable particle temperature. It must be concluded from these results that the decrease in drift velocity is important in a detailed analysis of plasma kinetics

Combining drift velocity and density measurements it was shown that the plasma is diluted with particles from the background diffusing into the plasma stream. In the region under investigation over 70% of the particles present are recirculating particles rather than particles coming directly from the arc. This has implications for particles that are lost at the wall, such as charged particles and reactive radicals. It means that even when they are produced in relatively large quantities, dilution with stable particles in the background will reduce their relative densities.

References

- 1 R.J. Severens, G.J.H. Brussaard, M.C.M. van de Sanden, and D.C. Schram, *Appl. Phys. Lett.* **67**, 491 (1995).
- 2 J.W.A.M. Gielen, M.C.M. van de Sanden, and D.C. Schram, *Appl. Phys. Lett.* **69**, 152 (1996).
- 3 J.J. Beulens, A.T.M. Wilbers, M. Haverlag, G.S. Oehrlein, G.M.W. Kroesen, and D.C. Schram, *J. Vac. Sci. Technol. B* **10**, 2387 (1992).
- 4 Chapter 8 of this thesis.
- 5 M.J. de Graaf, R.J. Severens, M.J.F. van de Sande, R. Meyer, H. Kars, M.C.M. van de Sanden, and D.C. Schram, *J. Nucl. Mat.* **200**, 380 (1993).
- 6 R.F.G. Meulenbroeks, D.C. Schram, M.C.M. van de Sanden, and J.A.M. van der Mullen, *Phys. Rev. Lett.* **76**, 1840 (1996).
- 7 W. Demtröder, *Laser Spectroscopy*, 2nd ed., Springer, Berlin (1996).
- 8 N. Sadeghi, M. van de Grift, D. Vender, G.M.W. Kroesen, and F.J. de Hoog, *Appl. Phys. Lett.* **70**, 835 (1997).
- 9 M.C.M. van de Sanden, J.M. de Regt, and D.C. Schram, *Plasma Sources Sci. Technol.* **3**, 501 (1994).
- 10 M.C.M. van de Sanden, R. van den Bercken, and D.C. Schram, *Plasma Sources Sci. Technol.* **3**, 511 (1994).
- 11 M. Mitchner, C.H. Kruger, *Partially ionized gases*, Wiley Interscience, New York (1973).
- 12 G.M.W. Kroesen, D.C. Schram, A.T.M. Wilbers, and G.J. Meeusen, *Contr. Plasma Phys.* **31**, 27 (1991).
- 13 V.M. Lelevkin, D.K. Otorbaev, and D.C. Schram, *Physics of Non-Equilibrium Plasmas*, North-Holland, Amsterdam (1992).

5 Ion Densities in a High Intensity, Low Flow Nitrogen-Argon Plasma

5.1 Introduction

High-density plasmas are commonly used in a variety of industrial applications [1]. Some of these sources are used for downstream processing, where the plasma production is separated from the treatment region. One such source is the expanding thermal arc [2, 3]. In a previous report [4] the electron and ion densities in the expanding nitrogen plasma were investigated. Because in many industrial applications pump capacity is limited the question arose to modify the plasma source to work at lower flows (total flow smaller than 500 standard cm³ per minute (scm)). Initial investigations creating argon plasmas in this regime are reported by Van de Sanden [5]. The current report (originally published as Ref. [6]) extends the investigation of the ion densities in the nitrogen expanding plasma to the low flow regime. A model for the gas phase reactions involving ions after the expansion of the plasma will be presented and compared to measurements.*

5.2 Experiments

The operation of the setup used is described in Chapter 1 of this thesis. In the experiments described here the current through the arc is set to 36 A. The voltage drop depends on the gas flow rate and gas composition and ranges from 50-100 V. No magnetic field was applied in this study. The argon gas is injected at the cathode side and is dissociated/ionized in the arc channel. The plasma is then let to expand supersonically into a low pressure chamber. Normally this plasma is operated at high flow rates, typically of the order of several standard liters per minute. To be able to use this plasma at flow rates in the range of 100-500 scm, the bore of the copper plates was varied, to increase the upstream pressure. It was found that operation was most reliable if six plates were used with bores varying between 4 and 1 mm (Fig. 5.1). The fourth plate, with a bore of 2 mm contains a seeding channel, through which nitrogen can be injected into the arc. An overview of all relevant parameters during the experiments is given in Table 5.1.

* Since the original publication of the work described in this chapter (Ref. [6]) some of the insights have changed, such as estimates for the drift velocity and diffusion (see chapter 4 of this thesis) and details of the recombination mechanism (chapters 6 and 7 of this thesis). However, in this chapter the original publication is reproduced without adaptation to later insights. It should be viewed as a first general investigation of the behavior of ions in plasmas containing nitrogen, with the specific technical adjustment for the low-flow regime.

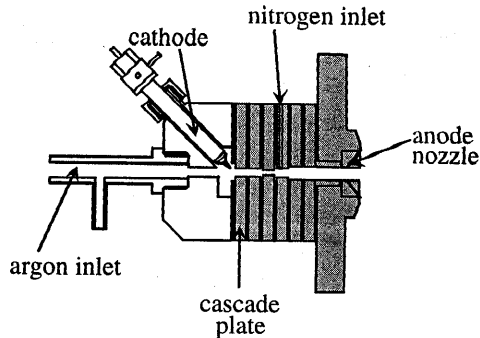


Figure 5.1: Cascaded arc with varying channel bores

The Langmuir probe used to determine the plasma density is a tungsten disc with a radius of 2 mm. The backside and edges of the probe are shielded off by a ceramic (Al_2O_3) tube. This probe is more extensively described in Chapter 2.1. The probe is placed on the axis of the expanding plasma with the normal to the probe surface parallel to the expansion. The probe can be controlled by a movable arm to measure at different positions in the plasma.

A pure argon plasma was created with a total flow of 500 sccm. Because extensive research has been carried out on the expanding argon jet [2, 5, 7, 8] this plasma can be used as a means of calibrating the probe measurements [9] and investigate the workings of the arc under the conditions of low flow. The electron density was measured by the Langmuir probe, as a function of distance from the nozzle. The results are shown in Fig. 5.2. The background pressure in the vessel is 7 Pa, the electron temperature behind the shock is approximately 0.2 eV [10]. The decrease of electron density as a function of distance from the nozzle is caused by recombination and diffusion. The three particle recombination

Table 5.1: Overview of experimental conditions	
Ar flow	500-100 sccm
N ₂ flow	0-400 sccm
Arc current	36 A
Downstream ($z > 10$ cm):	
Chamber pressure	7 Pa
Electron density	$10^{17} - 10^{19} \text{ m}^{-3}$
Electron temperature	0.1 - 0.3 eV

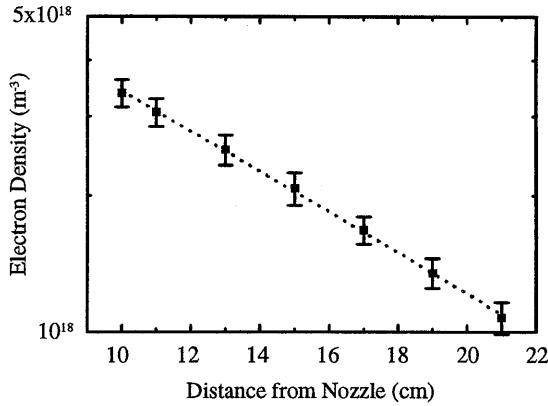


Figure 5.2: Measured (■) and fitted (dashed line) electron densities in an argon plasma, as a function of distance from the nozzle.



has (with $T_e = 0.2$ eV) a rate of $k_1 \approx 0.1\text{-}2 \times 10^{-36}$ (m^6s^{-1}) [7]. The decrease of electron density through recombination can be calculated as a function of distance from the nozzle:

$$\frac{\partial n_e}{\partial z} = -n_e^3 k_1 \frac{1}{v_d} \quad (5.2)$$

where v_d is the forward drift velocity, which is assumed to be constant.

With the initial condition $n(z=0) = n_{e0}$, this is solved to:

$$n_e(z) = \left(2k_1 z \frac{1}{v_d} + \frac{1}{n_{e0}^2} \right)^{-1/2} \quad (5.3)$$

With the plasma parameters given above a drift velocity v_d of 600 m/s [2], and an initial density n_{e0} of 10^{19} m^{-3} the density is reduced to $0.5 n_{e0}$ at $z = 4.5$ m. It is clear from these calculations that recombination cannot explain the observed decrease in electron density on the axis of this argon plasma. This means that the loss of electron density on the axis is dominated by diffusion towards the walls.

The mass balance in steady state, neglecting recombination, is given by:

$$-\bar{\nabla} \cdot (D_a \bar{\nabla} n_e) + \bar{\nabla} \cdot (n_e \bar{v}_d) = 0 \quad (5.4)$$

with D_a the ambipolar diffusion coefficient. This equation can be solved analytically in several different ways, each with its own set of assumptions. Although the different methods lead to

slightly different axial density profiles they all have a typical decay length ($1/e$ length) of approximately

$$\ell_{decay} = \frac{R_0^2 v_d}{4D_a} \quad (5.5)$$

where R_0^2 is the plasma radius, which is almost constant for the downstream plasma ($z > 10$ cm), see for example [11]. The decay length of the electron density can be estimated, using the ambipolar diffusion coefficient, D_a :

$$D_a = \left(1 + \frac{T_e}{T_i}\right) \frac{3.6 \times 10^{30} (kT_i)^{\frac{1}{2}}}{n_a} \quad (5.6)$$

With $T_i = T_e \approx 0.2$ eV, a gas temperature of 500 K and pressure $p = 7$ Pa, the collision time τ_{ia} is approximately 10^{-6} s, according to [12]. This leads to a diffusion coefficient $D_a \approx 1 \text{ m}^2 \text{ s}^{-1}$. An estimated plasma radius of 3 cm and a drift velocity of 600 m s^{-1} result in a $1/e$ decay length for the electron density of approximately 14 cm. For $r = 0$, an exponential fit to the measured data is shown as the dashed line in Fig. 5.2. The effective decay length fitted is 10 cm. Taking into account the uncertainty in several of the parameters used in estimating the rate of decrease, it is possible to conclude that the observed decay can be explained through diffusion.

An extrapolated initial density $n(0,0)$ of $9.4 \times 10^{18} \text{ m}^{-3}$ is found. This can be compared to results in the high flow regime (flow > 3500 sccm) by Van de Sanden et al. [2] who found that the ion density scales approximately linearly with arc current and background pressure. Extrapolating their results (as an example: arc current = 45 A, background pressure = 40 Pa, initial ion density = $5 \times 10^{19} \text{ m}^{-3}$) to the settings used here predicts an initial density of $5 \times 10^{18} \text{ m}^{-3}$. The initial density in the plasma under investigation in this report is therefore a factor of two higher. This may be attributed to a relatively higher pressure inside the arc caused by the smaller bore of the central plates used (see Fig. 5.1) when operating at lower flow.

The results found in argon can now be used as a basis for understanding the results in the nitrogen/argon mixtures. Some extra considerations have to be made because, as will be shown, reactions in the gas phase are no longer negligible. Inside the arc the temperatures are high ($T_i \approx T_e \approx 1$ eV) as well as the electron density ($n_e \approx 10^{22} \text{ m}^{-3}$). Therefore, the relative abundance of the ions can be calculated using pLTE considerations. The ions will be atomic ions only and their relative density is given by

$$\frac{n_{N^+}}{n_{Ar^+}} = \frac{g(N^+)}{g(N)} \frac{g(Ar)}{g(Ar^+)} \frac{N_{flow}}{Ar_{flow}} e^{\left(\frac{E_{Ar^+} - E_{N^+}}{T_e}\right)} \quad (5.7)$$

with n_{N^+} , n_{Ar^+} the density of N^+ and Ar^+ , $g(\dots)$ the statistical weights of the different particles, and E_{\dots} the ionization energy for each atom. For the purpose of modeling and understanding

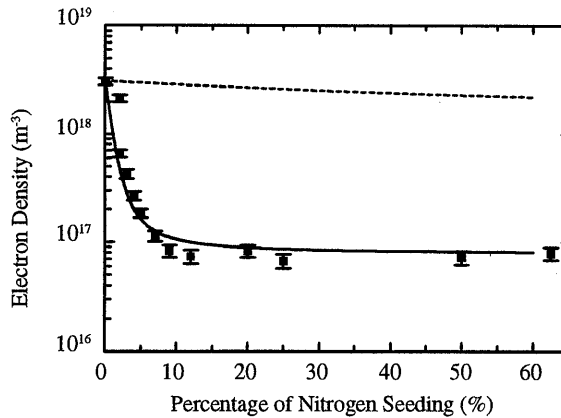
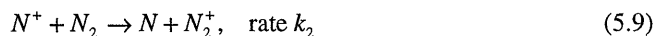
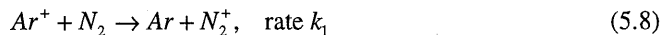


Figure 5.3: Measured (■) and modeled (solid line) electron densities as a function of nitrogen seeding. The rate constants used for the modeling are $k_1 = 4 \times 10^{-16} \text{ m}^3 \text{ s}^{-1}$, $k_2 = 2 \times 10^{-16} \text{ m}^3 \text{ s}^{-1}$ and $k_3 = 4.5 \times 10^{-13} \text{ m}^3 \text{ s}^{-1}$. The dashed line shows the decrease of electron density through diffusion of N_2^+ .

the reactions taking place in the expansion, it is assumed that the relative density given by Eq. (5.7) still exists just after the shock in the expansion. This assumption seems justified because the compression of the atomic ions in the shock will be smaller than a factor of four [2] and three-particle recombination will still be negligible. The influence of varying the relative flow of the gases into the arc on the electron density and relative ion densities downstream is investigated. The results of the Langmuir probe measurements are shown in Figs. 5.3 and 5.4(a). In Fig. 5.3, the electron density on the expansion axis, at a distance of 15 cm from the nozzle, is shown as a function of relative nitrogen flow. In Fig. 5.4(a) the ratio of electron to ion saturation current is shown. The ratio of electron to ion saturation current is equal to the square root of the mass ratio of electrons to ions (see Chapter 2) and is therefore a measure for the relative ion densities.

To understand these results, it is necessary to incorporate some recombination reactions in the mass balance equation (Eq. (5.4)). The dissociated and ionized gas coming from the arc expands into a background of neutral argon and molecular nitrogen formed on the vessel walls. The following reactions will determine the densities of the different species:

Charge exchange:



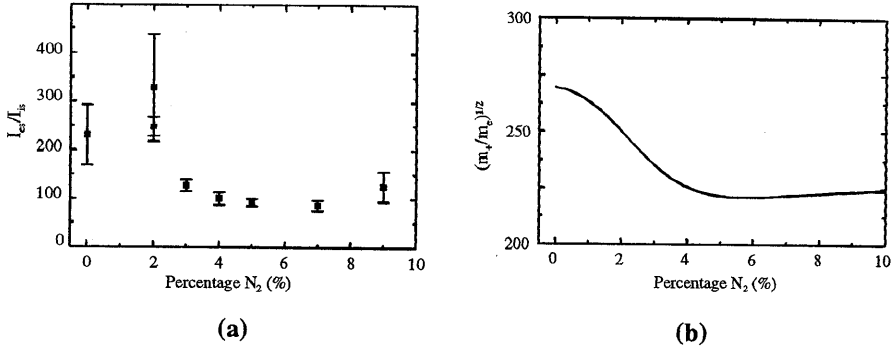


Figure 5.4: Ion to electron mass ratios as a function of nitrogen seeding. Values determined from probe measurements (a) and calculated (b), using the same rate constants as in Fig. 5.3.

Recombination:



At $T_e \approx 0.2$ eV, the charge exchange rates k_1 and k_2 are estimated to be $7 \times 10^{-17} \text{ m}^3 \text{ s}^{-1}$ [13] and $1 \times 10^{-16} \text{ m}^3 \text{ s}^{-1}$ [14] respectively. The rate of the dissociative recombination, k_3 , is estimated at $10^{-13} \text{ m}^3 \text{ s}^{-1}$ [15]. With a drift velocity of 600 m/s and the rates given above, diffusion away from the expansion axis is negligible compared to charge exchange and recombination for a relative nitrogen flow above approximately 1% and electron densities larger than 10^{17} m^{-3} . This is also shown by the dashed line in Fig. 5.3. Equation (5.4) can now be rewritten as a set of rate equations:

$$\frac{\partial n_{Ar^+}}{\partial z} = -k_1 n_{Ar^+} n_{N_2} v_d \quad (5.11)$$

$$\frac{\partial n_{N^+}}{\partial z} = -k_2 n_{N^+} n_{N_2} v_d \quad (5.12)$$

$$\frac{\partial n_{N_2^+}}{\partial z} = k_1 n_{Ar^+} n_{N_2} v_d + k_2 n_{N^+} n_{N_2} v_d - k_3 n_{N_2^+} n_e v_d \quad (5.13)$$

where $n_e = n_{Ar^+} + n_{N^+} + n_{N_2^+}$ follows from quasi neutrality. These equations are solved numerically.

Allowing some variations in the rate constants, a fit to the measured data is shown as the solid line in Fig. 5.3. The rates used to obtain a good fit are $k_1 = 2 \times 10^{-16} \text{ m}^3 \text{ s}^{-1}$, $k_2 = 1 \times 10^{-16} \text{ m}^3 \text{ s}^{-1}$

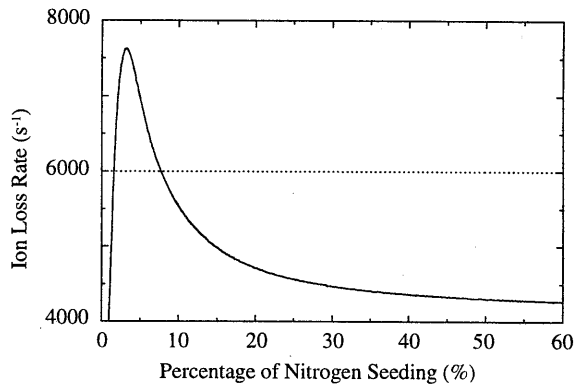


Figure 5.5: Total ion loss rate, A_{ion} , due to diffusion (dashed line) and due to recombination (solid line) as a function of nitrogen seeding.

and $k_3 = 0.5 \times 10^{-13} \text{ m}^3 \text{ s}^{-1}$. The absolute value of these rates depends linearly on the drift velocity. The fitted values for the rates k_1 and k_2 also depend on the neutral gas temperature. Within the uncertainties introduced by these dependencies, the values fitted compare reasonably to the theoretical values given above. The same rate constants are used to calculate the ion to electron mass ratio in the plasma. This is shown in Fig. 5.4(b). Although the experimentally determined ratios (Fig. 5.4(a)) and the calculated ones differ in absolute value, the trend towards lighter ions is visible. The difference in absolute values is possibly caused by small offsets in the measuring circuitry, which has great influence on the ion saturation current and therefore on the current ratio.

The model predicts that at seeding percentages of nitrogen larger than approximately 10% the plasma will consist of predominantly N_2^+ ions. The plasma density downstream drops to below 10^{17} m^{-3} . At these low electron densities the dissociative recombination becomes small. If a total ion loss rate, A_{ion} , is defined as

$$A_{ion} = \frac{1}{n_e} \frac{\partial n_e}{\partial t} \quad (5.14)$$

it is possible to distinguish between the loss rate due to recombination and the loss rate due to diffusion. This is shown in Fig. 5.5, where the loss rates are shown as a function of nitrogen seeding, at a distance of 15 cm from the nozzle. From these calculations it follows that at a nitrogen seeding of more than 10% the main loss process is diffusion towards the wall. The plasma density as a function of distance from the nozzle with a nitrogen seeding of 80% is shown in Fig. 5.6, where the solid line is an apparent linear fit resulting in a $1/e$ decay length

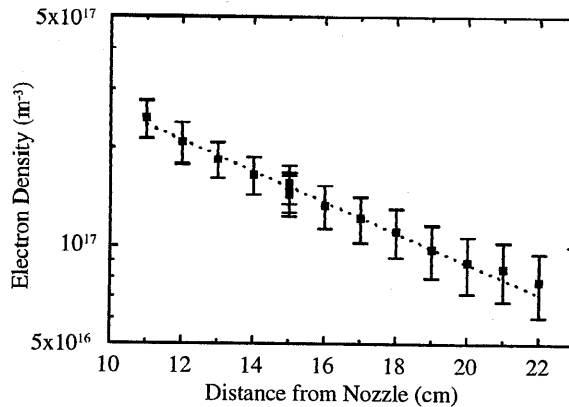


Figure 5.6: measured and modeled electron densities as a function of distance from the nozzle.

of 9 cm. This decay length is comparable to the one found in argon since the N_2^+ ions will have resonant charge exchange with the N_2 in the background, similar to Ar^+ in argon. The diffusion coefficient of N_2^+ is expected to be smaller by a factor of $\sqrt{28/40}$ (the square root of the mass ratio), but this will be partly compensated by the dissociative recombination and a higher drift velocity.

The results obtained here with the plasma in the low flow regime can be compared to results found by Dahiya et al. [4] in a similar plasma at higher flow (>1000 sccm). Although the same (charge exchange and dissociative recombination) reactions are taking place, the dominant ion found in the mass spectrometer by Dahiya et al. is N^+ . This is due to the fact that the ion densities at higher flow are higher, typically of the order of 10^{18} m^{-3} at a distance of 20 cm from the nozzle.

5.3 Conclusions

It was shown that the decrease of the plasma density as a function of the distance to the nozzle in a low flow (500 sccm) argon plasma can be explained by diffusion away from the expansion axis. The decay length is 10 cm. In the case that nitrogen is seeded into the arc plasma the plasma density is lowered considerably due to charge exchange and dissociative recombination. At nitrogen flows larger than 10% the plasma density at 11 cm from the nozzle is slightly less than 10^{17} m^{-3} and does not decrease further with higher partial nitrogen flow. The dominant ion in this case is molecular ion N_2^+ . Because of the low electron density at high percentages of nitrogen, the dissociative recombination becomes slow. The main loss process of ions in this case is diffusion away from the plasma axis. The effective decay length found is 9 cm.

References

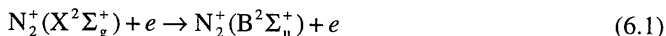
- 1 see for example M.A. Lieberman and A.J. Lichtenberg, *Principles of Plasma discharges and material processing* (John Wiley & Sons, Inc. New York, 1994).
- 2 M.C.M. van de Sanden, J.M. de Regt and D.C. Schram, *Plasma Sources Sci. Technol.* **3**, 501 (1994).
- 3 G.J. Meeusen, R.P. Dahiya, M.C.M. van de Sanden, G. Dinescu, Zhou Qing, R.F.G. Meulenbroeks, and D.C. Schram, *Plasma Sources Sci. Technol.* **3**, 521 (1994).
- 4 R.P. Dahiya, M.J. de Graaf, R.J. Severens, H. Swelsen, M.C.M. van de Sanden, and D.C. Schram, *Phys. Plasmas* **1**, 2086 (1994).
- 5 M.C.M. van de Sanden, and J.A. Tobin, *Plasma Sources Sci. Technol.* **7**, 28 (1997).
- 6 G.J.H. Brussaard, M.C.M. van de Sanden, and D.C. Schram, *Phys. Plasmas* **4**, 3077 (1997).
- 7 M.C.M. van de Sanden, J.M. de Regt, and D.C. Schram, *Phys. Rev. E* **47**, 2792 (1993).
- 8 M.C.M. van de Sanden, R. van den Bercken, and D.C. Schram, *Plasma Sources Sci. Technol.* **3**, 511 (1994).
- 9 R.F.G. Meulenbroeks, M.F.M. Steenbakkens, Z. Qing, M.C.M. van de Sanden, and D.C. Schram, *Phys. Rev. E* **49**, 2272 (1994).
- 10 R.F.G. Meulenbroeks, P.A.A. van der Heijden, M.C.M. van de Sanden, and D.C. Schram, *J. Appl. Phys.* **75**, 2775 (1994).
- 11 R.F.G. Meulenbroeks, A.J. van Beek, A.J.G. van Helvoort, M.C.M. van de Sanden, and D.C. Schram, *Phys. Rev. E* **49**, 4397 (1994).
- 12 V.M. Lelevkin, D.K. Otorbaev, and D.C. Schram, *Physics of Non-equilibrium Plasmas*, North-Holland, Amsterdam (1992).
- 13 W. Lindinger, F. Howorka, P. Lukac, S. Kuhn, H. Villinger, E. Alge, and H. Ramler, *Phys. Rev. A* **23**, 2319 (1981).
- 14 S.C. Brown, *Basic Data of Plasma Physics, 1966*, 2nd ed. M.I.T. Press, Cambridge, Massachusetts (1966).
- 15 J.B. Hasted, *Physics of Atomic Collisions*, 2nd ed. Butterworths, London (1972).

6 Evidence for charge exchange between N^+ and $N_2(A^3\Sigma_u^+)$ in a low temperature nitrogen plasma

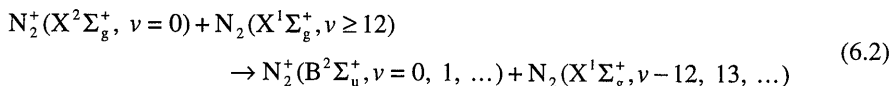
6.1 Introduction

Nitrogen plasmas are used in a wide variety of applications ranging from deposition of nitrides to the study of reentry phenomena of spacecraft. As the most abundant constituent of air, nitrogen also plays an important role in many open, atmospheric plasmas. This has led to extensive study of the phenomena in nitrogen plasmas and the modeling of reactions taking place. Especially the so-called long-lived or red afterglow of nitrogen molecules has fascinated scientists since the early days of plasma science [1]. Another phenomenon is the appearance of the short-lived or pink afterglow. The latter is the focus of the research presented in this chapter.

Kinetic modeling has proven to be a powerful tool in the study of the aforementioned phenomena. Especially the modeling of neutral molecule densities and atomic densities in the afterglow of DC discharges has provided detailed insight in the kinetics of the nitrogen plasma [2, 3, 4, 5, 6]. However, only few publications include results on the modeling of excited molecular ions. This could elucidate the matter further, since one of the most prominent features in the spectra of most nitrogen plasmas is the emission from molecular ions, the so-called First Negative System ($N_2^+(B^2\Sigma_u^+) \rightarrow N_2^+(X^2\Sigma_g^+) + h\nu$). One of the features studied in detail is the creation of ions in the afterglow. It is (and has been for some time) suggested that excited neutral molecules react to generate ions and electrons [7, 8, 9]. The subsequent excitation of these molecular ions is not well understood and possibly depends on the nature of the system used in creating the plasma. Generally, only two reactions are included in the kinetic models to account for population of excited N_2^+ , direct excitation by electron impact



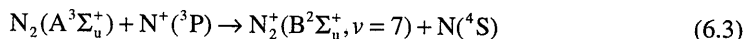
and population via V-E (Vibrational to Electronic) exchange with (highly) vibrationally excited ground state molecules



Reaction Eq. (6.1) requires electron energies of approximately 3 eV. Since the electron temperature in the afterglow region of most plasmas is only a few tenths of an eV, this reaction can only be significant if a large overpopulation exists in the high-energy tail of the electron energy distribution. Such overpopulation would also impact the distribution of neutral molecules among their different states. Since this is not observed, the direct excitation

by electron impact is usually neglected in kinetic models of the pink afterglow [10]. The second reaction is therefore the only reaction used in the modeling of excited molecular ions in the afterglow. Again, 3 eV is necessary to excite the molecular ion. If the neutral nitrogen molecules involved are vibrationally excited with vibrational quantum numbers larger than 12, this reaction may occur. Kinetic modeling of vibrational levels in the neutral nitrogen molecules suggests that a rather large overpopulation with respect to a Boltzmann distribution may exist around and above the level $v = 12$ [11, 12]. This would mean that a fraction of approximately 10^{-3} of the total neutral molecular density has sufficient internal energy.

All of the experiments and models referred to above involve either DC glow or microwave discharges. In recent years, spurred by interest from industry, high intensity remote plasma sources have undergone rapid development. Although the observations made in these plasmas show similarity to those in the flowing glow discharges discussed earlier, the reactions differ significantly. In this chapter we will report evidence of an alternative reaction path for the population of excited molecular ions, that is likely to occur under afterglow conditions in high intensity remote plasmas. The reaction proposed here is the charge exchange between ground state atomic ions, $N^+(^3P)$, and metastable neutral molecules in the $N_2(A^3\Sigma_u^+)$ state.



Experiments have not yet clarified the source of the metastable $N_2(A^3\Sigma_u^+)$. One possibility is that it is formed on the walls of the vessel by association of two $N(^4S)$ atoms, another possibility is formation inside the arc. If $N_2(A^3\Sigma_u^+)$ is formed in the arc it can only survive if it remains at the edge of the plasma. In the center of the plasma, the electron density is high, so de-excitation or dissociation will occur. So, the only $N_2(A^3\Sigma_u^+)$ from the arc that can survive the first expansion must come from the edge of the plasma, where temperatures and electron density are much lower. If $N_2(A^3\Sigma_u^+)$ is formed through wall association in the vessel it will recirculate (diffuse) into the flowing plasma. This means that there is no real difference from a kinetic point of view between formation in the (edges of the) arc plasma and formation in the vessel. Further research is currently underway to determine the origin of the metastable molecules (see also Chapter 7 of this thesis). In Fig. 6.1 the proposed reaction is shown in a simplified potential energy diagram.

6.2 Experiments

In the experiments described a cascaded arc is used as a remote plasma source for the production of nitrogen ions and radicals. The source is extensively described in Chapter 1 of this thesis and, for example Ref. [13]. From cathodes to the anode nozzle a DC current is drawn which can be varied between 40 and 75 A. Inside the arc the pressure is of the order

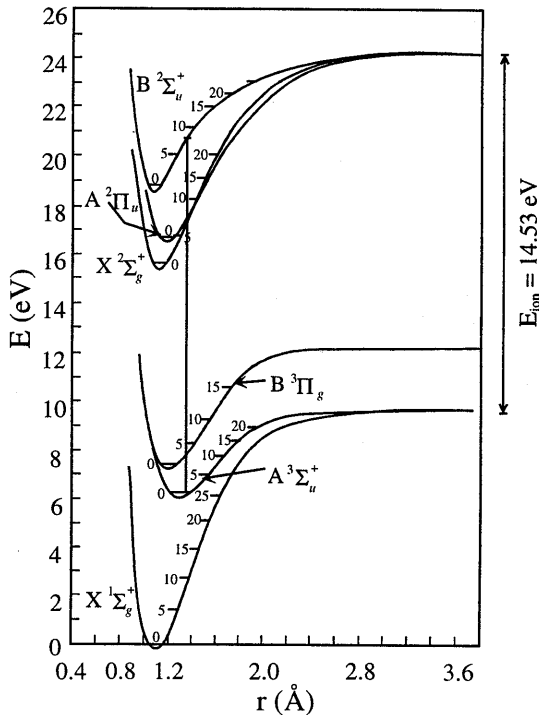


Figure 6.1: Simplified potential energy diagram of N_2 and N_2^+ . The vertical line shows the proposed transition from the metastable ($A^3\Sigma_u^+$) state. The numbers indicate the vibrational levels.

$10^4 - 10^5$ Pa. The electron density and temperature are high ($n_e = 10^{22} \text{ m}^{-3}$, $T_e = 1 \text{ eV}$) producing a plasma with high dissociation (up to 100 %) and ionization degree (approximately 10 %) [14, 15]. This plasma is let to expand through the nozzle into a low pressure chamber where it can be used for surface modification or the deposition of thin layers [16, 17]. The chamber is 40 cm long and has an internal diameter of 40 cm. The pressure inside the chamber is set to 225 Pa, at a total nitrogen flow rate of 1000 sccm (standard cubic centimeter per minute).

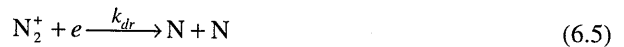
Langmuir probe measurements are carried out to determine the electron density and temperature in the flowing afterglow. The electron density and temperature were determined on the axis of the flow at settings of the current through the arc of 50, 65 and 75 A. Optical emission spectroscopy was carried out at the same positions as the Langmuir probe measurements. To obtain the local emissivity, a lateral scan was made and an Abel inversion was performed. The emission from five bands of the first negative system ($\Delta v = -2$ to $\Delta v = +2$) is shown in Fig. 6.2(a) through (e). The vibrational energy of both upper and lower states was

calculated using the location of all the reported transition in Lofthus and Krupenie [18] and making a fit of the vibrational energy with a third order polynomial. The predicted location of the bands is in concordance with the measured spectra and agrees with ref. [18] with one exception: The calculated and measured wavelength for the transition 7→9 is 4437 Å, whereas ref. [18] places it at 4459 Å. It is the opinion of the authors that the transition was misidentified in ref. [18]. A simulation using a model developed by Aldea et al. [19] was fitted to the bands in order to determine relative densities of the vibrational states. The result of the simulations is shown as dashed lines in Fig. 6.2. The relative population as a function of vibrational quantum number v' of $N_2^+(B^2\Sigma_u^+)$ determined from these fits is shown in Fig. 6.3. The most remarkable feature in both Figs. 6.2 and 6.3 is the strong overpopulation of the vibrational levels 6 and 7. This strongly suggests that a significant part of $N_2^+(B^2\Sigma_u^+)$ is populated via charge exchange between ground state atomic ions and metastable molecules in the electronic A-state and vibrational ground state (Eq. (6.3)). This reaction is energetically resonant when it leads to vibrational level 7 of $N_2^+(B^2\Sigma_u^+)$ and the internuclear distance of the original molecule is equal to the internuclear distance in the molecular ion, thus allowing for a direct transition (according to the Franck-Condon principle) without the necessity to form a complex N_3^+ first. The population of the lower vibrational levels ($v = 0-4$) may be explained by a similar charge exchange leading to the 2D ground state of N instead of the 4S state. The energy needed for this reaction (0.4 eV) is available in kinetic energy, but the Franck-Condon overlap is much smaller.

An additional indication can be found to distinguish between formation of $N_2^+(B^2\Sigma_u^+)$ through V-E exchange (Eq. (6.2)) on one hand and charge exchange (Eq. (6.3)) on the other hand. In Fig. 6.4 the emitted intensity from the first negative system is shown as a function of electron density. At high electron densities ($>2 \times 10^{16} \text{ m}^{-3}$), the dependence is first order; at lower densities it becomes a higher order dependence. As mentioned, inside the arc discharge, electron density and temperature are high [14] ($n_e = 10^{22} \text{ m}^{-3}$ and $T_e = 1 \text{ eV}$, respectively). Consequently the dominant ion in this region is the atomic ion N^+ [20]. In the afterglow region, the ion density distribution is governed by charge exchange and dissociative recombination according to the following generalized scheme [20]:



followed by



with k_{ce} and k_{dr} the rates for charge exchange and dissociative recombination respectively.

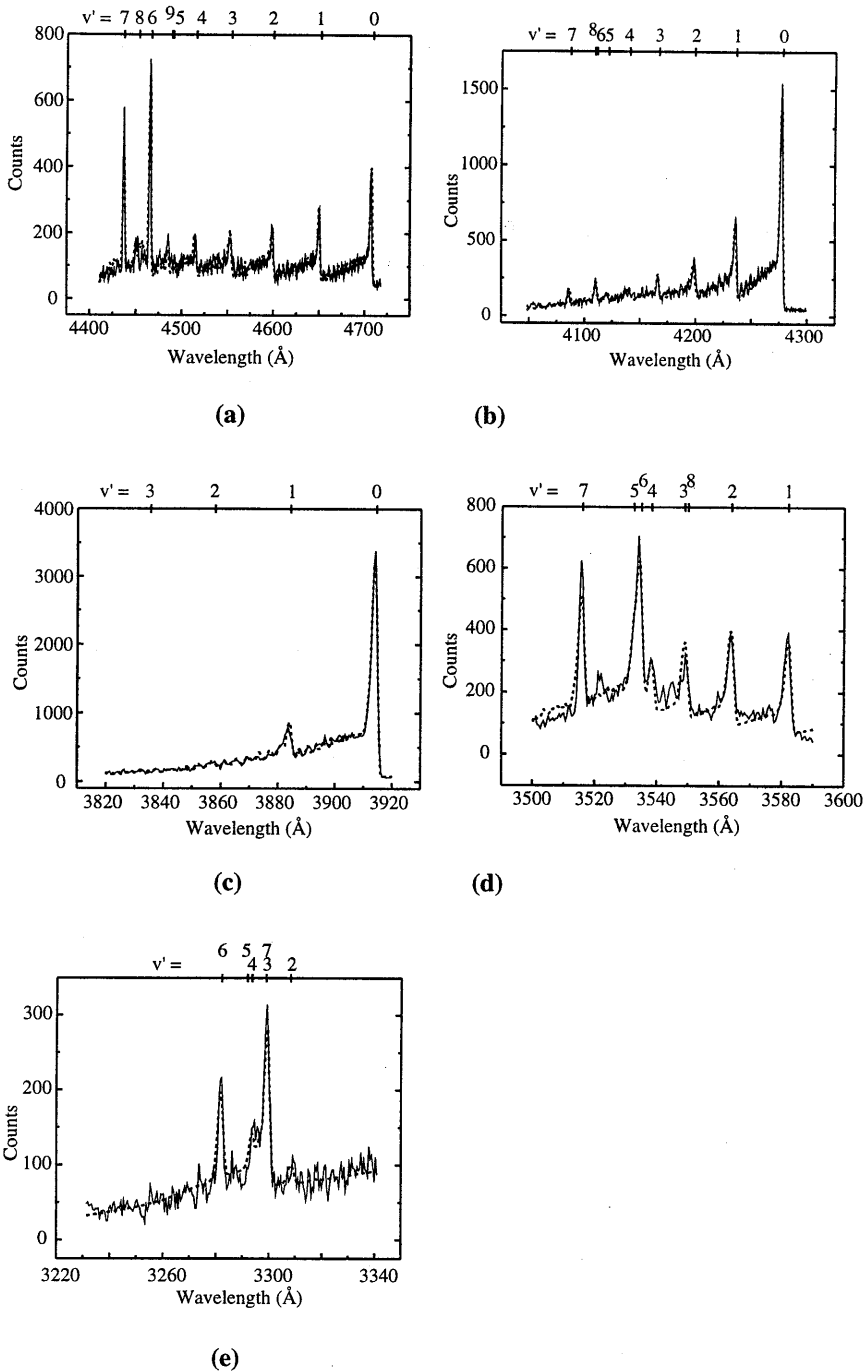


Figure 6.2: Emission spectra of the first negative system $N_2^+(B^2\Sigma_u^+) \rightarrow N_2^+(X^2\Sigma_g^+) + h\nu$. The bands shown are (a) $\Delta v = -2$, (b) $\Delta v = -1$, (c) $\Delta v = 0$, (d) $\Delta v = +1$, and (e) $\Delta v = +2$.

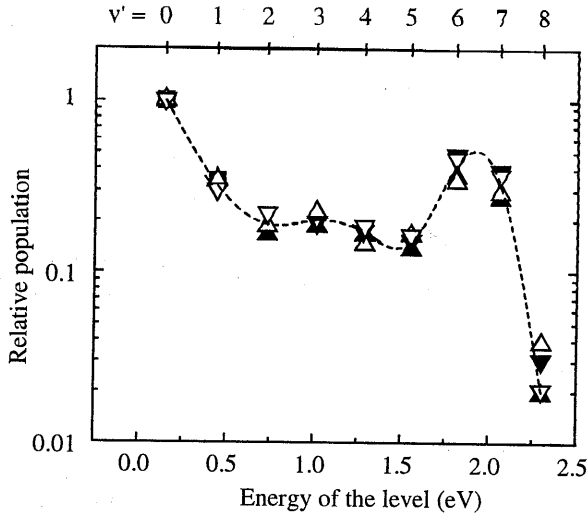


Figure 6.3: Vibrational distribution of $N_2^+(B^2\Sigma_u^+)$ determined from different bands of the first negative system. The symbols indicate the band from which the densities are determined, (∇) $\Delta v = -2$, (\blacktriangledown) $\Delta v = -1$, (\blacksquare) $\Delta v = 0$, (\blacktriangle) $\Delta v = +1$, and (\triangle) $\Delta v = +2$.

In this mechanism no distinction is made between the different excited states of the atoms and molecules and the rates should be considered averaged over all states present in the plasma. Note that Eqs. (6.4) and (6.5) are independent from Eq. (6.3). Equations (6.4) and (6.5) describe the general mechanism of recombination in the afterglow (see also Refs. [20] and [21]), whereas Eq. (6.3) is the proposed mechanism for population of the excited molecular ion. The (total) molecular ion density, $n_{N_2^+}$, is determined by the rate of production through charge exchange and destruction through dissociative recombination Eqs. (6.4) and (6.5):

$$n_{N_2^+} = \frac{n_{N^+} n_{N_2} k_{ce}}{n_e k_{dr}} \quad (6.6)$$

with n_e the electron density. Since quasi-neutrality must exist the electron density must be equal to the total ion density

$$n_e = n_{N^+} + n_{N_2^+} + n_{N_3^+} + \dots \quad (6.7)$$

Using the electron densities measured by the Langmuir probe it can be shown that the N_3^+ density is smaller than the N_2^+ by at least a factor 20 and may therefore be neglected in

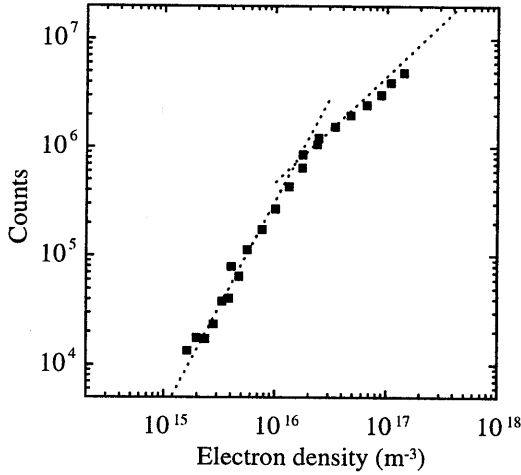


Figure 6.5: Emitted intensity of the first negative system as a function of electron density. The dashed lines show 1st and 2nd order dependence.

Eq. (6.7)* without significant loss of accuracy. Combining Eqs. (6.6) and (6.7) yields for the atomic ion density

$$n_{N^+} = \frac{n_e^2 k_{dr}}{n_e k_{dr} + n_{N_2} k_{ce}} \quad (6.8)$$

Using the approximate rate for charge exchange (the exact composition of molecular species is unknown) of $k_{ce} = 10^{-18} \text{ m}^3 \text{ s}^{-1}$ extrapolated from ref. [22] with an activation energy of 1.1 eV, and the rate of dissociative recombination $k_{dr} = 10^{-13} \text{ m}^3 \text{ s}^{-1}$ from ref. [23] it is possible to distinguish two regions. For large n_e ($n_e > n_{N_2} k_{ce}/k_{dr} \approx 10^{17} \text{ m}^{-3}$) the atomic ion density, n_{N^+} , equals the electron density. For $n_e < n_{N_2} k_{ce}/k_{dr}$, the atomic ion density becomes quadratically dependent on n_e according to Eq. (6.8) (assuming that the N_2 density is constant). This is consistent with the observed intensity from the first negative system (Fig. 6.5), although the transition from linear to higher order occurs at a slightly lower electron density than estimated above. The molecular ion density, $n_{N_2^+}$, on the other hand depends linearly on the electron density for low n_e and becomes constant at high n_e , according to Eqs. (6.6) and (6.7). Population of the $N_2^+(B^2\Sigma_u^+)$ state through V-E exchange between

* The complete balance for the N_3^+ density is outside the scope of this investigation. The density can be calculated from the rate coefficients given in Ref. [4] and will be discussed in more detail in Chapter 7.

vibrationally excited molecules and molecular ions in the ground state would in first approximation be proportional to the molecular ion density (the density of vibrationally excited molecules does not depend directly on the electron or ion density, since it is formed mainly by V-V exchange among molecules), contrary to the observed dependence of emission on n_e in Fig. 6.5.

6.3 Conclusions

Spectroscopic investigation of the first negative system of nitrogen shows overpopulation of the vibrational levels 6 and 7 of $N_2^+(B^2\Sigma_u^+)$. Selective excitation of these levels is explained by a charge exchange reaction between atomic ions in the ground state and metastable molecules in the $N_2(A^3\Sigma_u^+)$ state. The emitted intensity of the first negative system is shown to be linear with n_e for $n_e > 2 \times 10^{16} \text{ m}^{-3}$, a higher order dependence exists below this value. This is consistent with population of $N_2^+(B^2\Sigma_u^+)$ by atomic ions, N^+ . Population of $N_2^+(B^2\Sigma_u^+)$ by V-E exchange between vibrationally excited neutral molecules and ground state molecular ions can neither explain the selective population of vibrational levels 6 and 7 in the $N_2^+(B^2\Sigma_u^+)$ state, nor the observed dependence of emitted intensity on the electron density.

The observations made show a new mechanism for charge exchange that may have a significant influence on the ion densities and recombination in the remote arc generated plasma in nitrogen. This influence will be investigated in Chapter 7. Furthermore, it is shown that active (meta-)stable neutral particles are present in the downstream nitrogen plasma. Besides the influence on gas phase kinetics demonstrated here and in Chapter 7, these particles could play an important role in surface processes.

References

- 1 J. Kaplan, *Phys. Rev.* **54**, 176 (1938).
- 2 H. Coitout, G. Cernogora, and L. Magne, *J. Physique III* **5**, 203 (1995).
- 3 P.A. Sá, and J. Loureiro, *J. Phys. D: Appl. Phys* **30**, 2320 (1997).
- 4 V. Guerra, and J. Loureiro, *Plasma Sources Sci Technol.* **6**, 361 (1997).
- 5 G. Cernogora, C.M. Ferreira, L. Hochard, M. Touzeau, and J. Loureiro, *J. Phys. B: At. Mol. Phys.* **17**, 4429 (1984).
- 6 J. Loureiro, C.M. Ferreira, M. Capitelli, C. Gorse, and M. Cacciatore, *J. Phys. D: Appl. Phys.* **23**, 1371 (1990).
- 7 G.E. Beale, Jr., and H.P. Broida, *J. Chem. Phys.* **31**, 1030 (1959).
- 8 H.H. Brömer, and F. Döbler, *Z. Physik* **185**, 278 (1965).
- 9 Sin-Li Chen, and J.M. Goodings, *J. Chem. Phys.* **50**, 4335 (1969).

- 10 see for example P. Supiot, O. Dessaux, and P. Goudmand, *J. Phys. D: Appl. Phys.* **28**, 1826 (1995).
- 11 M. Cacciatore, M. Capitelli, S. DeBenedictis, M. Dilonardo, and C. Gorse, in: *Nonequilibrium Vibrational Kinetics*, Ed. M. Capitelli, Springer Verlag Berlin, Germany (1986).
- 12 M. Capitelli, C. Gorse, and A. Ricard, *J. Phys. Lettres* **44**, L-251 (1983).
- 13 R.F.G. Meulenbroeks, R.A.H. Engeln, M.N.A. Beurskens, R.M.J. Paffen, M.C.M. van de Sanden, J.A.M. van der Mullen, and D.C. Schram, *Plasma Sources Sci. Technol.* **4**, 74 (1995).
- 14 M.C.M. van de Sanden, G.M. Janssen, J.M. de Regt, D.C. Schram, J.A.M. van der Mullen, and B. van der Sijde, *Rev. Sci. Instrum.* **63**, 3369 (1992).
- 15 M.C.M. van de Sanden, J.M. de Regt, and D.C. Schram, *Plasma Sources Sci. Technol.* **3**, 501 (1994).
- 16 R.J. Severens, G.J.H. Brussaard, M.C.M. van de Sanden, and D.C. Schram, *Appl. Phys. Lett.* **67**, 491 (1995).
- 17 J.W.A.M. Gielen, M.C.M. van de Sanden, and D.C. Schram, *Appl. Phys. Lett.* **69**, 152 (1996).
- 18 A. Lofthus, and P.H. Krupenie, *J. Phys. Chem. Ref. Data* **6**, 113 (1977).
- 19 E. Aldea, G. Dinescu, J.W.A.M. Gielen, M.C.M. van de Sanden, and D.C. Schram, *Procs. XIII ESCAMPIG, Poprad, Slovakia* **20 E**, eds. Lukác, Košinár, and Skalný, 239 (1996).
- 20 R.P. Dahiya, M.J. de Graaf, R.J. Severens, H. Swelsen, M.C.M. van de Sanden, and D.C. Schram, *Phys. Plasmas* **1**, 2086 (1994).
- 21 G.J.H. Brussaard, M.C.M. van de Sanden, and D.C. Schram, *Phys. Plasmas* **4**, 3077 (1997).
- 22 S.C. Brown, *Basic Data of Plasma Physics*, 2nd ed. MIT Press, Cambridge, MA, (1966).
- 23 J.B. Hasted, *Physics of Atomic Collisions*, 2nd ed., Butterworths, London (1972).

7 The Density of Ions and Metastable Molecules in the Nitrogen Plasma

7.1 Introduction

Nitrogen plasmas are among the most thoroughly investigated plasmas. Interest in excitation mechanisms of nitrogen was first raised by the aurora phenomenon. More recent interests in nitrogen plasmas and plasma-surface interaction comes from the study of re-entry of spacecraft into the earth's atmosphere (the typical orange glow around the heat shields is caused by excited nitrogen) and hypersonic transport [1]. The formation of excited molecules by plasma-surface interaction is believed to be important in the energy exchange between the plasma and the ceramic tiles of the spacecraft. Super- and hypersonic plasma jets are used for fundamental studies into such reactions.* Plasma processing with high intensity nitrogen plasmas is used for nitriding of materials such as titanium to form hard and wear resistant materials [2, 3]. These materials range from corrosion resistant bathroom taps to high-speed parts in rocket and jet engines. In the study of the use of nitrogen plasmas for all of these applications, it is important to create a plasma with a great degree of freedom in plasma composition. The remote arc generated plasma provides this ability. The composition of the particles in the plasma can be varied by different settings of the source, background pressure and/or application of a magnetic field. The energy of charged particles can be chosen independently by application of a substrate bias. For a good understanding of the influence of different particles on plasma-surface interactions it is, of course, necessary to obtain detailed knowledge of the densities and energy of different particles. In this chapter the behavior of ions in the downstream nitrogen plasma is investigated. In Chapter 5 it was shown that in an argon-nitrogen plasma recombination takes place. In Chapter 6 one of the mechanisms for the recombination in a nitrogen plasma has been identified involving the excited metastable $N_2(A^3\Sigma_u^+)$ molecule. Such metastable molecules play an important role in the chemistry of low-temperature nitrogen plasmas [4, 5, 6]. This chapter will show how the densities of the different ions and the metastable $N_2(A^3\Sigma_u^+)$ density may be obtained in the remote arc generated nitrogen plasma by solving the mass balances for each of the species. In this respect this chapter is an extension of the chemical kinetics studied in Chapter 6 and the flow and diffusion behavior of heavy particles studied in Chapter 4.

* Part of the current research has been done in an ongoing cooperation between the Eindhoven University of Technology and the Wright Paterson Air Force base in Dayton, OH, with a grant from the European Office of Aerospace Research and Development (EOARD contract number SPC-97-4082)

An overview of the relevant plasma settings is given in Table 7.1. The plasma flows from the nozzle in the positive z direction. In the nozzle the plasma expands supersonically into the vessel. After the shock it flows at subsonic velocities [7]. The subsonic part of the plasma is the topic of the current investigation. For a more complete description of the source and the supersonic expansion, see also Chapter 1 of this thesis. In the downstream part, particles emitted from the source diffuse in positive r direction towards the vessel wall. Particles formed at the wall can diffuse back into the plasma in negative r direction. Throughout this chapter cylindrical symmetry is assumed (see also Chapter 4).

7.2 Theory

7.2.1 General steady state mass balance

In the downstream plasma under investigation a steady supply of energetic particles (atoms, ions, electrons and molecules) flows into the vessel from the arc. Inside the vessel these particles react with each other and diffuse towards the wall and after reactions at the wall newly formed particles diffuse back into the plasma stream. At any position in the plasma, the flow from the arc, diffusion to and from the walls and reactions among the particles is balanced so that a steady state situation exists (on the time scale of the measurements). The relative importance of reactions and transport for each particle at a specific position depends on the flow velocity, diffusion constant, and rate for reactions with other particles. In general the steady state mass balance for the density n of each particle can be written as (see also Chapters 4-6)

$$\frac{dn}{dt} = -\bar{\nabla} \cdot (n\bar{v}_d) + \bar{\nabla} \cdot (D\bar{\nabla}n) + P - nR = 0 \quad (7.1)$$

with \bar{v}_d the drift velocity, D the diffusion coefficient, P the production of the particles, and R the reaction rate for the loss through volume reactions with other particles or radiative decay

N ₂ flow	1 slm
Arc current	45-75 A
Downstream ($z > 10$ cm):	
Chamber pressure	225 Pa
Electron density	$10^{15} - 10^{19} \text{ m}^{-3}$
Electron temperature	0.1 - 0.3 eV

in the case of excited particles.

7.2.2 Electrons.

There is a flow of electrons and ions coming from the arc and (ambipolar) diffusion towards the walls. Since electron temperatures are low (< 0.5 eV), there is no significant ionization by electron impact inside the low pressure chamber. As was discussed in the previous two chapters, volume loss of ions is caused by dissociative recombination of molecular ions, N_2^+ , with electrons:



With these considerations the particle balance for the electrons is written as:

$$-\bar{\nabla} \cdot (n_e \bar{v}_d) + (\bar{\nabla} \cdot D_a \bar{\nabla} n_e) - n_e n_{N_2^+} k_{dr} = 0 \quad (7.3)$$

with n_e the electron density, \bar{v}_d the drift velocity, D_a the ambipolar diffusion coefficient (see for example [8, 9]), $n_{N_2^+}$ the density of the molecular ions and k_{dr} the rate coefficient for dissociative recombination [10]. In the downstream plasma, the flow is mainly in the positive z direction, away from the nozzle, as was extensively discussed in Chapter 4. Diffusion is mainly in the radial direction. In Fig. 7.2(b) in the experimental section of this chapter it will be shown that there is no significant radial dependence of the electron temperature. The ambipolar diffusion coefficient, D_a , consequently has no radial dependence either (see Chapter 4). With cylindrical symmetry, Eq. (7.3) is written in terms of z and r as:

$$-v_d \frac{\partial n_e}{\partial z} + D_a \frac{1}{r} \frac{\partial}{\partial r} \left(r \frac{\partial n_e}{\partial r} \right) - n_e n_{N_2^+} k_{dr} = 0 \quad (7.4)$$

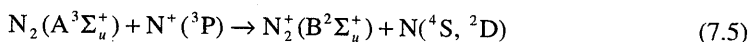
In this simplification the decrease in drift velocity with increased distance from the nozzle is neglected. Although it was shown in Chapter 4 that this decrease in drift velocity can have significant influence on the diffusion in the downstream plasma, this influence will be less when significant recombination is taking place, as is the case in the present investigation.

Practically all of the ions emitted from the thermal arc source will be atomic ions, since molecular ions will have a very short lifetime at the density and temperature in the arc plasma. What will therefore be most important for the ion density distribution and the electron density in general is the charge exchange mechanism between the atomic ions and neutral molecules (see Eq. (7.2)). In Chapter 6 it was shown that at least part of this charge exchange is a charge exchange between ground state atomic ions and metastable molecules in the $N_2(A^3\Sigma_u^+)$ state, leading to the excited molecular ion in the $N_2^+(B^2\Sigma_u^+)$ state. For an understanding of the ion density distribution in the plasma it is therefore necessary to investigate the particle balances for the atomic ions, the excited molecular ions $N_2^+(B^2\Sigma_u^+)$ and the ground state molecular ions $N_2^+(X^2\Sigma_g^+)$. Note that for the recombination of electrons, there is no difference between the

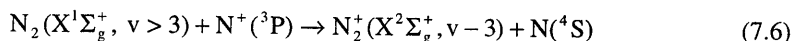
excited and ground state molecular ions. That is the reason why in Eqs. (7.3) and (7.4) no distinction was made between these species. The total molecular ion density $n_{N_2^+}$ is the sum over all species of N_2^+ .

7.2.3 Atomic ions N^+ .

In the particle balance of the atomic ion we will consider two mechanisms for charge exchange. The first mechanism is the one described in Chapter 6, exchange between ground state atomic ions and metastable molecules in the $N_2(A^3\Sigma_u^+)$ state:



The vibrational state of the resulting molecular ion depends on the vibrational state of the initial metastable molecule and on the specific ground state of the resulting N atom. The second mechanism is between ground state atomic ions and vibrationally excited molecules. The difference in ionization energy between N and N^+ must in this case be carried as vibrational energy by the molecule. The reaction is:



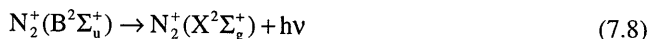
Based on these two mechanisms and the transport of particles by drift and diffusion, the particle balance for the atomic ions becomes

$$-v_d \frac{\partial n_{N^+}}{\partial z} + D_a \frac{1}{r} \frac{\partial}{\partial r} \left(r \frac{\partial}{\partial r} n_{N^+} \right) - n_{N^+} n_{N_2(A)} k_{ce1} - n_{N^+} n_{N_2(X, v>3)} k_{ce2} = 0 \quad (7.7)$$

with n_{N^+} the atomic ion density, $n_{N_2(A)}$ the density of the metastable molecules, k_{ce1} the rate coefficient for the reaction given in Eq. (7.5), $n_{N_2(X, v>3)}$ the density of vibrationally excited molecules, and k_{ce2} the rate coefficient for the charge exchange reaction Eq. (7.6).

7.2.4 Excited molecular ions $N_2^+(B^2\Sigma_u^+)$.

The excited molecular ion, $N_2^+(B^2\Sigma_u^+)$, formed in the reaction Eq. (7.5) will undergo radiative decay into its ground state $N_2^+(X^2\Sigma_g^+)$:



The light emitted is the so-called First Negative System (FNS) of nitrogen, studied in detail in Chapter 6. The lifetime of $N_2^+(B^2\Sigma_u^+)$ is of the order 10^{-8} s [11], that is, much shorter than the typical transport times (which will be shown in the next section to be larger than 10^{-4} s). As a result, the first two terms of the particle balance Eq. (7.1) are negligible. The specie is said to be in Quasi Steady State throughout the plasma. The production by the reaction Eq. (7.5) is balanced (locally) by the destruction through radiative decay, Eq. (7.8):

$$n_{N^+} n_{N_2(A)} k_{ce1} - n_{N_2^+(B)} A_{B \rightarrow X} = 0 \quad (7.9)$$

with $n_{N_2^+(B)}$ the density of the excited molecular ion, and $A_{B \rightarrow X}$ the transition probability for the radiative decay of Eq. (7.8).

7.2.5 The ground state molecular ions, $N_2^+(X^2\Sigma_g^+)$.

The final particle balance in the description of the ionic species in the nitrogen plasma is the balance for the ground state molecular ions, $N_2^+(X^2\Sigma_g^+)$. Apart from the transport terms, the production of the ground state molecular ion is by charge exchange of atomic ions with vibrationally excited molecules in the ground state (Eq. (7.6)) and radiative decay of excited molecular ions (Eq. (7.8)). The destruction of molecular ions is by dissociative recombination (Eq. (7.2)). The balance is:

$$-v_d \frac{\partial n_{N_2^+(X)}}{\partial z} + D_a \frac{1}{r} \frac{\partial}{\partial r} \left(r \frac{\partial}{\partial r} n_{N_2^+(X)} \right) + n_{N^+} n_{N_2(X, \nu > 3)} k_{ce2} + n_{N_2^+(B)} A_{B \rightarrow X} - n_e n_{N_2^+(X)} k_{dr} = 0 \quad (7.10)$$

In general, the ambipolar diffusion coefficients, D_a , for diffusion of atomic and molecular ions are different. In the case of diffusion of electrons (Eq. (7.4)) the diffusion coefficient depends on the composition of the ions in the plasma. In the calculation of the mass balance, the diffusion always has to be compared to the recombination (both are loss terms in the mass balances). Diffusion is only important at very low electron density. It will be shown later that in those cases the molecular ion will be the most abundant ion in the plasma. In the present analysis, only the ambipolar diffusion coefficient of molecular ions is therefore needed.

The complete scheme of reactions involved in charge exchange and dissociative recombination in nitrogen is given in Table 7.2. The four balance equations (Eq. (7.4)) for the electrons, Eq. (7.7) for the atomic ions, Eq. (7.9) for the excited molecular ions, and Eq. (7.10)

Table 7.2: Reactions involved in the charge exchange and dissociative recombination

Reaction	Rate		Ref.
$N_2(A^3\Sigma_u^+) + N^+(^3P) \rightarrow N_2^+(B^2\Sigma_u^+) + N(^4S, ^2D)$	$10^{-16} \text{ m}^3 \text{ s}^{-1}$	k_{ce1}	[21]
$N_2(X^1\Sigma_g^+, \nu > 3) + N^+(^3P) \rightarrow N_2^+(X^2\Sigma_g^+, \nu - 3) + N(^4S)$	$10^{-16} \text{ m}^3 \text{ s}^{-1}$	k_{ce2}	[21]
$N_2^+(B^2\Sigma_u^+) \rightarrow N_2^+(X^2\Sigma_g^+) + h\nu$	10^8 s^{-1}	$A_{B \rightarrow X}$	[11]
$N_2^+ + e \rightarrow 2N$	$3 \times 10^{-13} \text{ m}^3 \text{ s}^{-1}$	k_{dr}	[10]

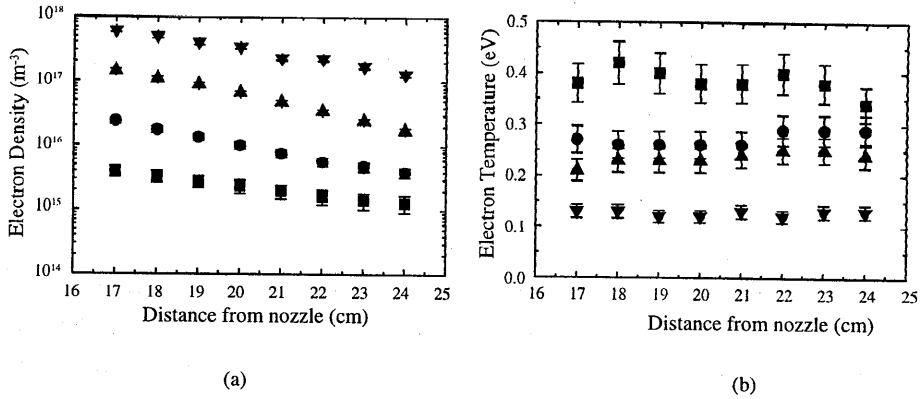


Figure 7.1: Electron density (a), and temperature (b) as a function of distance from the nozzle at different settings of the current through the arc: ■ 45 A, ● 65 A, ▲ 75 A, and ▼ 75 A after 1 hour.

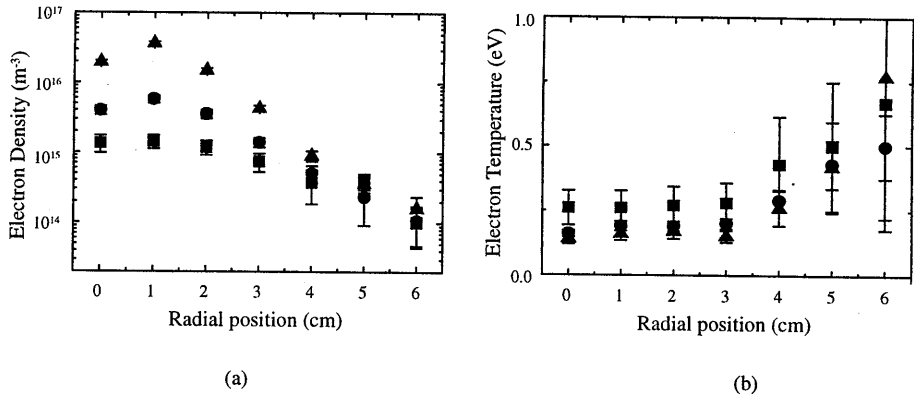


Figure 7.2: Electron density (a) and temperature (b) as a function of radial position at 24 cm from the nozzle: ■ 45 A, ● 65 A, ▲ 75 A.

for the ground state molecular ions) in combination with measurements of the electron density and the light emitted in the first negative system (Eq. (7.8)) enable the determination of the ion densities and metastable $\text{N}_2(\text{A}^3\Sigma_u^+)$ density in the plasma.

7.3 Experimental Results

Electron densities were measured using a single planar Langmuir probe. The electron densities are shown in Fig. 7.1(a) as a function of distance from the nozzle at different settings of the arc current. Two sets of measurements were taken at maximum current (75 A), the second of which was taken after the plasma had been running for one hour. The results show that the density has increased significantly during that time. A possible explanation will be discussed

later, in section 7.4. In Fig. 7.1(b) the electron temperatures corresponding to the measurements of Fig. 7.1(a) are shown. In Fig. 7.2 radial profiles of the electron density and temperature are shown at 24 cm downstream from the nozzle.

Estimation of the N_2^+ density from the electron density measurements

Using the data given in Figs. 7.1 and 7.2 and the particle balance for the electrons (Eq. (7.4)), it is possible to make an estimate of the N_2^+ density. The first term of Eq. (7.4), $-v_d \frac{\partial n_e}{\partial z}$, is found by fitting an exponential decay through the points of Fig. 7.1(a) and taking the derivative of the fit. The velocity (see Chapter 4) is taken to be constant at a value of 400 ± 50 m/s. The second term of Eq. (7.4), $D_a \frac{1}{r} \frac{\partial}{\partial r} \left(r \frac{\partial n_e}{\partial r} \right)$ is found after fitting a Gaussian profile (cf. Chapter 4) through the data of Fig. 7.2(a) and taking the second derivative with respect to r . The ambipolar diffusion coefficient, D_a , is given by [8]:

$$D_a = \left(1 + \frac{T_e}{T_i} \right) \frac{3.6 \times 10^{30} (kT_i)^{\frac{1}{2}}}{n_a} \quad (7.11)$$

with n_a the density of the neutral (N_2) particles. The N_2^+ density is found by rewriting Eq. (7.4) to

$$n_{N_2^+} = \frac{\left\{ -v_d \frac{\partial n_e}{\partial z} \right\} + \left\{ D_a \frac{1}{r} \frac{\partial}{\partial r} r \frac{\partial n_e}{\partial r} \right\}}{n_e k_{dr}} \quad (7.12)$$

The value of the rate for dissociative recombination, k_{dr} , is taken [10] to be 3×10^{-13} m³/s. The resulting N_2^+ density is shown in Fig. 7.3 as a function of electron density. The solid diagonal line in Fig. 7.3 indicates the line $n_i = n_e$. Since quasi neutrality must be sustained, the N_2^+ density can never exceed the electron density. The drawn line is therefore an upper limit for the molecular ion density. The uncertainty resulting from the measurements of v_d , T_e , n_e and its derivatives is shown as error bars on the data points of Fig. 7.3. Apart from the uncertainties in the measurements there are also uncertainties in the ambipolar diffusion coefficient and the rate coefficient for dissociative recombination [9], leading to systematical errors in the N_2^+ density determined by Eq. (7.12). This explains why the N_2^+ density seems to exceed the electron density at low electron density.

The largest systematic error in the calculations leading to the results of Fig. 7.3 is caused by the uncertainty in the rate coefficient for dissociative recombination, k_{dr} . This uncertainty is estimated to be approximately a factor of 3. The error is primarily a result of the limited knowledge of the temperature dependence of the rate coefficient. Another possibility is the presence of larger ions, specifically N_3^+ , whose presence will effectively lead to a larger rate of dissociative recombination. This effect will be discussed later in this chapter. Taking into

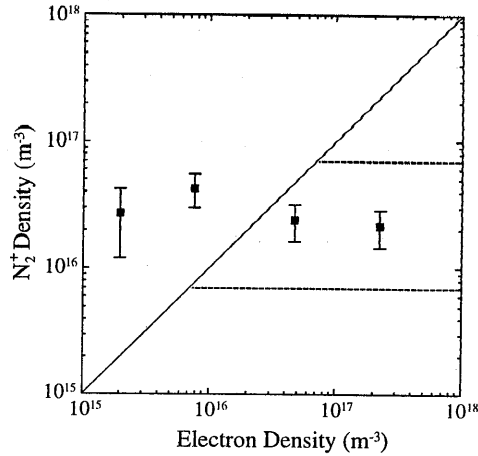


Figure 7.3: Estimated N_2^+ density as a function of electron density.

account the uncertainty in the rate coefficient for dissociative recombination, an interval was calculated for the possible values of the density of N_2^+ . The interval is shown in Fig. 7.3 by the dashed lines.

There is also an uncertainty in the ambipolar diffusion. This is mainly due to lack of knowledge of the ion distribution. N^+ and N_2^+ have different diffusion coefficients, not only because of the difference in mass, but also because only N_2^+ will undergo resonant charge exchange with the N_2 in the background. In these calculations the diffusion coefficient of N_2^+ was used, with a gas temperature of 10^3 K. This means that the real diffusion coefficient may be slightly higher, leading to a lower N_2^+ density. In the present calculations the effect of diffusion turns out to be at least an order of magnitude lower than the other transport term ($v_d \frac{\partial n_e}{\partial z}$) and may therefore be neglected.

Determination of the N_2^+ density from the electron density and spectroscopic measurements

There is another way of determining the molecular ion density by using data from the balances for excited molecular ions (Eq. (7.9)) and ground state molecular ions (Eq. (7.10)). If the transport terms in Eq. (7.10) are neglected Eq. (7.10) can be rewritten to

$$n_{N^+} n_{N_2(A)} k_{ce1} \left(\frac{n_{N_2(X,v)} k_{ce2}}{n_{N_2(A)} k_{ce1}} + 1 \right) = n_{N_2^+(X)} n_e k_{dr} \quad (7.13)$$

Defining a parameter ξ as

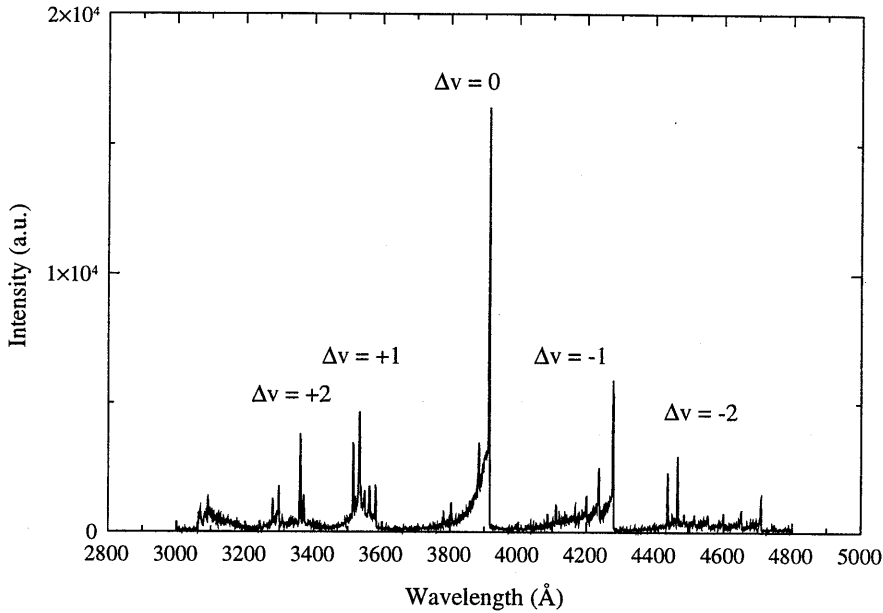


Figure 7.4: Spectrum of the First Negative System of nitrogen: $N_2^+(B^2\Sigma_u^+) \rightarrow N_2^+(X^2\Sigma_g^+)$

$$\xi \equiv \frac{n_{N_2(A)} k_{ce1}}{n_{N_2(A)} k_{ce1} + n_{N_2(X,v)} k_{ce2}} \quad (7.14)$$

ξ represents the relative importance of charge exchange involving metastable molecules (the process described in Chapter 6) compared to the total charge exchange (Eqs. (7.5) plus (7.6)). Combining Eq. (7.13) and Eq. (7.14) with Eq. (7.9) yields the ground state molecular ion density as

$$n_{N_2^+(X)} = \frac{n_{N_2^+(B)} A_{B \rightarrow X}}{n_e k_{dr}} \xi^{-1} \quad (7.15)$$

The emitted light from the radiative decay of $N_2^+(B^2\Sigma_u^+)$ (First Negative System) is measured with optical emission spectroscopy. Equation (7.15) shows that the molecular ion density will be proportional to the emitted light in the first negative system divided by the electron density. It is assumed here that the parameter ξ is not directly dependent on the electron density.

In Fig. 7.4 the spectrum of the First Negative System is shown. The spectrum has been discussed in detail in Chapter 6. Since it is not possible with the setup used to measure the whole spectrum instantly, the intensity of the light of the (0,0) transition at 391.4 nm (the most prominent peak in the spectrum) is taken as a measure of the total intensity of emitted light from the plasma. To determine whether this is a reasonable simplification, radial scans were

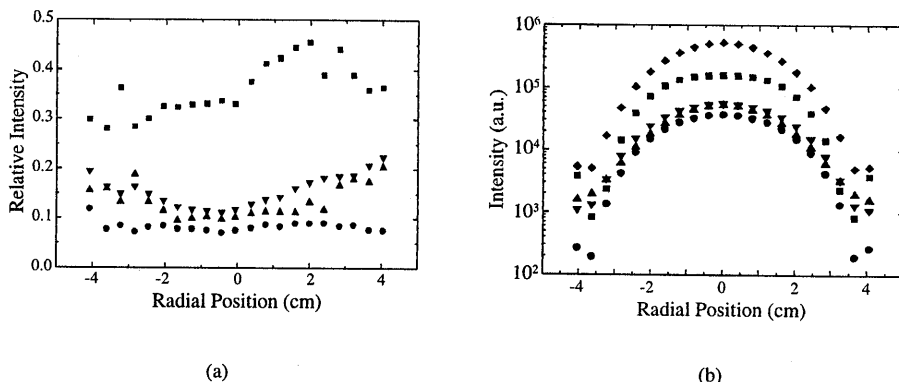


Figure 7.5: Intensity of the bandheads (a) relative to the intensity of the (0,0) transition; and (b) as a function of radial distance. The symbols in both figures are: ● $\Delta v = -2$, ■ $\Delta v = -1$, ◆ $\Delta v = 0$, ▲ $\Delta v = +1$, ▼ $\Delta v = +2$.

made of the bandheads of the four other bands visible in the spectrum ($\Delta v = -2, -1, 1, 2$) and divided by the intensity of the (0,0) bandhead. The result is shown in Fig. 7.5(a). The relative intensity of all bandheads remains constant within approximately 25%. The optical emission spectroscopy integrates the emitted light over the line of sight. To determine the local emission, lateral scans are converted to radial profiles with Abel inversion [12]. The local density (still in arbitrary units) of the upper level of the bandheads of the five bands visible in the spectrum is shown in Fig. 7.5(b) as a function of radial position. From Fig. 7.5 it may be concluded that the local intensity of the (0,0) transition after Abel inversion, $I_{(0,0)}$, is proportional to the density of $N_2^+(B^2\Sigma_u^+)$ and we may write

$$I_{(0,0)} = n_{N_2^+(B)} A_{B \rightarrow X} \cdot C_c \quad (7.16)$$

with C_c a calibration constant that depends on the response of the emission spectroscopy setup.

It is possible to determine the absolute density of the molecular ion (under the assumptions that diffusion may be neglected and ξ is not directly dependent on the electron density). Quasi neutrality gives

$$n_e = n_{N^+} + n_{N_2^+} \quad (7.17)$$

The assumption has been made here that larger molecules (N_3^+, N_4^+, \dots) are not present in significant numbers. This assumption will be discussed later. Since the radiative decay of the excited molecular ion is much faster (10^{-8} s) than the dissociative recombination ($10^{-3} - 10^{-6}$ s for electron densities between 10^{15} and 10^{18} m^{-3}) the density of molecular ions, $n_{N_2^+}$, will be

equal to the density of ground state molecular ions $n_{N_2^+(X)}$. Combining Eq. (7.17) with Eq. (7.13) results in

$$n_{N^+} n_{N_2(A)} k_{ce1} \left(\frac{n_{N_2(X,v)} k_{ce2}}{n_{N_2(A)} k_{ce1}} + 1 \right) = (n_e - n_{N^+}) n_e k_{dr} \quad (7.18)$$

so that the atomic ion density, n_{N^+} , is found as

$$n_{N^+} = \frac{n_e^2 k_{dr}}{(n_{N_2(A)} k_{ce1} + n_{N_2(X,v)} k_{ce2} + n_e k_{dr})} \quad (7.19)$$

This equation shows that at high electron density, $n_e > (n_{N_2(A)} k_{ce1} + n_{N_2(X,v)} k_{ce2}) / k_{dr}$, the atomic ion density equals the electron density. At these high densities the dissociative recombination is fast, so that charge exchange (Eqs. (7.5) and (7.6)) is the limiting step in the reaction mechanism for the loss of ions. Equation (7.19) also shows that at low electron density, $n_e < (n_{N_2(A)} k_{ce1} + n_{N_2(X,v)} k_{ce2}) / k_{dr}$, the atomic ion density is proportional to the electron density squared (this was shown explicitly in Fig. 6.5 of Chapter 6).[†] Using Eqs. (7.9), (7.16) and (7.17) the measured intensity, $I_{(0,0)}$, can be written as

$$I_{(0,0)} = \frac{n_e^2 k_{dr} \cdot n_{N_2(A)} k_{ce1}}{n_{N_2(A)} k_{ce1} + n_{N_2(X,v)} k_{ce2} + n_e k_{dr}} C_c \quad (7.20)$$

As with the atomic ion density, for low electron density this intensity will be proportional to the electron density squared. In a more formal form:

$$\lim_{n_e \rightarrow 0} \frac{I_{(0,0)}}{n_e^2} = \xi \cdot k_{dr} \cdot C_c \quad (7.21)$$

The parameter $I_{(0,0)} / n_e^2$ is plotted in Fig. 7.6. At electron densities below $2 \times 10^{16} \text{ m}^{-3}$ the value of $I_{(0,0)} / n_e^2$ tends to a limit of $3.3 \times 10^{-28} \text{ m}^5 \text{ s}^{-1}$ (although the dimension here is not particularly interesting). Taking into account the uncertainties in the measurements we find for the constant $\xi \cdot k_{dr} \cdot C_c$:

$$2 \times 10^{-28} < \xi \cdot k_{dr} \cdot C_c < 6 \times 10^{-28} \quad [\text{m}^5 \text{ s}^{-1}] \quad (7.22)$$

Combining Eqs. (7.15) and (7.16) the molecular ion density is determined from measured data by

$$n_{N_2^+} = \frac{I_{(0,0)}}{n_e} (\xi \cdot k_{dr} \cdot C_c)^{-1} \quad (7.23)$$

[†] Strictly speaking, we have made the new assumption here that $n_{N_2(A)} k_{ce1}$ does not depend on n_e . However, this is not a much stronger assumption than what was already assumed, i.e. that ξ is independent of n_e .

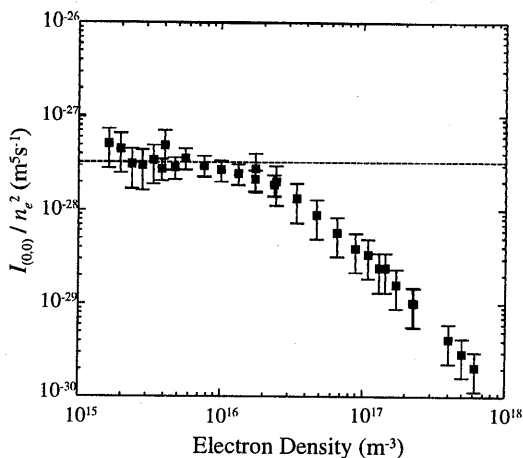


Figure 7.6: Emission of the (0,0) transition divided by the electron density squared, as a function of electron density. The dashed line indicates the limit to which this parameter tends at low electron density.

Figure 7.7 shows the molecular ion density determined in this way. The error bars show the uncertainty in the determination of $I_{(0,0)}$ and n_e . The dashed lines indicate the systematic error introduced by the determination of the constant $\xi \cdot k_{dr} \cdot C_c$.

It may be interesting to note that the absolute molecular ion density is determined without the necessity to know any rate constants or the efficiency of the emission spectroscopy setup. The densities compare well with the densities estimated in Fig. 7.3. The latter were estimated on the basis of rate constants and the velocity measurement of Chapter 4 (beside the Langmuir probe measurements, which are used in both methods).

The influence of formation of larger molecular ions

By setting the electron density equal to the sum of the N^+ and N_2^+ the presence of larger molecular ions was neglected. This may not be entirely justified. N_3^+ is normally formed by the reaction [13, 14]



with M the third particle to account for the excess energy (≈ 1 eV). The rate coefficient for this reaction is (at 10^3 K) $2 \times 10^{-42} \text{ m}^6 \text{ s}^{-1}$ according to ref. [13]. This process must compete with the charge exchange reactions Eqs. (7.5) and (7.6). Using a neutral density of 10^{22} m^{-3} , an estimated rate for the charge exchanges of Eqs. (7.5) and (7.6) of $10^{-16} \text{ m}^3 \text{ s}^{-1}$ and density for

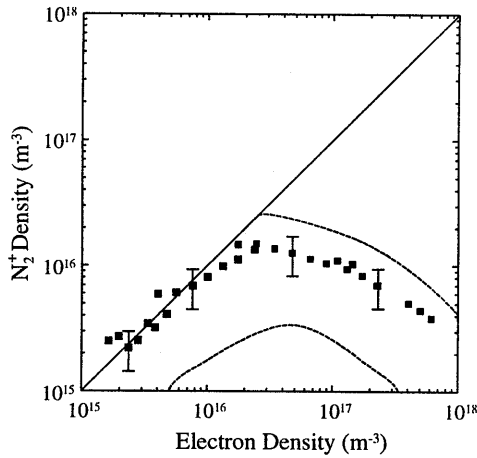


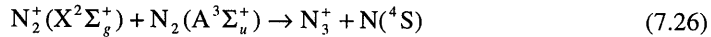
Figure 7.7: Molecular ion density as a function of electron density.

$N_2(A^3\Sigma_u^+)$ and $N_2(X^1\Sigma_g^+, v > 3)$ of 10^{20} m^{-3} (these values will be discussed in detail later), the formation of N_3^+ through reaction Eq. (7.24) will be at least an order of magnitude slower than the charge exchange leading to N_2^+ and may therefore be neglected.

Another possibility for the formation of N_3^+ is the following reaction [15]:



This reaction requires 6.5 eV and will therefore normally be insignificant in low temperature plasmas. However, the metastable $N_2(A^3\Sigma_u^+)$ has just over 6 eV in electronic excitation. It seems possible that in this plasma with ample evidence for the presence of the metastable molecules N_3^+ may be formed through the more specific reaction



N_3^+ will be lost through dissociative recombination with an electron. The rate for dissociative recombination of N_3^+ is approximately 3 times larger than k_{dr} for N_2^+ [13]. The effect of this process is an effective increase in the rate of dissociative recombination, k_{dr} , and the transformation of part of the ground state molecular ions to N_3^+ . This has some effect on the determination of the N_2^+ density leading to the results of Fig. 7.7. Since the rate of recombination has no influence, and the emission is not affected by the formation of N_3^+ the absolute values found for the molecular ion density will remain the same. The only effect is at low electron density, where reaction Eq. (7.26) becomes faster than the dissociative recombination Eq. (7.2). To estimate the electron density at which the rate of both processes becomes comparable we must estimate the rate coefficient for reaction Eq. (7.26). Since the

reaction is energetically nearly resonant, we use the maximum in the cross section for charge exchange between N^+ and N_2 of 10^{-19} m^2 [16, 17]. This estimate should be considered an upper limit since Eq. (7.26) represents an ion transfer rather than electron transfer reaction. This leads to a rate coefficient of $10^{-16} \text{ m}^3 \text{ s}^{-1}$. With a density of $N_2(A^3\Sigma_u^+)$ of 10^{20} m^{-3} (see below), at electron densities lower than $3 \times 10^{16} \text{ m}^{-3}$ a significant portion of molecular ions may be N_3^+ . Figure 7.7 in this case gives the sum of the molecular ion densities of $N_2^+ + N_3^+$. For the estimation of molecular ions leading to Fig. 7.3 there is an additional effect. Since the rate of dissociative recombination of N_3^+ is larger than for N_2^+ , the values at low electron density in Fig. 7.3 will be lower thus bringing them closer to the line $n_i = n_e$.

At low electron densities and/or high pressure N_4^+ may be formed through the reaction [14, 13]



with M the third particle to account for the excess energy. The rate coefficient for this reaction is $1.1 \times 10^{-41} \text{ m}^6 \text{ s}^{-1}$ [14, 18]. The rate of formation of N_4^+ must also compete with the dissociative recombination. With neutral gas (N_2) density of 10^{22} m^3 the rate of formation of N_4^+ becomes comparable to the rate of dissociative recombination at electron densities below $3 \times 10^{15} \text{ m}^{-3}$. Within the measurements performed here, the formation of N_4^+ may be neglected without loss of accuracy. The formation of even larger molecules is more complex and they will therefore not be formed under the present conditions.

The relative importance of charge exchange between atomic ions and metastable molecules.

Some information on the constant $\xi \cdot k_{dr} \cdot C_c$ may be obtained by calibrating the optical emission spectroscopy setup. The calibration was performed using a tungsten ribbon lamp [19, 20]. The spectrum of the first negative system was integrated over all five visible bands, from 3200 to 4750 Å. The calibration constant C_c was found to be $(7 \pm 2) \times 10^{-15} \text{ m}^2$. With the rate of dissociative recombination of $k_{dr} = 3 \times 10^{-13} \text{ m}^3 \text{ s}^{-1}$ the value of ξ is found to be 0.15. When the uncertainties in the measurements (the uncertainty in k_{dr} is unknown) are included, we find $0.07 < \xi < 0.4$. This means that between 7% and 40% of the charge exchange occurring in the plasma leads to the formation of excited molecular ions, $N_2^+(B^2\Sigma_u^+)$. The rest of the charge exchange reactions (between 60 and 93%) will involve vibrationally excited ground-state molecules $N_2(X^1\Sigma_g^+, v > 3)$. The density of these molecules needed to account for these reactions will be discussed later.

The density of the metastable $N_2(A^3\Sigma_u^+)$.

The rate for charge exchange between atomic ions and metastable molecules, k_{ce1} , is unknown. As an estimate we will use the cross section for charge transfer between nitrogen

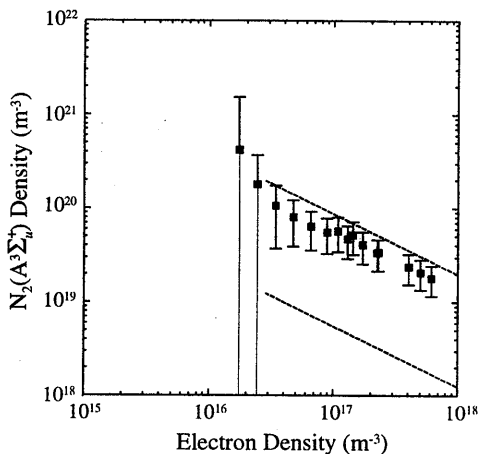


Figure 7.8: Density of the metastable molecule $N_2(A^3\Sigma_u^+)$.

ions and ground state molecular nitrogen at low energy, just above the threshold. This cross section is found in ref. [21] to be $5 \times 10^{-20} \text{ m}^2$. Since the charge exchange with the metastable molecule is a resonant process, this cross section must be regarded as a lower limit. With this cross section and ion temperatures between 0.1 and 0.5 eV, the rate of charge exchange, k_{ce1} , is estimated to be $10^{-16} \text{ m}^3 \text{ s}^{-1}$. The atomic ion density, n_{N^+} , is obtained by subtracting the molecular ion density from the electron density (Eq. (7.17) and Fig. 7.7). With Eqs. (7.9) and (7.16) the density of the metastable molecule is

$$n_{N_2(A)} = \frac{I_{(0,0)} C_c^{-1}}{n_{N^+} k_{ce1}} \quad (7.28)$$

The calculated density of $N_2(A^3\Sigma_u^+)$ is plotted in Fig. 7.9. At low electron densities the error in the determination of n_{N^+} becomes larger than the density. The calculation of $n_{N_2(A)}$ in this manner, therefore, only yields significant results at high electron density. Systematic errors are caused by the uncertainty in the determination of C_c ($\pm 30\%$) and the rate for charge exchange, k_{ce1} , which could be an order of magnitude higher. The dashed lines in Fig. 7.8 show the interval in which the density may vary with these uncertainties.

Destruction of $N_2(A^3\Sigma_u^+)$ is mainly through energy pooling reactions in which two $N_2(A^3\Sigma_u^+)$ molecules form one excited $N_2(B^3\Pi_g)$ or $N_2(C^3\Pi_u)$ and one ground-state $N_2(X^2\Sigma_g^+)$ [5, 22]. The rate these reactions is approximately $2 \times 10^{-16} \text{ m}^3 \text{ s}^{-1}$. With the densities found in Fig. 7.8, the lifetime of $N_2(A^3\Sigma_u^+)$ is approximately 10^{-3} - 10^{-4} s, which is also the typical time needed to traverse the vessel. This means that even if more $N_2(A^3\Sigma_u^+)$ is produced, the density

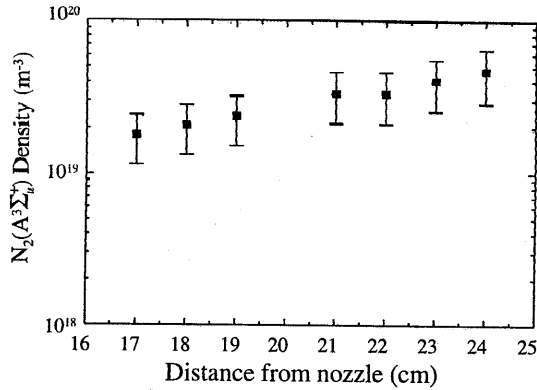


Figure 7.9: $N_2(A^3\Sigma_u^+)$ density as a function of distance from the arc.

at the center of the plasma and 20 cm downstream from the source, is not expected to exceed 10^{19} - $10^{20} m^{-3}$.

The densities found in Fig. 7.8 exceed typical values measured in glow discharges by approximately 1 order of magnitude [23].

It was assumed earlier that the density of $N_2(A^3\Sigma_u^+)$ is independent of n_e . In Fig. 7.8 it is shown that this is not completely true. The decrease in $n_{N_2(A)}$ at high n_e is most likely due to the depletion of $N_2(A^3\Sigma_u^+)$ by the charge exchange with atomic ions. This can only be the case if the density of $N_2(A^3\Sigma_u^+)$ is of the same order as the atomic ion density and a significant part of the charge exchange involves a metastable molecule. As an upper limit, in the case that $\xi = 1$, the loss of an electron due to charge exchange of an atomic ion followed by dissociative recombination, will cause an equal loss in absolute density of metastable molecules. Therefore, the loss in the density of $N_2(A^3\Sigma_u^+)$ is only significant if this density is of the same order as the atomic ion density.

There may be some effect of the decrease of $n_{N_2(A)}$ at high n_e on the N_2^+ density shown in Fig. 7.7. If, with $n_{N_2(A)}$, the value of ξ decreases, the N_2^+ density at high n_e has been underestimated so that the decrease of $n_{N_2^+}$ with increasing n_e will be less.

The apparent decrease in the $N_2(A^3\Sigma_u^+)$ density with increasing electron density gives insight in another very interesting matter, the origin of the metastable molecule. There are basically two possibilities. The first one is the formation of $N_2(A^3\Sigma_g^+)$ on the walls of the vessel by association of two $N(^4S)$ atoms; the other possibility is formation inside the arc. In Fig. 7.9 the density of $N_2(A^3\Sigma_u^+)$, determined from Eq. (7.24) is plotted as a function of distance from the

arc. If the $N_2(A^3\Sigma_u^+)$ were formed inside the arc one would expect a decrease rather than an increase of the density with increasing distance from the arc. It is therefore more likely that the $N_2(A^3\Sigma_u^+)$ is formed outside the arc, on the vessel walls.

The density of vibrationally excited molecules $N_2(X^1\Sigma_g^+, v > 3)$.

The density of vibrationally excited ground state molecules, $N_2(X^1\Sigma_g^+, v > 3)$, can be estimated from the value found for ξ . Using the cross section for charge exchange between atomic ions and ground state molecules [21], just above the threshold, the rate coefficient is found to be $k_{ce2} = 10^{-16} \text{ m}^3 \text{ s}^{-1}$. With $\xi = 0.15$ and $n_{N_2(A)} \approx 5 \times 10^{19} \text{ m}^{-3}$, Eq. (7.15) gives the density of $N_2(X^1\Sigma_g^+, v > 3)$ as $n_{N_2(X,v>3)} \approx 3 \times 10^{20} \text{ m}^{-3}$. The total N_2 density (using a gas temperature of 10^3 K) is 10^{22} m^{-3} . To obtain the density of $3 \times 10^{20} \text{ m}^{-3}$ the vibrational temperature needs to be 3000 K. The electron density in the plasma is found to be lower, so that a slight overpopulation of the vibrational distribution with respect to thermal equilibrium must exist.

7.4 Conclusions

The main loss mechanism for the electrons and ions in the expanding nitrogen plasma is charge exchange followed by dissociative recombination. Using the axial electron density profile and the velocity, it was shown to be possible to estimate the molecular ion density in the plasma. Part of this charge exchange involves charge exchange between atomic ions, N^+ , and metastable molecules, $N_2(A^3\Sigma_u^+)$, leading to excited molecular ions, $N_2^+(B^2\Sigma_u^+)$. Using the emission from the radiative decay of $N_2^+(B^2\Sigma_u^+)$ as a function of electron density, the molecular ion density can be calculated. The two methods for the determination of the molecular ion density compare well and yield values for the density of N_2^+ between 10^{15} and $3 \times 10^{16} \text{ m}^{-3}$. The presence of N_3^+ may lead to a slight overestimation of N_2^+ at low electron densities. From the emission of $N_2^+(B^2\Sigma_u^+)$ as a function of electron density it has been determined that between 7 and 40% of the charge exchange reactions will lead to the excited molecular ion, $N_2^+(B^2\Sigma_u^+)$.

The density of the metastable molecule has been calculated and is found to be 10^{19} - 10^{20} m^{-3} (0.1-1% of the total N_2 density). At high electron density the density of the metastable molecule increases with increasing distance to the arc source. This suggests that $N_2(A^3\Sigma_u^+)$ is formed in the vessel (on the walls of the vessel) rather than inside the arc. The density of $N_2(A^3\Sigma_u^+)$ found (0.1-1% of the total N_2 density) shows that a significant amount of energy in this plasma is carried by stable neutral molecules. Because of its role in the reaction mechanisms in the nitrogen plasma and its possible use as an active specie on surfaces, the origin of $N_2(A^3\Sigma_u^+)$ should be a topic in future investigations.

To account for the charge exchange between atomic ions and vibrationally excited ground state molecules, $N_2(X^1\Sigma_g^+, v > 3)$, the density of the latter must be approximately $3 \times 10^{20} \text{ m}^{-3}$. This corresponds to a vibrational temperature of the ground state molecules of 3000 K.

References

- 1 G.S.R. Sarma, in: *Molecular Physics and Hypersonic flow*, ed. M. Capitelli, Kluwer, Dordrecht (1995).
- 2 A. Leyland, K.S. Fancey, A.S. James, and A. Matthews, *Surf. Coat. Technol.* **41**, 295 (1995).
- 3 A. Gicquel, N. Laidani, P. Saillard, and J. Amouraux, *Pure Appl. Chem* **62**, 1743 (1990).
- 4 M.A. Biondi, *Phys. Rev.* **82**, 453 (1951).
- 5 L.G. Piper, *J. Chem. Phys.* **88**, 6911 (1988).
- 6 P.A. Sa, and J. Loureiro, *J. Phys. D: Appl. Phys.* **30**, 2320 (1997).
- 7 M.C.M. van de Sanden, PhD thesis, Eindhoven University of Technology (1991).
- 8 V.M. Lelevkin, D.K. Otorbaev, and D.C. Schram, *Physics of Non-equilibrium Plasmas*, North-Holland, Amsterdam (1992).
- 9 J.B. Hasted, *Physics of Atomic Collisions*, Butterworths, Washington, 1964.
- 10 W.H. Kasner, and M.A. Biondi, *Phys. Rev.* **137**, 317 (1965).
- 11 A. Lofthus, P.H. Krupenie, *J. Phys. Chem. Ref. Data* **6**, 113 (1977).
- 12 R. Van den Bercken, and J. van Broekhoven, Internal report VDF/NT 91-06, Eindhoven University of Technology (1991).
- 13 J.A. Guthrie, R.C. Chaney, and A.J. Cunningham, *J. Chem. Phys.* **95**, 930 (1991).
- 14 D. Smith, N.G. Adams, and T.M. Miller, *J. Chem. Phys.* **69**, 308 (1978).
- 15 M. Saporoschenko, *Phys. Rev.* **111**, 1550 (1958).
- 16 A.V. Phelps, *J. Phys. Chem. Ref. Data*, **20**, 557 (1991).
- 17 W. Freysinger, F.A. Khan, and P.B. Armentrout, *J. Chem. Phys.*, **101**, 3688 (1994).
- 18 V. Guerra, and J. Loureiro, *Plasma Sources Sci Technol.* **6** (1997) 361.
- 19 J. Voogd, *Philips Techn. Tijdschr.* **5**, 87 (1940).
- 20 J.C. de Vos, *Physica* **20**, 690 (1954).
- 21 R.F. Stebbings, B.R. Turner, and A.C.H. Smith, *J. Chem. Phys.*, **38**, 2277 (1963).
- 22 L.G. Piper, *J. Chem. Phys.* **88**, 231 (1988).
- 23 G. Cernogora, C.M. Ferreira, L. Hochard, M. Touzeau, and J. Loureiro, *J. Phys. B: At. Mol. Phys.* **17**, 4429 (1984).

8 Stripping of Photoresist Using a Remote Thermal Ar/O₂ and Ar/N₂/O₂ Plasma

8.1 Introduction

In this chapter the application of the remote arc generated plasma for the removal of photoresist from silicon is presented. The plasma under investigation can and has been used for numerous applications. As will be explained hereafter, several advantages of the setup are particularly suited for stripping of photoresist. This practical application will also illustrate how several of the processes described in previous chapters are combined to give an explanation to the observations made.

One of the most frequently recurring steps in the processing of wafers in the semiconductor industry is the post-etch cleaning of the wafers. After a photoresist layer has been applied, exposed to (UV) light and etched, the residual photoresist has to be removed as well as other etch residues. Traditionally this is done by wet chemical etching. With the use new materials and ever-smaller feature sizes came the need for more selective and controllable cleaning techniques. Since the 1980's, dry plasma etching is being applied for the removal of photoresist [1]. At first RF (13.56 MHz) plasma processing was applied, in which the wafers are directly exposed to the plasma. With a plasma system it was possible to remove more complex photoresist materials and other residues. An added advantage is the elimination of toxic chemicals. A disadvantage of such a system is the occurrence of large bias potentials and charging of the wafers in a RF discharge. Ions are accelerated by the bias potential, which leads to ion bombardment causing damage at the surface. Current induced in the wafers due to charging of the wafers may cause breakdown of underlying components inside the wafer. Since 1992 downstream microwave processing [2, 3] is the technology of choice. The plasma is created in a microwave cavity but the actual process takes place downstream from the source. This reduces the bias potential of the wafer and the damage from ion impact. The plasma creates mainly neutral oxygen atoms needed for the removal of the photoresist. With a remote system it also became possible to move from batch processes (in which a batch of wafers is placed inside the plasma) to continuous, single wafer processes. Furthermore, reactive gases, such as fluorine can be added to the plasma outside the source, without the risk of damaging the plasma source. It appears that remote plasma processing is the most promising technology for the removal of photoresist and other residues. From the experience with downstream microwave processing the demands of a plasma cleaning system can be summarized in four requirements:

1. The ability to remove a wide variety of substances by the use of different gas compositions
2. The ability to use the tool in a continuous process.

3. Low bias potential to prevent damage.
4. High radical density to reduce processing times.

In this context, the use of a DC arc (cascaded arc) source is investigated here for its use in the removal of photoresist. It has many of the same features as a downstream microwave system, but produces radicals at a much higher intensity. This should lead to higher rates of removal of photoresist. The charge exchange and dissociative recombination (see Chapters 5-7) reduces the amount of ions in the plasma and creates reactive atoms. The improved ratio between atoms and ions means that the flux of ions is relatively small and with that, the current through the wafers. The supersonic expansion also makes this source truly remote in the sense that there is no influence of the downstream plasma conditions on the source. By changing downstream conditions such as background pressure, the density of the reactive particles can be influenced (see Chapter 4). In addition, a direct current source such as the cascaded arc is easier to use since it does not need the (constant) tuning of a microwave system.

8.2 Experimental Setup

The experimental setup used in these experiments is the DEPO I setup [4]. It is slightly different from the setup used in other parts of this thesis and described in Chapter 1. The setup is shown schematically in Fig. 8.1. The vacuum vessel is set up vertically. The source is a cascaded arc source with 6 cascade plates. It is mounted vertically in the vacuum vessel and is movable along the vertical axis. Inside the vessel is a substrate holder with temperature control and cooled with liquid nitrogen. Samples are clamped down mechanically on the substrate holder. A small back flow of helium ensures good thermal contact between sample and holder.

Argon and nitrogen are injected into the arc at the cathode side of the arc. Oxygen is injected in a ring inside the vessel, 4 cm downstream from the nozzle. In a few experiments oxygen was also injected directly into the nozzle and into the arc through a channel in the last plate. Because of concern about possible wear to the arc source this last injection method was only

Ar flow	60 sccs
O ₂ flow	0-17 sccs
Arc Current (I_{arc})	82 A
Chamber pressure	3 mbar
distance arc-substrate	30 cm
substrate temperature	350 K

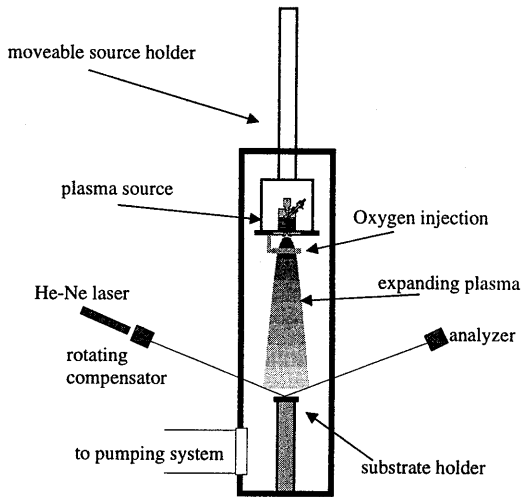


Figure 8.1: Setup for deposition and etching (DEPO I). The plasma source is a six plate cascaded arc

applied in two experiments. In the experiments described here, a standard condition was chosen around which different parameters were varied. These standard conditions are summarized in Table 8.1.

The photoresist (Sumitomo PFI 38A) was spincoated on 6-inch silicon wafers supplied by IMEC Leuven. The resist was baked at 423 K (150 °C). The wafers were cut into smaller, 2×2 cm samples that can be clamped onto the DEPO I substrate holder. The resist layer has a thickness of 1.2 μm and a refractive index of 1.62. The thickness of the layer and etch rates are determined using in-situ ellipsometry. The measured ellipsometric angles, Ψ and Δ , are simulated to obtain thickness, etch rate and refractive index [5]. An example is shown in Fig. 8.2.

8.3 Theory

For the removal of photoresist by plasma treatment it is generally acknowledged that oxygen atoms are the etching species [6, 7, 8, 9]. In the investigation of the downstream arc plasma as a source of atomic oxygen, argon is used as the carrier gas that is activated in the arc. Argon ions emanate from the arc and oxygen gas is injected into the stream 4 cm from the nozzle. Generation of oxygen takes place by charge exchange and dissociative recombination (see for example Chapter 7 of this thesis):

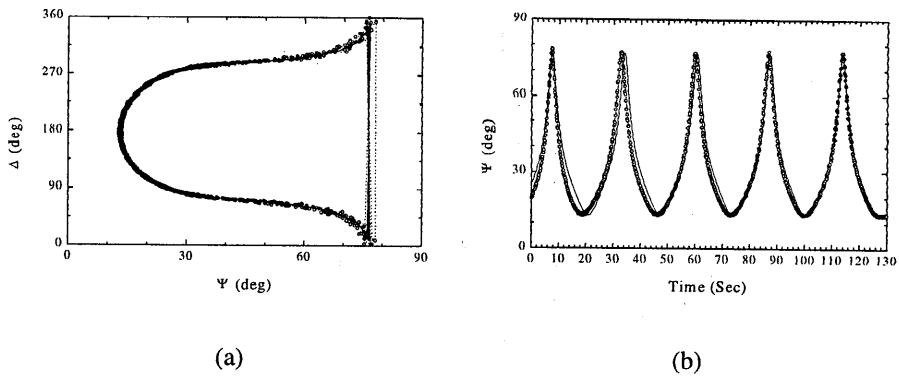


Figure 8.2: Ellipsometry measurements during photoresist stripping. (a) shows the curves in a Ψ - Δ plot. (b) shows Ψ as a function of time. The solid lines are simulations with a refractive index $n = 1.62$



The charge exchange reaction is exothermal (the ionization energy for O_2 is 12.06 eV, for Ar it is 15.6 eV) with a rate of approximately $10^{-16} \text{ m}^3\text{s}^{-1}$ [10]. The rate for dissociative recombination is of the order $10^{-13} \text{ m}^3\text{s}^{-1}$ [11] (comparable to the reactions in nitrogen, extensively described in Chapter 7). After dissociation, the oxygen atoms are transported further downstream to where the substrate is positioned.

It is clear already from this simple kinetic model, that the amount of oxygen atoms produced is limited by the amount of argon ions produced inside the arc. To enhance the production of oxygen atoms, nitrogen is added to the argon as a carrier gas. Similar to the situation with argon, nitrogen ions will undergo charge exchange and dissociative recombination with the oxygen molecules injected downstream. In addition, neutral nitrogen atoms will react with oxygen molecules to form nitric oxide and oxygen atoms [12, 13]:



The rate for this reaction is approximately $5 \times 10^{-18} \text{ m}^3\text{s}^{-1}$ * [12]. The nitric oxide reacts with nitrogen atoms to form another oxygen atom:



with a rate of $10^{-16} \text{ m}^3\text{s}^{-1}$ [12]. In principle both reactions (Eqs. (8.2) and (8.3)) are reversible so that also the back reaction will take place. However, both reactions are exothermal in the

* The exact rate for this reaction depends on the specific ground state of the nitrogen atom.

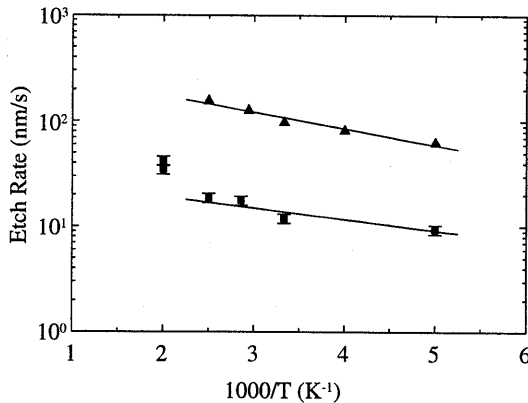


Figure 8.3: Etch rate as a function of reciprocal temperature. ■ Oxygen/argon, and ▲ oxygen/nitrogen/argon plasma mixture. Solid lines are linear fits to the data below 423 K.

direction indicated, yielding 1.4 and 3.2 eV for Eq. (8.2) and Eq. (8.3) respectively. This means that for the backward reactions activation energy is required. Since the temperature of the plasma is much lower (approximately 0.3 eV), the corresponding reaction rates will be small (although the presence of active nitrogen molecules (see Chapter 7) could somewhat increase the rate of the backward reaction of Eq. (8.3)). The main result will be additional production of oxygen atoms when argon/nitrogen is used as the carrier gas, compared to the pure argon plasma.

8.4 Results

8.4.1 Argon/Oxygen

Substrate temperature

The etching rate depends mainly on the flux of atomic oxygen at the substrate and the etching reaction rate constant. The latter depends on the substrate temperature and the activation energy of the surface reaction[†], E_a . If linear kinetics are assumed for the reaction at the substrate, the reaction rate, R_s , can be expressed by:

[†] The exact reaction mechanism at the surface depends on the type of photoresist used, and is beyond the scope of this investigation. Here, an overall activation energy and reaction rate are assumed.

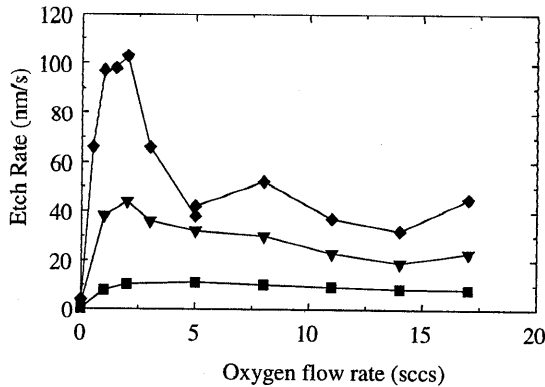


Figure 8.4: Etch rate as a function of oxygen flow rates at different background pressure: ◆ 300 Pa , ▼ 100 Pa, and ■ 25 Pa.

$$R_s = R_{s0} e^{\frac{E_a}{kT_s}} \quad (8.4)$$

The etching rate is shown in an Arrhenius plot as a function of reciprocal substrate temperature in Fig. 8.3. The plasma conditions were kept constant, so that the oxygen flux at the substrate is constant. The activation energy is fitted to the measurements at temperatures below 400K. The activation energy found is $5 \pm 1 \times 10^{-21}$ J/K, the equivalent of 250 ± 100 K. The data above a substrate temperature of 400 K deviates strongly from the line fitted. This is due to the fact that the photoresist was baked at 423 K. When the samples are heated above this temperature, structural changes in the photoresist start taking place, even before the plasma etching has started. For this reason, further experiments have been performed at a substrate temperature of 350 K.

Oxygen flow rate and pressure

Figure 8.4 shows the etch rate as a function of oxygen flow rate at different background pressure (25, 100 and 300 Pa). The argon flow rate and current through the arc have been kept constant. In very general terms, an increase of the pressure will decrease the mean free path and lower the diffusion (of argon ions and oxygen atoms) towards the vessel walls and thus increase the etch rate at the center of the sample. Increasing the oxygen flow rate will increase the production of oxygen atoms. Since the flux of argon ions is limited, it is to be expected that at high oxygen flow rate the etch rate will tend to a limit. This limit is reached when all argon ions have reacted with oxygen molecules following Eq. (8.1). Then the flux of oxygen atoms equals twice the flux of argon ions emanated from the arc. Indeed for oxygen flow rates

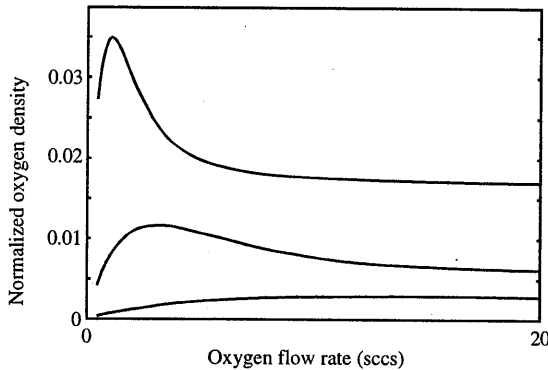


Figure 8.5: Simulation of the oxygen atom density at 30 cm from the exit of the arc, as a function of oxygen flow rate. The upper curve are results for 300 Pa background pressure, the middle curve 100 Pa, and the lower curve 25 Pa. See appendix for a more detailed explanation of the simulation.

below 3 sccs an increase in the etch rate is observed with oxygen flow rates. Also the etch rate increases with increased background pressure, as expected.

Rather surprising is the observation that at higher oxygen flow rates (> 3 sccs) the etch rate decreases and tends to a lower limit. The (qualitative) explanation for this phenomenon could come from the realization that oxygen atoms can diffuse faster than the argon ions. At low oxygen flow rates the partial pressure of O_2 is low and the charge exchange reaction, Eq. (8.1), is slow. Oxygen atoms will be formed throughout the plasma, without much influence on the argon ion density. Increasing the oxygen flow (and with that the partial pressure of oxygen molecules in the background gas) will merely increase the total amount of oxygen atoms produced. The increase in etch rate will be (nearly) linear with the increase in oxygen flow rate, as observed. At high oxygen flow rates, Eq. (8.1) becomes much faster. The argon ion density decreases quickly as a function of distance from the nozzle due to the reaction with oxygen molecules and most of the atomic oxygen will be formed close to the nozzle. In this case the oxygen atoms will have more time to diffuse and the eventual density at the position of the sample will be lower. In the appendix to this chapter this effect is shown quantitatively by solving (numerically) the rate equations for argon ions and oxygen atoms in a freely diffusing plasma with a constant flow velocity, assuming different diffusion coefficients for oxygen atoms and argon ions. The results of these calculations are shown in Fig. 8.5. Even with the results from the appendix it is not possible to completely model the etching behavior as a function of oxygen flow rate as observed in Fig. 8.4, since the presence of the substrate holder disturbs the flow. The free (fitting) parameter in the model is the diffusion coefficient of oxygen atoms.

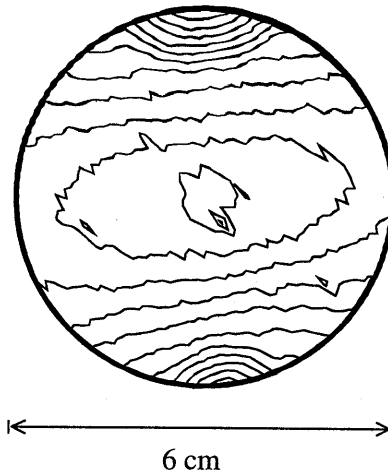


Figure 8.6: Thickness profile on a wafer after 30 seconds of etching with 17 sccs oxygen flow rate at 100 Pa background pressure. The thickness at the center is 590 nm; each contour line indicates a difference in thickness of 15 nm.

To obtain agreement in the ratio between the maximum etch rate and the etch rate at maximum oxygen flow rate (a factor of 2 at 300 Pa), the diffusion of oxygen atoms has to be a factor of 100 larger than for argon ions. Good qualitative agreement is achieved, but the diffusion coefficient for oxygen atoms has to be taken rather large and may indicate that additional reactions are important. For a complete quantitative analysis, a complete numerical model of the plasma including the flow in front of the substrate and the reactions taking place at the surface would be needed.

To get some insight in the homogeneity of the etching process, a 6-inch wafer was etched during 30 seconds. The thickness of the photoresist was measured by scanning the wafer with an ex situ ellipsometer. The thickness in the center of the wafer was calibrated using a scanning electron microscope after breaking the wafer in the middle. The thickness profile is shown in Fig. 8.6. Since the wafer is larger than the substrate holder, it could not be clamped down. Instead vacuum grease was used to stick the wafer to the holder. Still, complete temperature control could not be achieved because the edges of the wafer were extending beyond the substrate holder. This resulted in a slight bending of the wafer. This is the reason that the profile shown in Fig. 8.5 is not symmetric in all directions. It is assumed that bending occurred along the axis shown vertical in Fig. 8.6, since the vacuum grease to the left and right of this axis was discolored. This would also explain, why the etch rate on the sides is

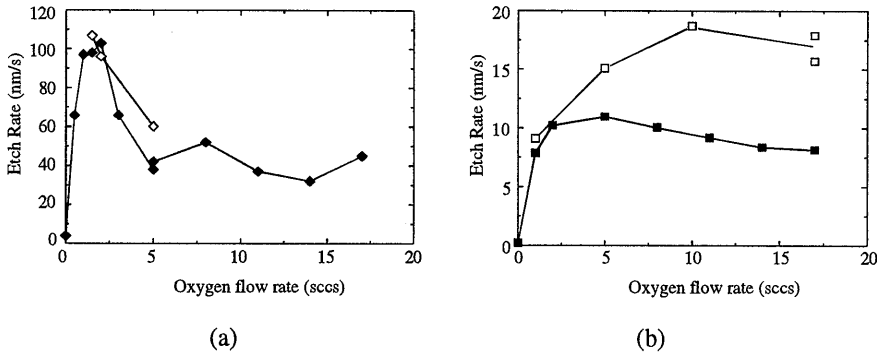


Figure 8.7: Comparison of the etch rate using different injection methods. (a) 300 Pa background pressure, ◆ ring injection (as in Fig. 8.4) ◇ nozzle injection. (b) 25 Pa, ■ ring injection □ injection into the arc channel.

higher than along the vertical axis of Fig. 8.6. The width of the profile along the vertical axis (along which temperature control is least disrupted) is approximately 5 cm.

Injection method

In the setup used, different methods are available for the injection of oxygen into the argon plasma. In the previous results oxygen was injected through a ring, 4 cm downstream from the nozzle. Other positions where oxygen can be injected are injection into the nozzle and injection through the last plate of the cascaded arc into the arc channel.[‡] In Fig. 8.7 (a), the effect of injection into the expansion nozzle on the etch rate is compared to injection through the ring. No significant changes in etch rate are observed. The explanation for this is as follows. When oxygen is injected into the nozzle, a flux of oxygen molecules is carried with the expanding plasma. Because the plasma flow is supersonic over the first few centimeters [14, 15] with a velocity of up to 4000 m/s, it only takes a few microseconds for the plasma to reach the ring. Very few reactions will take place on this time scale. From this point of view little change in the etch rate was expected. In previous analyses (Chapters 4-7) it was argued that molecular species in the background are playing an important role in the reactions between ions and these molecules. In the case of the nozzle injection, clearly the (primary) flow of oxygen molecules into the plasma is the flow coming directly from the injection (not from the background). However, in Chapter 4 it was also shown that at any position downstream in the vessel (even on the axis of the expansion), the density of the particles coming directly from the plasma makes up less than 30% of the total density at that position. The oxygen atoms formed by the

[‡] A fourth method of injecting the oxygen flow is injection into the vessel (background). This method was not used in the current investigation.

plasma diffuse towards the walls and desorb as oxygen molecules. If the probability of association at the wall is close to 1, which is likely in a stainless steel vessel [16, 17], the partial pressure of oxygen molecules in the background gas will be close to the partial flux of oxygen injected (anywhere). Therefore, in this case even when the oxygen flow is injected into the nozzle, most reactions between ions and molecules that take place in the plasma will involve molecules recirculating in the background gas rather than the molecules injected directly into the plasma stream. Thus, also from this point of view injection in the ring is not significantly different from injection through the ring (or into the vessel background). This situation only occurs because the oxygen atoms formed associate at the vessel wall and desorb as oxygen molecules. If this were not the case (for example, if a depositing species is considered, or association probability at the wall is zero), different injection positions will lead to different plasma compositions. If such a species is injected into the plasma flow (through the nozzle), the density of this species will drop as a function of distance from the nozzle (just as the argon ion density drops). Injection in the background of the vessel would lead to an increase in the density of this species as a function of distance to the nozzle. Injection through the ring around the plasma may be considered as an intermediate method, since part of the injected gas will be carried with the plasma flow and part will end up in the background gas. When the probability of association of the atoms (or radicals) formed in the plasma is high (close to 1) such as for oxygen, the position of the injection does not matter.

A different situation occurs when oxygen is injected through the last plate of the cascaded arc, directly into the arc channel. Inside the arc the electron density and temperature are high ($>10^{20} \text{ m}^{-3}$ and 1 eV, respectively). This enables extra dissociation mechanisms for the oxygen molecules by electron impact and by thermal dissociation



and



The etch rates obtained when oxygen is injected into the arc are compared to ring injection in Fig. 8.7 (b). When a small amount of oxygen is injected, the increase in etch rate is small. In this case, the extra production through Eqs. (8.5) and (8.6) is negligible compared to the oxygen produced by the argon ions. When larger amounts of oxygen are injected an enhancement of the etch rate is observed of up to a factor 2. The exact structure of the etch rate as a function of oxygen flow rate is difficult to describe, since the ion composition in the arc will be changed. The effect of injection into the arc consequently is not merely a superposition of the effect of argon ions plus the extra production of Eq. (8.5), but a more complex interaction between the different mechanisms. Because of fear of extensive wear to the arc, no further investigation of the etching behavior was undertaken with oxygen injection into the arc channel. It is worthwhile to investigate whether an arc can be constructed which is

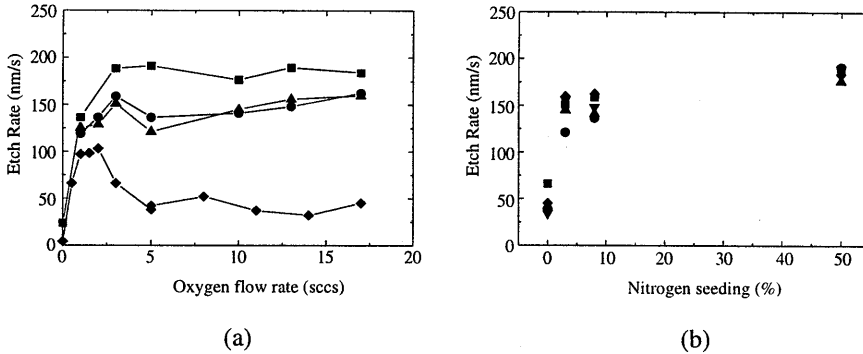


Figure 8.8: (a) etch rate as a function of oxygen flow rate at different nitrogen seeding percentages. \blacklozenge 0%, \blacktriangle 3%, \bullet 8%, and \blacksquare 50%.
 (b) etch rate as a function of nitrogen seeding percentages at different oxygen flow rates. \blacksquare 3 sccs oxygen, \bullet 5 sccs, \blacktriangle 10 sccs, \blacktriangledown 13 sccs, and \blacklozenge 17 sccs.

compatible with the use of oxygen. As a general observation it can be concluded that injection of oxygen into the arc leads to significantly higher etch rates.

8.4.2 Argon/Nitrogen/Oxygen

In the remote thermal argon/oxygen plasma with injection through the ring or in the nozzle, the production of oxygen atoms is limited by the amount of argon ions coming from the plasma source (Eq. (8.1)). To overcome this limitation nitrogen was added to the argon as the carrier gas. Due to the high electron density and temperature inside the arc, the dissociation degree will be high (up to 100%). The nitrogen atoms can dissociate the oxygen molecules injected downstream according to Eq. (8.2). Higher etch rates are therefore expected when an argon/nitrogen mixture is used as the carrier gas. The etch rate was determined as a function of oxygen flow at different partial flow of nitrogen in argon. The results are shown in Fig. 8.8(a). The total flow of the carrier gas (argon + nitrogen) was kept constant at 60 sccs. The background gas was fixed at 300 Pa, the substrate temperature at 350 K, and the oxygen was injected through the ring. The data at 0% nitrogen are the same as shown in Fig. 8.4 and 8.7(a) and are shown again for comparison.

When nitrogen is added to the carrier gas the etch rate increases, as expected. Moreover, the etch rates do not decrease after reaching their maximum value, as was the case in the argon/oxygen plasma. This is a very interesting result in itself, since it makes the etch rate less critically dependent on the oxygen flow rate, which makes tuning the plasma and processing times easier. Although the general behavior (the increase in etch rate when nitrogen is added)

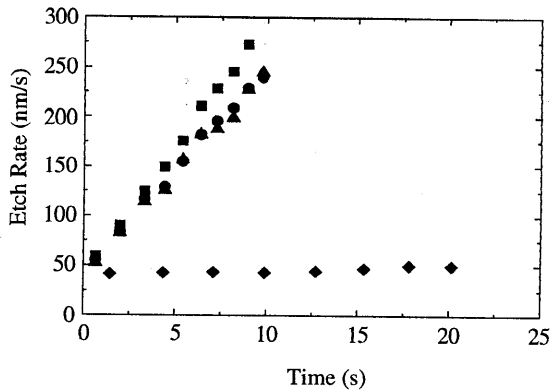


Figure 8.9: Etch rate as function of time at different nitrogen seeding percentages. \blacklozenge 0%, \blacktriangle 3%, \bullet 8%, and \blacksquare 50%.

can be explained using Eq. (8.2), the exact dependency of etch rate on nitrogen admixture is puzzling. The same data as in Fig. 8.8(a) is shown in Fig. 8.8(b) as a function of nitrogen percentage. This figure shows in particular that just a small addition of nitrogen increases the etch rate considerably. This observation was also made by Van Straaten [18]. A higher percentage of nitrogen only slightly increases the etch rate further. This is not according to the expected behavior based on Eq. (8.2). From that reaction alone, one would expect a gradual increase of the etch rate with nitrogen percentage, as the amount of nitrogen atoms produced increases with the nitrogen flow rate. Part of the explanation may be found in the fact that, when nitrogen is added, the nitrogen atoms that are produced will recombine at the vessel wall and desorb as molecules. These molecules in the background gas will undergo charge exchange and recombination with the argon ions, just as the oxygen molecules. There will thus be a competition between the formation of nitrogen atoms and oxygen atoms through charge exchange and dissociative recombination in the downstream plasma. The mechanism for production of oxygen atoms through the reaction of Eq. (8.1) will become less important at higher nitrogen seeding. The extra dissociation of oxygen molecules by nitrogen atoms is then effectively balanced by a reduced charge exchange between ions and oxygen molecules.

Another observation made that may shed some light on the etching behavior of the argon/nitrogen/oxygen plasma is shown in Fig. 8.9. In this figure the etch rate is shown as a function of time at different nitrogen seeding percentages. In the case that only argon is used as the carrier gas, the etch rate remains constant in time. But when nitrogen is added the etch rate increases with time, during the etching process. Since no changes in the plasma were

observed in time, the increase in the etch rate suggests some surface process (the substrate surface changes in time, because it is etched). Figure 8.9 also shows that this increase in etch rate with time does not depend significantly on the amount of nitrogen. Even at 3% nitrogen the increase in the etch rate is observed. It has been suggested that the presence of nitrogen atoms can create a top layer on the sample [19]. This layer may prevent the diffusion of oxygen atoms ad- or absorbed on the surface back into the gas phase. The result is a higher oxygen concentration at the surface, hence a higher etch rate (the pressure cooker effect). Significant changes in the surface composition during etching, in the presence of small amounts of nitrogen, were also observed in etching by transformer coupled plasmas by Nijsten et al. [20]. The plasma systems used and etch rates observed differ too much to enable a detailed comparison.

A different explanation could be found in changes of the vessel walls during plasma operation. Such observations have been reported in literature [16, 17, 21, 22]. The explanation given in these references is that the presence of other gases reduces the wall association of oxygen atoms. Other atoms (in this case nitrogen atoms) will compete with oxygen atoms for the available reactive sites on the wall. As a result less oxygen atoms will associate, thus increasing the oxygen atom density in the gas phase. It would seem from Fig. 8.9 that these processes continue in time, at least during the time it takes to etch the 1.2 μm layer (which takes only 6 seconds). Clearly, more detailed studies are needed to understand the observed etching behavior.

8.5 Conclusions

Very high etch rates were achieved (up to 200 nm/s) using the expanding thermal arc plasma. The etch rate increases with background pressure, as expected from the flow and diffusion of the plasma studied in Chapter 4. When using argon as the carrier gas and injecting oxygen downstream through the ring, the etch rate initially increases with oxygen flow rate, due to an increase in the production of oxygen atoms by charge exchange and dissociative recombination. At higher oxygen flow rates (> 3 sccs) the etch rate decreases. This behavior can be (qualitatively) explained by the mechanism of charge exchange and dissociative recombination combined with flow and diffusion in the downstream plasma. Injecting oxygen in the nozzle of the source does not change the etch rate. Injection of oxygen directly into the arc increases the etch rate at high oxygen flow rates due to the dissociation of oxygen molecules by electron impact in the arc.

Adding a small amount (3%) of nitrogen to argon as the carrier gas results in higher etch rates. The etch rate does not decrease at high oxygen flow rates. This may be due to a decrease in oxygen atom production through charge exchange on one hand (since nitrogen molecules will

consume part of the ions coming from the arc) that is compensated by an increase in the production of oxygen atoms by reactions of oxygen molecules with nitrogen atoms. Adding more nitrogen does not lead to much higher etch rates. An increase of the etch rate as a function of time was observed in the argon/nitrogen/oxygen plasma. This suggests a surface process induced by the presence of nitrogen. Clearly, better understanding of the kinetics in this plasma is needed, especially those involving the different kinds of molecules (NO, excited N₂ and/or O₂) that may play a significant role in surface processes.

The goals of the initial investigations were achieved: reaching high etch rates using a remote plasma with very low electron and ion energies. The etch rate can be controlled by external parameters, such as background pressure, substrate temperature or gas composition. The details of the plasma and surface chemistries need further investigation.

References

- 1 J. Sargent, V. Starov, and W. Rust, *Solid State Technol.* **May 1997**, 171 (1997)
- 2 J.W. Metselaar, V.I. Kuznetsov, and A.G. Zhidkov, *J. Appl. Phys.* **75**, 4910 (1994)
- 3 F. Pasierb, A. Ghanbari, M.S. Ameen, and R.S. Heinrich, *J. Vac. Sci. Technol. A* **10**, 1096 (1992).
- 4 J.W.A.M. Gielen PhD thesis, Eindhoven University of Technology (1996)
- 5 R.M.A. Azzam, and N.M. Bashara, *Ellipsometry and Polarized Light*, North-Holland, Amsterdam (1977).
- 6 J.M. Cook, and B.W. Benson, *J. Electrochem. Soc.* **130**, 2459 (1983).
- 7 D.M. Manos, D.L. Flamm, *Plasma Etching*, Academic Press, New York (1989).
- 8 Sang-Kyu Park, and D.J. Economou, *J. Appl. Phys.* **66**, 3256 (1989).
- 9 M.A. Hartney, D.W. Hess, and D.S. Soane, *J. Vac. Sci. Technol. B* **7**, 1 (1989).
- 10 S.C. Brown, *Basic Data of Plasma Physics, 1966*, 2nd ed. MIT press, Cambridge (1966).
- 11 J.B. Hasted, *Physics of Atomic Collisions*, Butterworths, Washington (1964).
- 12 B.F. Gordiets, C.M. Ferreira, V.L. Guerra, J.M.A.H. Loureiro, J. Nahorny, D. Pagnon, M. Touzeau, and M. Vialle, *IEEE Trans. Plasma Sc.* **23**, 750 (1995).
- 13 V. Guerra, and J. Loureiro, *Plasma Sources Sci. Technol.* **6**, 373 (1997).
- 14 See for example: M.C.M. van de Sanden, PhD thesis, Eindhoven University of Technology (1991).
- 15 M.C.M. van de Sanden, J.M. de Regt, and D.C. Schram, *Plasma Sources Sci. Technol.* **3**, 501 (1994).
- 16 J.P. Booth, N. Sadeghi, *J. Appl. Phys.* **70**, 611 (1991).
- 17 A. Granier, F. Nicolazo, C. Vallée, A. Gouillet, G. Turban, and B. Grolleau, *Plasma Sources Sci. Technol.* **6**, 147 (1997).
- 18 O. van Straaten, internal report VDF/NT 97-18, Eindhoven University of Technology (1997).
- 19 N. Koyama, T. Endoh, H. Fukuda, and S. Nomura, *J. Appl. Phys.* **79**, 1464 (1996).
- 20 S. Nijsten, internal report VDF/NT 96-25, Eindhoven University of Technology (1996).
- 21 J.P. Booth, O. Joubert, and J. Pelletier, *J. Appl. Phys.* **69**, 618 (1991).
- 22 M.D. Costa, P.A. Zuliani, and J.M. Deckers, *Can. J. Chem.* **57**, 568 (1979).

Appendix to Chapter 8

Flow, diffusion, recombination and volume production of argon ions and oxygen atoms.

Argon ions

The flow and free diffusion of argon ions emanated from the plasma source was treated in chapter 4. In the case that oxygen molecules are injected into the downstream plasma recombination will take place (see Eq. (8.1)). If we assume that the recombination does not significantly deplete the molecular density, or diffusion from the vessel walls is fast enough to compensate this depletion, the density of oxygen molecules can be considered to be constant throughout the vessel. The rate equation for argon ions in steady state is then given by

$$\frac{dn_{Ar^+}}{dt} = -\bar{\nabla} \cdot (\bar{v}_d n_{Ar^+}) + \bar{\nabla} \cdot (D_a \bar{\nabla} n_{Ar^+}) - n_{Ar^+} n_{O_2} k_{ce} = 0 \quad (A 1)$$

with n_{Ar^+} the density of the argon ions, \bar{v}_d the drift velocity, D_a the diffusion coefficient of the argon ions, n_{O_2} the density of oxygen molecules, and k_{ce} the rate coefficient for charge exchange between argon ions and oxygen molecules. Since the electron temperature is low (0.1-0.5 eV) there is no production of ions in the downstream plasma. Eq. (A.1) can be simplified if we assume that the drift velocity only has a component in the (positive) z -direction, diffusion in the z direction is negligible compared to the drift term, and the diffusion coefficient is constant throughout the part of the plasma under investigation (these are the same assumptions as in chapter 4). Eq. (A 1) can now be rewritten in cylindrical coordinates as

$$-v_d \frac{\partial n_{Ar^+}(z, r)}{\partial z} + D_a \frac{1}{r} \left(\frac{\partial}{\partial r} \left(r \frac{\partial n_{Ar^+}(z, r)}{\partial r} \right) \right) = n_{Ar^+}(z, r) n_{O_2} k_{ce} \quad (A 2)$$

The solution is of the form

$$n_{Ar^+}(z, r) = n_{Ar^+}(z, 0) \cdot e^{-\frac{r^2}{(\rho(z))^2}} \quad (A 3)$$

with $\rho(z)$ the radius of the distribution at position z . Substituting this into the differential equation Eq. (A 2) leads to

$$\begin{aligned}
 & -v_d \cdot e^{-\frac{r^2}{(\rho(z))^2}} \left(\frac{\partial n_{Ar^+}(z,0)}{\partial z} + n_{Ar^+}(z,0) \frac{2r^2}{(\rho(z))^3} \frac{\partial \rho(z)}{\partial z} \right) + \frac{4D_a}{(\rho(z))^2} n_{Ar^+}(z,0) \cdot e^{-\frac{r^2}{(\rho(z))^2}} \left(\frac{r^2}{(\rho(z))^2} - 1 \right) = \\
 & n_{Ar^+}(z,0) \cdot e^{-\frac{r^2}{(\rho(z))^2}} n_{O_2} k_{ce}
 \end{aligned} \tag{A 4}$$

Analogous to the treatment in chapter 4 this must hold for all r , we now find:

$$\begin{aligned}
 & -v_d \frac{2r^2}{(\rho(z))^3} \frac{\partial \rho(z)}{\partial z} + \frac{4D_a}{(\rho(z))^2} \frac{r^2}{(\rho(z))^2} = 0 \\
 & \wedge \\
 & -v_d \frac{\partial n_{Ar^+}(z,0)}{\partial z} - \frac{4D_a}{(\rho(z))^2} n_{Ar^+}(z,0) = n_{Ar^+}(z,0) n_{O_2} k_{ce}
 \end{aligned} \tag{A 5}$$

The first part of Eq. (A 5) leads to exactly the same development of the radius $\rho(z)$:

$$\rho(z) = \left(\frac{4D_a}{v_d} z + (\rho(0))^2 \right)^{\frac{1}{2}} \tag{A 6}$$

The density on the axis of the expansion, $n_{Ar^+}(z,0)$, is found after rearranging Eq. (A 5) to

$$\frac{1}{n_{Ar^+}(z,0)} \frac{\partial n_{Ar^+}(z,0)}{\partial z} = - \frac{1}{\left\{ z + \frac{(\rho(0))^2 v_d}{4D_a} \right\}} - n_{O_2} k_{ce} \frac{1}{v_d} \tag{A 7}$$

The right hand side of this equation is a superposition of the freely diffusing particle flow (without recombination) and the term that accounts for recombination. The solution is found to be:

$$n_{Ar^+}(z,0) = n_{Ar^+}(0,0) \frac{1}{\left(\frac{4D_a}{v_d (\rho(0))^2} \right) z + 1} \cdot e^{-n_{O_2} k_{ce} \frac{1}{v_d} z} \tag{A 8}$$

The solution for the density is (simply) the product of the solution found in chapter 4 and an exponential term to account for the recombination.

Oxygen atoms

Oxygen atoms are produced after charge exchange and dissociative recombination of argon with oxygen molecules (see Eq. (8.1)). If the electron density is high enough the charge exchange will be the limiting step in the reaction mechanism. The production of oxygen atoms is then equal to the rate of charge exchange. The rate equation in steady state is then given by

$$\frac{dn_o}{dt} = -\bar{\nabla} \cdot (\bar{v}_d n_o) + \bar{\nabla} \cdot (D_o \bar{\nabla} n_o) + 2n_{Ar^+} n_{O_2} k_{ce} = 0 \quad (A 9)$$

with n_o the density of oxygen atoms, \bar{v}_d the drift velocity, and D_o the diffusion coefficient. The diffusion coefficient of oxygen atoms will be higher than that of argon ions, since the atoms are lighter and will not undergo the resonant charge exchange that inhibits the diffusion of argon atoms in a predominantly neutral argon background. It is clear from a comparison of Eq. (A 9) with Eq. (A 1), or from the reaction mechanism (Eq. (8.1)), that the production of oxygen atoms is (twice) the recombination of argon ions. The solution for the density of oxygen atoms is much more complicated than for argon, since the argon ion density, given by Eqs. (A 6) and (A 8) now appears in the differential equation Eq. (A 9).

First we will simplify Eq. (A 9) under the same assumptions concerning flow and diffusion as was done for the argon ions:

$$-v_d \frac{\partial n_o(z,r)}{\partial z} + D_o \frac{1}{r} \left(\frac{\partial}{\partial r} \left(r \frac{\partial n_o(z,r)}{\partial r} \right) \right) = n_{Ar^+}(z,r) n_{O_2} k_{ce} \quad (A 10)$$

The homogeneous solution of this equation (setting the right hand side to zero) leads to the solution for the free diffusion of flowing particles:

$$n_o(z,r) = n_o(z,0) \cdot e^{-\frac{r^2}{(\rho_o(z))^2}} \quad (A 11)$$

with

$$n_o(z,0) = n_o(0,0) \frac{1}{\left(\frac{4D_o}{v_d (\rho_o(0))^2} \right) z + 1} \quad (A 12)$$

and

$$\rho_o(z) = \left(\frac{4D_o}{v_d} z + (\rho_o(0))^2 \right)^{\frac{1}{2}} \quad (A 13)$$

This solution is not yet very interesting since the initial density, $n_o(0,0)$ is zero, and the initial radius, $\rho_o(0)$, is not defined. To find the oxygen atom density at some position z , we have to integrate the production (the right hand side of Eq. (A 10)) at each position z' along the axis over an infinitesimal interval dz' and set this as the initial condition for the solution of the

homogeneous part of Eq. (A 10). The oxygen density at the position z of interest, due to the production in the interval $[z', z' + dz']$ is given by

$$dn_o(z,0) = dz' 2n_{Ar^+}(z',0)n_{O_2}k_{ce} \frac{1}{v_d} \frac{1}{\left(\frac{4D_o}{v_d(\rho(z'))^2} \right) (z-z') + 1} \quad (\text{A } 14)$$

with $n_{Ar^+}(z',0)$ the argon ion density at z' , given by Eq. (A 8), and $\rho(z')$ the radius of the argon ion distribution at z' given by Eq. (A 6). This can be rewritten in a slightly more convenient form as

$$dn_o(z,0) = dz' 2n_{Ar^+}(0,0)n_{O_2}k_{ce} \frac{1}{v_d} \cdot e^{-n_{O_2}k_{ce} \frac{1}{v_d} z'} \cdot \frac{1}{\frac{4D_o}{v_d(\rho(0))^2} (z-z') + \frac{4D_a}{v_d(\rho(0))^2} z' + 1} \quad (\text{A } 15)$$

The total oxygen atom density on the axis, at a position z , $n_o(z,0)$, is found by integrating Eq. (A 15) over z' :

$$n_o(z,0) = 2n_{Ar^+}(0,0)n_{O_2}k_{ce} \frac{1}{v_d} \cdot \int_0^z \frac{e^{-n_{O_2}k_{ce} \frac{1}{v_d} z'}}{\frac{4D_o}{v_d(\rho(0))^2} (z-z') + \frac{4D_a}{v_d(\rho(0))^2} z' + 1} dz' \quad (\text{A } 16)$$

A similar procedure can be undertaken for each position r to find the radial profile of the oxygen atom density.

A simulation has been made to compare the calculated atomic oxygen density to the etch rates observed in Fig. 8.4. The measurements were taken as a function of oxygen flow rate. The oxygen flow rate can (in first approximation) be related to the oxygen molecule density by

$$n_{O_2} = \frac{\phi_{O_2} p}{\phi_{tot} kT} \quad (\text{A } 17)$$

with ϕ_{O_2} and ϕ_{tot} the flow rate of oxygen and total flow rate (argon plus oxygen), respectively. Using the rate for charge exchange, k_{ce} , of $10^{-16} \text{ m}^3 \text{ s}^{-1}$, the drift velocity, v_d , of 400 m/s, and gas temperature of 10^3 K , Eq. (A.16) can be calculated as a function of oxygen flow rate. The ambipolar diffusion coefficient at 300 Pa background pressure is approximately $0.04 \text{ m}^2 \text{ s}^{-1}$ (see chapter 4), and the radius at position $z = 0$ is estimated to be 1 cm. The argon density at the position (0,0) is set to 1 in the case of the highest pressure (300 Pa) to normalize the plots. The argon density at the position (0,0) approximately scales with the pressure (see for example [14]). The diffusion coefficients and the square of the radius, $(\rho(0))^2$, scale with

reciprocal pressure (see for example chapter 4). The only free parameter left is the diffusion coefficient of oxygen, D_O . The value for D_O is adjusted to obtain agreement between the simulation and the measured data. Most attention in this simulation is paid to obtain the correct ratio between the highest etch rate and the etch rate at the highest oxygen flow (a factor of 2 in the case for 300 Pa). Best agreement in this respect is achieved when the diffusion coefficient for oxygen atoms is a factor 100 higher than for argon ions.

The result of the simulations is shown in Fig. A.1. An overview of the parameters used is given in Table A.1.

Variable	300 Pa	100 Pa	25 Pa
$n_{Ar^+}(0,0)$	1	0.3	0.08
$\frac{4D_a}{v_d(\rho(0))^2}$	4 m ⁻¹	4 m ⁻¹	4 m ⁻¹
$\frac{4D_o}{v_d(\rho(0))^2}$	400 m ⁻¹	400 m ⁻¹	400 m ⁻¹
n_{O_2}	0.5×10^{21} m ⁻³	0.2×10^{21} m ⁻³	0.5×10^{20} m ⁻³

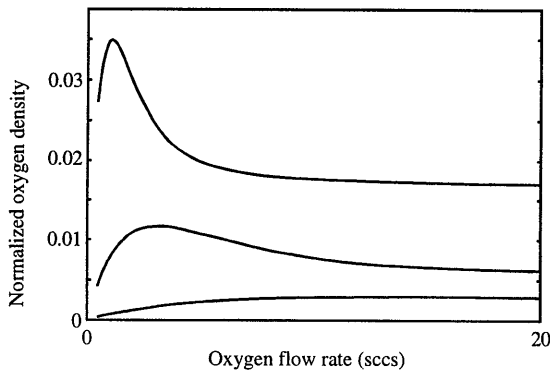


Figure A.1: Simulation of the oxygen density at $z = 30$ cm. The upper curve are results for 300 Pa background pressure, the middle curve 100 Pa, and the lower curve 25 Pa.

9 General Conclusions

The subject of this thesis is the investigation of the remote arc generated plasma in diatomic gases. Each chapter consists of more or less separate investigations with specific conclusions based on the results in that chapter. Here, these conclusions are generalized to show their importance to the overall picture of the plasma in diatomic gases.

- The main loss mechanism for ions and electrons in the plasmas containing diatomic gases is charge exchange of atomic ions with neutral molecules followed by dissociative recombination. Compared to purely atomic plasmas (such as argon plasmas) where the main loss mechanism is diffusion to the vessel wall, the electron/ion density in the plasma with diatomic gases decreases much faster. Only at low densities (typically below a few times 10^{16} m^{-3}) does diffusion become important. The main ion at these low densities is the molecular ion. The mechanism of charge exchange and dissociative recombination is also an important mechanism for production of atoms in the downstream plasma.
- For the determination of electron/ion density, temperature and ion mass, the theory of Langmuir probe measurements has been critically reviewed. The most accurate theory for the interpretation of Langmuir probe measurements in the downstream plasma is the *theory of cylindrical probes in a collisionless plasma at rest* (by J.G. Laframboise). Different probe configurations and geometries lead to similar results. It is possible to determine the electron density with less than 20% uncertainty and electron temperature with less than 30% uncertainty. The saturation currents of the single Langmuir probe measurements have an inaccuracy of less than 5%. From the saturation currents, the mass of the ions can be determined (with an uncertainty of 15%). The theory for Langmuir probe measurements in a magnetized plasma was compared to experimental results in argon. After an empirical adjustment to the theory, it is possible to determine the electron density in the remote magnetized plasma in diatomic gases, and from that the effective ion mass with an uncertainty of 40%. Establishing the accuracy of the measurements enables kinetic modeling of the plasma based on Langmuir probe measurements.
- A new diagnostic technique has been introduced to determine the dissociation degree in the downstream hydrogen plasma, based on Electron Beam Induced Fluorescence (EBIF). With the present setup, dissociation degrees above 1% can be measured in hydrogen. In principle it is possible to determine the dissociation degree by this method in any not magnetized remote arc generated plasma with sufficient degree of dissociation.

- Resonant LIF on argon has shown that the drift velocity in the downstream argon plasma is between 600 and 300 m/s and decreases with distance from the nozzle. The temperature of the neutral (metastable) argon atoms lies between 2000 and 3000 K and shows no significant dependence on axial or radial position over the region under investigation. The electron temperature (determined by Langmuir probe measurements) is equal to the heavy particle temperature.
- A simplified quasi two-dimensional model has been set up to calculate the density of particles in the downstream plasma. It is possible to find analytical expressions to describe the density distribution for three classes of particles:
 1. The particles emanated from the arc that do not significantly react in the downstream plasma but diffuse towards the vessel walls where they are lost (in this thesis argon ions in a pure argon plasma). The flow model has been solved analytically to obtain the density distribution of the particles in the downstream plasma. The radial density distribution is described by a Gaussian. The density on the axis is inversely proportional to the distance to the nozzle, the radius increases with the square root of the distance to the nozzle.
 2. The particles emanated from the arc that are lost in the downstream plasma by a first order reaction mechanism with one reactant with a constant density (in this thesis the charge exchange of atomic ions with neutral molecules). The density of these particles is found directly from the analytical solution of the model. The extension from the previous case consists (simply) of a multiplication by an exponential factor that contains the density of the reactants and the rate coefficient for the reaction.
 3. Particles created by a first order reaction between particles emanated from the source and a reactant with constant density in the downstream plasma (in this thesis the formation of oxygen atoms via charge exchange between argon ions and oxygen molecules injected downstream, followed by fast dissociative recombination of the molecular ions). The analytical solution of the model must be integrated numerically to obtain local densities.
- It has been shown for the first time that electronically excited metastable neutral molecules are present in the downstream nitrogen plasma. These molecules affect the ion composition. It also shows that in the remote arc generated plasma significant amounts of energy may be stored in the recirculating background gas.

- The stripping of photoresist using oxygen injected into the remote arc generated argon plasma leads to very high etch rates (100 nm/s at 350 K substrate temperature). This shows that exceptionally high fluxes of atoms can be produced by downstream injection of a diatomic gas into the plasma.
- When using nitrogen/argon mixtures as the carrier gas in the arc and injecting oxygen downstream, the etch rate of photoresist increases in time during the etch process. Although the exact processes involved are not yet well understood, the results show that additional kinetics can be induced by using combinations of different atomic radicals produced by injection in the source and/or in the downstream or in the arc source.
- From Chapters 4-7 and the first part of Chapter 8 a good understanding has been reached of the general behavior of particles in the downstream plasma with diatomic gases. The second part of Chapter 8 shows an example of an application of the remote arc generated plasma in mixtures of diatomic gases. From the results of the last experiments one must conclude that the kinetics involved (both in the gas phase and on the surface) are more complex. The diagnostic tools investigated in the Chapters 2-4 yield a good combination of measurements to investigate mixtures of gases in the plasma. Where charge particles can be identified by Langmuir probe (Chapter 2), neutral particles (atoms and molecules) can be investigated by EBIF (Chapter 3). Additional information on the reaction mechanisms is obtained by emission spectroscopy. The reaction rates will be found by combining the density measurements with velocity and temperature measurements from LIF (Chapter 4).

Summary

In this thesis the operation of the remote arc generated plasma is investigated in nitrogen, hydrogen and oxygen. The remote plasma has been designed for plasma processing such as etching and deposition of thin films. Furthermore, the high intensity of active particles created by the source and the freedom in operating parameters make this plasma particularly useful for fundamental research of plasma-surface interactions and gas-phase chemical kinetics.

Two diagnostic techniques are analyzed for the characterization of the plasma. The Langmuir probe theory for the determination of ion and electron density and temperature under the specific conditions of the downstream plasma is examined. Results of single and double probes are compared as well as cylindrical and planar probes. With the appropriate theories, the different methods and probe shapes lead to consistent results. Electron temperatures can be measured with an uncertainty of approximately 30%. The uncertainty in density is 20%, mainly due to the uncertainty in the temperature measurements. Ion and electron saturation current can be determined with an inaccuracy of less than 5%. In addition to density and temperature the ion mass can be found from the ratio of electron and ion currents to the probe. Further investigations were undertaken to extend the Langmuir probe diagnostic to measurements in magnetized plasmas. After adaptation of the existing theory to fit measurements in magnetized argon plasmas, it is possible to determine the ion mass to within 40% in the magnetized downstream plasma in nitrogen and hydrogen. With the investigation of the Langmuir probe it is now possible to perform reliable measurements of the behavior of charged particles, so that these results can be used as a basis for kinetic models.

Secondly, a new diagnostic technique is presented, based on Electron Beam Induced Fluorescence (EBIF) for the determination of the degree of dissociation in hydrogen. In the experiments an electron beam with 5 keV illuminates the plasma. The fluorescent light emitted by excited hydrogen atoms is measured. With the use of a collisional radiative model the dissociation degree of hydrogen is found. The result of the first experiment using this technique is presented, where a dissociation degree of $5 \pm 1\%$ was measured.

Resonant Laser Induced Fluorescence (LIF) on argon is used to investigate the drift velocity in the downstream plasma. A quasi 2-dimensional flow model is presented and compared to LIF and probe measurements. When the average drift velocity (400 ± 50 m/s) is used as an input parameter, the diffusion constant needed to describe the density profiles is a factor two to three lower than expected from temperature measurements. If the observed decrease in drift velocity is taken into account in the model, all parameters are within experimental accuracy.

Gas-phase kinetics involving ions are investigated in the downstream nitrogen plasma. Measurements in argon-nitrogen mixtures show fast recombination of ions and electrons. This is explained by charge exchange of atomic ions with neutral molecules, followed by dissociative recombination of the molecular ion. More detailed analysis based on emission

spectroscopy and probe measurements reveals the occurrence of charge exchange between atomic nitrogen ions and metastable $N_2(A^3\Sigma_u^+)$ molecules. Combining the results from emission spectroscopy and probe measurements with the earlier LIF measurements of the drift velocity enables calculation of the densities of N^+ , N_2^+ , and $N_2(A^3\Sigma_u^+)$ throughout the downstream nitrogen plasma. The results show that significant amounts of $N_2(A^3\Sigma_u^+)$ are present.

As an example of an application of the remote arc generated plasma in diatomic gases, stripping of photoresist by oxygen and oxygen-nitrogen plasmas is presented. High etch rates (up to 100 nm/s) are observed when oxygen is injected downstream in an argon plasma. These results show that a high flux of radicals can be created by interaction of ions from the arc source with molecules injected downstream. In a further investigation argon-nitrogen mixtures have been used as the carrier gas through the arc. Downstream injection of oxygen into these plasmas leads to even higher etch rates (up to 200 nm/s). In these last experiments, an increase in the etch rate was observed during etching, suggesting changes in the etched surface or conditioning of the vessel through the presence of nitrogen in the plasma.

In the course of the investigations in this thesis a general view is established of the behavior of active particles, ions in particular, in the downstream arc generated plasma in diatomic gases. Quasi two-dimensional models with analytical solutions are set up to describe the drift and diffusion of particles coming from the arc source, as well as for species lost through first-order reactions and those formed by first-order reactions in the gas-phase. With this knowledge, it is possible to describe and predict how the densities of those species are influenced by external parameters, such as background pressure and gas flow. The presence of active neutral molecules in the nitrogen plasma and the etching behavior in nitrogen-oxygen mixtures suggest the possibility of creating active particles at a plasma-surface boundary.

Samenvatting

Dit proefschrift behandelt het met een boogontlading op afstand gegenereerde plasma in stikstof, waterstof en zuurstof. Dit zogenaamde *remote* plasma is ontworpen voor het verbeteren van materialen en het deponeren van dunne lagen (plasma processing). Door de hoge intensiteit aan actieve deeltjes die door de plasmabron worden geleverd en de grote mate van vrijheid waarin het plasma kan worden beïnvloed is het bovendien zeer geschikt voor fundamentele studies van plasma-oppervlakte interacties en chemische processen in de gasfase. Twee diagnostieken voor de karakterisering van het plasma zijn onderzocht. De theorie van Langmuir-sondemetingen is bestudeerd voor de bepaling van ionen- en electronendichtheden en electronentemperatuur uit metingen die zijn gedaan onder de omstandigheden die heersen in het te onderzoeken plasma. Als de juiste theorie wordt gebruikt leiden metingen met verschillende sondes (cilindrische en platte) en meetmethodes (enkele en dubbele configuratie) tot overeenkomstige resultaten. De elektronentemperatuur kan worden bepaald met een onnauwkeurigheid van ongeveer 30%. De onnauwkeurigheid in de bepaling van de elektronendichtheid is ca. 20% en wordt voornamelijk veroorzaakt door onnauwkeurigheden in de bepaling van de temperatuur. De onnauwkeurigheid in de flux van ionen en elektronen is minder dan 5%. De massa van de ionen kan worden berekend uit de verhouding tussen de elektronen- en ionenstroom. De mogelijkheid is onderzocht om betrouwbare Langmuir-sondemetingen te verrichten in gemagnetiseerde plasma's. Na aanpassing van de bestaande theorie voor dergelijke metingen aan resultaten verkregen in argon is het mogelijk om de massa van de ionen in het gemagnetiseerde plasma te bepalen met een onnauwkeurigheid van ca. 40% (als de massa van de ionen eenmaal bekend is, kunnen de plasmameters worden bepaald uit metingen in de dubbel-sonde configuratie). Het resultaat van dit onderzoek is dat het nu mogelijk is om betrouwbare metingen te doen die kunnen dienen als basis voor modellering van de kinetika in het plasma

Een nieuwe meetmethode om de dissociatiegraad in het waterstofplasma te meten wordt geïntroduceerd, gebaseerd op elektronenbundel-geïnduceerde-fluorescentie (Elektron Beam Induced Fluorescence, EBIF). In deze experimenten wordt een elektronenbundel met een energie van 5 keV door het plasma geschoten. De elektronen slaan deeltjes aan die vervallen onder het uitzenden van licht. Met behulp van een botsing-stralingsmodel wordt de gemeten intensiteit van het licht geanalyseerd en wordt de dissociatiegraad bepaald. Bij het eerste resultaat van deze meetmethode is een dissociatiegraad gemeten van $5 \pm 1\%$.

Resonante laser-geïnduceerde fluorescentie (LIF) wordt toegepast in een argon plasma om de snelheid en temperatuur van het plasma te bepalen. Een quasi-tweedimensionaal stromingsmodel wordt opgezet en vergeleken met de resultaten van de LIF- en Langmuir-sondemetingen. Als de gemiddelde stromingssnelheid (400 ± 50 m/s) wordt gebruikt in het

model blijkt dat de waarde van de diffusiecoëfficiënt die uit het model volgt lager is dan mocht worden verwacht uit metingen van de temperatuur. Als de waargenomen afname van de stromingssnelheid als functie van de afstand tot de bron wordt meegenomen in het model, liggen de waarden van alle variabelen binnen de meetonnauwkeurigheid.

In het stikstofplasma worden de reacties onderzocht waarbij ionen betrokken zijn. Metingen in argon-stikstof mengsels tonen aan dat er snelle recombinatie plaatsvindt als er stikstof in het plasma aanwezig is. Dit kan worden verklaard door een ladingsuitwisselingsreactie tussen atomaire ionen en neutrale moleculen, gevolgd door dissociatieve recombinatie van de moleculaire ionen. Gedetailleerder onderzoek naar dit mechanisme in stikstof heeft aanwijzingen opgeleverd voor een ladingsuitwisseling tussen atomaire stikstofionen en elektronisch aangeslagen metastabiele stikstofmoleculen in de $N_2(A^3\Sigma_u^+)$ toestand. Door resultaten te combineren van optische emissiespectroscopie, Langmuir-sondemetingen en LIF-metingen, zijn de dichtheden bepaald van N^+ , N_2^+ en $N_2(A^3\Sigma_u^+)$. De resultaten tonen aan dat een belangrijk deel van de stikstofmoleculen zich in de metastabiele $N_2(A^3\Sigma_u^+)$ toestand bevindt.

Als voorbeeld van toepassing van het door de boogontlading gegenereerde plasma in twee-atomige gassen is het verwijderen van fotogevoelig materiaal (een proces in de fabricage van chips) onderzocht. Om dit materiaal kunnen etsen wordt zuurstofgas na de bron toegevoegd aan een argon plasma. Hoge etssnelheden (tot 100 nm/s) zijn op deze manier bereikt. Dit resultaat toont aan dat met deze plasma's een grote flux van radicalen kan worden gemaakt. Om nog hogere etssnelheden te bereiken wordt stikstof toegevoegd aan het argon in de plasmabron. Het toevoegen van zuurstof (na de bron) aan dit argon-stikstofplasma leidde inderdaad tot nog hogere etssnelheden (tot 200 nm/s). Tijdens dit laatstgenoemde etsproces bleek de etssnelheid toe te nemen. Dit kan duiden op veranderingen van het oppervlak dat wordt geëtsd of van de wand van het lage-drukvat door toevoeging van stikstof.

Gedurende het onderzoek voor dit proefschrift werd een algemeen beeld vastgelegd van het gedrag van actieve deeltjes (ionen in het bijzonder) in het plasma van twee-atomige gassen. Quasi-tweedimensionale modellen met analytische oplossingen werden opgesteld om het gedrag te beschrijven van zowel de deeltjes die uit de bron komen als van de deeltjes die via eerste-orde reacties verloren gaan of worden gevormd. Met deze kennis is het mogelijk om de invloed te beschrijven van externe parameters, zoals achtergronddruk en gasdebiet op het plasma. De aanwezigheid van aangeslagen, neutrale, metastabiele moleculen in het stikstofplasma en het etsgedrag in argon-stikstof-zuurstofmengsels suggereren de mogelijkheid om actieve deeltjes te genereren aan in het plasma geplaatste oppervlakken.

Acknowledgements

The author gratefully acknowledges the support of the Netherlands Technology Foundation (STW) of the Netherlands Organization for Scientific Research (NWO). Part of the work has been performed in a collaborative effort between Wright Patterson Air Force Base and Eindhoven University of Technology and has been supported by the European Office of Aerospace Research and Development (EOARD).

During the course of this research I was fortunate to be able to work closely with several researchers around the world. For this privilege and for the hospitality shown by everyone involved, I would like to acknowledge some people in particular. Dr. Bish Ganguli, Prof. Alan Garscadden, Nada and Bob of the Wright Laboratories (putting together a complete working cascaded arc setup in less than a month must be a record); Prof. Igor Kossyi, Prof. Valery Silakov, Alexander Matveev, and Andrey Chebotarev of the Russian Academy of Sciences; Marc Schaeckens, Prof. Gottlieb Oehrlein, Sjoerd Nijsten, Theo Standaert, and many others at the State University of New York at Albany; Eugen Aldea and Gheorge Dinescu of Institute of Physics and Technology of Radiation Devices in Bucharest for sharing their expertise in the analysis of emission spectroscopy on nitrogen plasmas.

Closer to home, many have contributed to the realization of this thesis. Firstly I would like to thank Richard van de Sanden en Daan Schram for creating a creative, challenging but still relaxed working environment. The technical support by Ries van de Sande, Bertus Hüsken en Herman de Jong has been very important in the (often ad-hoc) changes to the experimental setup and repairs after experiments of the more destructive kind. I would like to thank Marcel Carrère for his help with the Langmuir probes in magnetic fields and Karine Letourneur for her cooperation in the photoresist etching experiments. A lot of experimental results and theoretical insights have come with the help of student-trainees and graduating students. Bedankt/Thanks/Merci Michiel, Maarten, Gareth, David, Michel, Bart, Patrick v.d.V. , Ralph, Patrick v.A., Hans, Jeroen, Eric, Ivo en Elwin. The cooperation with everybody else in the group "Equilibrium and Transport in Plasmas" has improved the quality of the work in this thesis and has made working in this group very enjoyable. Finally, I would like to thank my parents and friends who have contributed to the quality of life outside the university.

Curriculum Vitae

- 14 August 1969 Born in Leidschendam, The Netherlands
- June 1987 Diploma Athenaeum B,
Chr. Lyceum, Alphen aan de Rijn
- September 1987 - Student General Engineering, Virginia Polytechnic Institute and
June 1988 State University (Virginia Tech), Blacksburg, Va., USA.
- September 1988 - Student Applied Physics,
September 1994 Eindhoven University of Technology.
- November 1994 - PhD student,
March 1999 Group Equilibrium and Transport in Plasma, Department of Applied
Physics, Eindhoven University of Technology.